APPLIED ELECTROCHEMISTRY OF POROUS METALS

by

Tyler D. Pounds

A dissertation submitted to Johns Hopkins University in conformity with the requirements for the degree of Doctor of Philosophy

Baltimore, Maryland

December 2018

Abstract

Due to their unique morphologies, nanoporous (NP) materials synthesized by selective dissolution are promising candidates as catalysts for several electrochemical reactions with significant environmental implications, including carbon dioxide (CO_2) reduction and ammonia (NH_3) synthesis. Neither suitable electrocatalysts nor effective electrochemical methods have been discovered for these reactions. In this thesis, I discuss research progress toward these goals, including new catalyst materials and synthesis methods and engineering of novel electrochemical flow cells for precise control of reaction environments.

I discuss a new diffusion bonding method for synthesis of supported NP-Cu and evaluate this material as a CO_2 reduction electrocatalyst. While minor amounts of secondary elements in the NP-Cu detract from the catalyst selectivity, we show the catalytic properties are tuned by the dealloying technique or ionic liquid impregnation. We discuss approaches to optimize NP-Cu for future research.

Next, I investigate sequential electrolysis in a flow cell containing two complete electrochemical cells with porous flow-through electrodes as a possible method to synthesize NH_3. This approach is demonstrated on a model sequential reaction of hydrogen oxidation followed by proton reduction at large current densities. A novel electrode arrangement with adjacent working electrodes located at the flow inlet allows precise control over the local reaction environment. Because the electrochemical cells cannot operate independently, we develop a new technique to precisely control the potential at the non-independent cell. NP-Nb based catalysts are employed as the downstream working electrode to show that these materials can convert reactants passing through them at virtually 100% efficiency with appropriate catalyst morphology and functionalization. While NP-Nb is shown to be a poor NH_3 electrocatalyst, we discuss approaches to employ robust NP-Nb as a support for an active NH_3 catalyst.

We last explore electrodeposition of Cu on model integrated circuit substrates in an ancillary study to NP-Cu synthesis. The electrolytes employ novel mediators, organic acids or atomic Pb, to allow deposition of pristine Cu films in recessed features. A new mechanism is proposed for this process involving differential mediator coverage due to local differences in seed layer structure, resulting in enhanced deposition rates at the bottoms of the recessed features.

Preface

Acknowledgements

Thank you to my wife, Caroline, for her love and support throughout years of study and research. She provided a great deal of encouragement and wisdom and helped me appropriately appreciate and celebrate this accomplishment, which would not have been possible without her. We had a wonderful, joyful baby, Whitman, in the final year of my research, and Caroline's endless energy and patience in raising him not only helped me tremendously during busy periods, but provided inspiration during the process of finishing this work. I'm incredibly grateful for Whitman and that he arrived during our time at Hopkins. While he didn't sleep as much as we might have hoped, it was delightful to come home to a happy, playful little boy every day and have such a perfect reason to spend time away from lab work and writing!

I am very thankful for the support of two tremendous advisors, Jonah Erlebacher and Bob Cammarata. Bob was my first advisor and sadly passed away in January 2016. He was an admired instructor, researcher, friend and comedian. It was an honor to work alongside and learn from him. I am very grateful to Jonah for the graciously provided opportunity to research in his group on so many interesting projects. Besides being a kind and always humorous advisor, it was great fun and always thought provoking to research in his lab. He selflessly directed research projects and ideas in a way that tremendously benefitted his students by balancing the necessary guidance to effectively

steer projects while also allowing students the full opportunity to explore their research and develop their abilities.

I appreciate the support of Professor Chao Wang and students in his group for assistance with laboratory research. Professor Karl Sieradzki of Arizona State University also provided great insight to several research projects presented within.

I am thankful to the staff of the Department of Materials Science and Engineering at JHU (Jeanine Majewski, Ada Simari, Bryan Crawford and Meg Tully in particular), who are instrumental in assisting the students during their studies and research.

Finally, I thank my parents, Sid and Diana; sister and brother-in law, Sydney and Shane; and mother-in-law, Linda for their support and encouragement throughout years of study. To my parents, I am thankful for educational opportunities they provided me through their own sacrifices. Sydney and Shane have always provided a model example to follow. To Linda, thank you for your everlasting encouragement and willingness to help Caroline and I raise Whitman.

This work would not have been possible without funding from the Department of Energy on award number DE-SC0008686. I am grateful for their generous support.

Table of Contents

List of Tables vii

List of Figures viii

Chapter 1 - Electrochemical Concepts 1

Chapter 2 - Nanoporous Copper Thin Films for CO_2 Reduction 17

Chapter 3 - Motivation for a Flow Cell for Sequential Electrolysis 66

Chapter 4 - Flow Cell for Sequential Electrolysis 81

Chapter 5 – Porous Niobium for Sequential HOR and HER 99

Chapter 6 – Electrochemical Ammonia Synthesis 153

Chapter 7 - Novel Mediators for Copper Electrodeposition in Recessed Features 156

Chapter 8 - Summary 187

Curriculum Vitae 190

List of Tables

Table 2-1. Measured roughness factors of NP-Cu films by Zn UPD. Cu-Zn samples were bonded at 350 C, and Cu-Al samples were bonded at 500 C.

Table 5-1. Calculated characteristics of HER working electrodes.

Table 7-1. Exchange current densities (j0) and Cathodic Symmetry Coefficients (🐦C*) as calculated by least squares fitting of Tafel data and current density ratios.*

List of Figures

Figure 1-1. Ideal current density versus potential curve for a cathodic reaction showing the three characteristic regions corresponding to variation in the rate limiting reaction step. The equilibrium potential is denoted E^0*.*

Figure 1-2. Plan view SEM image of nanoporous Cu synthesized by dealloying of brass in 3M H2SO4.

Figure 1-3. Schematic details of dealloying process. (a) Less noble elements [silver] dissolve from terrace sites. (b) Noble adatoms [gold] diffuse to more stable surface sites exposing the terrace beneath for further dissolution. (c) Initial ligaments form with characteristic length scales on the order of nm. (d) Ligaments are undercut leading to new connected porosity when insufficient noble adatoms are liberated to passivate ligament bases. (e) Characteristic length scales on the order of 10 nm are initially observed, (f) which can be coarsened by annealing or electrochemical cycling. Image courtesy of [1].

Figure 2-1. Annual worldwide CO2 emissions since 1980. Figure adapted from Ref [2].

Figure 2-2. Schematic of process used to create supported NP-Cu thin films by diffusion bonding of elemental foils followed by dealloying.

Figure 2-3. Phase diagrams of Cu-Al and Cu-Zn. The red lines denote the annealing temperatures used for diffusion bonding and formation of dealloyable intermetallic phases. The common shorthand symbols for the brass phases are denoted in green.

Figure 2-4. Images of NP-Cu films supported on Cu foil synthesized by dealloying of diffusion couples.

Figure 2-5. Sectional micrographs of Cu mesh and Zn foil after annealing at 350 C for 20 minutes prior to dealloying (left) and after dealloying (right) in 3M H2SO4.

Figure 2-6. Sectional micrographs of Cu and Al foils after annealing at 500 C for 240 minutes prior to dealloying (left) and after dealloying (right) in 1M HCl.

Figure 2-7. Plan view SEM micrographs of NP-Cu synthesized from dealloyed Cu-Al in the noted electrolytes.

Figure 2-8. Plan view SEM micrographs of NP-Cu synthesized from Cu-Zn parent supported on Cu mesh and dealloyed in 3M H2SO4.

Figure 2-9. Plan view SEM micrographs of NP-Cu synthesized from dealloyed Cu-Zn (annealed for 20 minutes at 350 C unless noted) supported on Cu mesh in the noted electrolytes.

Figure 2-10. Open circuit potential versus time for dealloying in 1M H2SO4 of Cu/Zn bonded at 350 C for 18 min. The dashed red line denotes the open circuit potential of pure Cu in the electrolyte.

Figure 2-11. Cyclic voltammograms (50 mV/sec) of Cu mesh in 250 mM K2SO4 with and without ZnSO4 as indicated.

Figure 2-12. Cyclic voltammograms (50 mV/sec) in 250 mM K2SO4 + 10 mM ZnSO4 of NP-Cu formed by diffusion bonding Cu-Zn at 350 C for the noted times.

Figure 2-13. Cyclic voltammograms (50 mV/sec) in 250 mM K2SO4 + 10 mM ZnSO4 of NP-Cu formed by diffusion bonding Cu-Zn at 350 C for 20 minutes and subsequently dealloyed in the noted electrolytes.

Figure 2-14. Faradaic efficiencies of CO2RR with NP-Cu thin films derived from Cu-Al: A) dealloyed in 1M KOH, B) dealloyed in 1M HCl, C) dealloyed in 1M HCl and impregnated with [M3BN][Tf2N], and D) dealloyed in 1M HCl and impregnated with [BMIM][PF6]. The balance of the FE leading to 100% total efficiency was H2.

Figure 2-15. Partial current densities for CO2RR products on NP-Cu catalyst derived from Cu-Al and dealloyed in 1M KOH.

Figure 3-1. Trends in world population and Haber-Bosch derived nitrogen use in the 20th century. Figure reproduced from [2].

Figure 4-1. The flow cell as assembled.

Figure 4-2. Sectional diagram of the flow cell. Blue shapes represent the HDPE plates. Note that gaskets placed between the plates to seal the flow channel are omitted for simplicity.

Figure 4-3. Circuit diagram of the flow cell highlighting the HOR current and uncompensated HER resistance responsible for the potential shift observed at the HER cell due to applied current in the HOR cell. Paths and currents shown in blue represent those in the electrolyte. The working, counter and reference electrodes are denoted WE, CE and RE respectively.

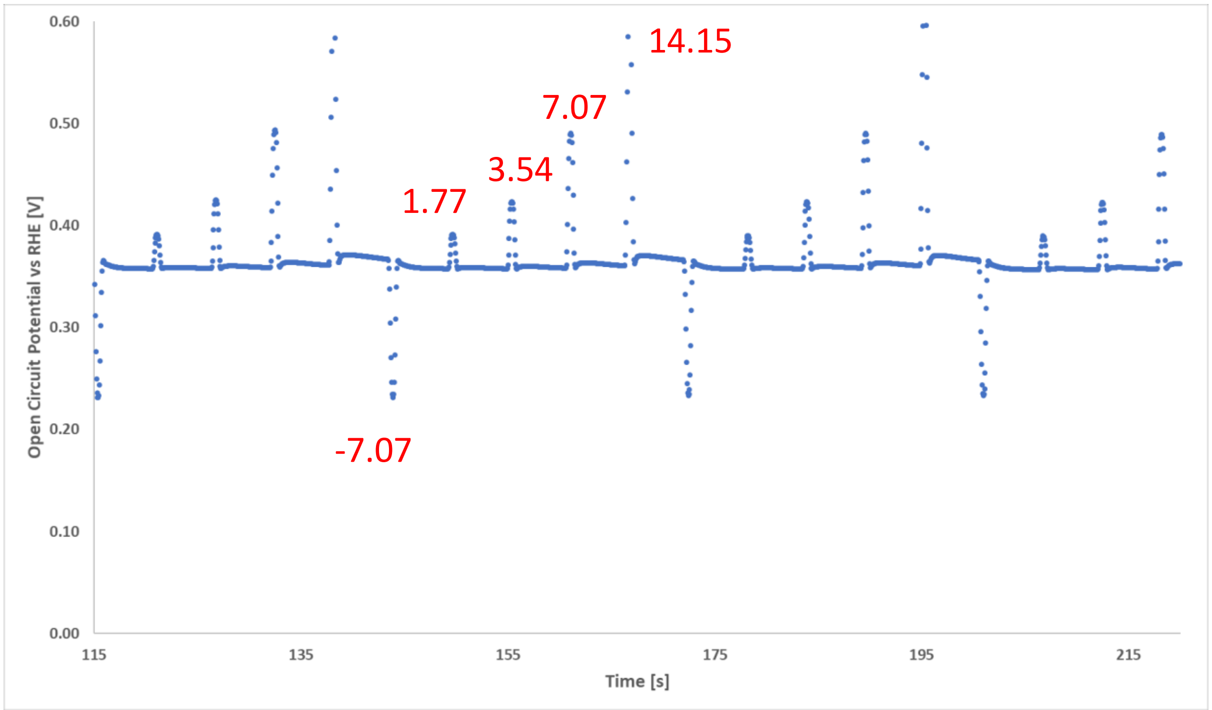

Figure 4-4. Open circuit potential of a porous Nb sample at the HER working electrode while the HOR working electrode (Pt mesh) was pulsed to the current densities noted in red (in mA/cm2) from a baseline HOR current of 0 mA/cm2. The electrolyte was H2 saturated.

Figure 4-5. Open circuit potential shift at a porous Nb HER working electrode as a function of applied HOR current density obtained from the data in Figure 4-4.

Figure 4-6. Open circuit potential of a Pt mesh electrode as function of time under the noted flow rates in H2 saturated electrolyte.

Figure 4-7. Cyclic voltammograms (50 mV/sec) of a porous Nb HER working electrode in H2 saturated electrolyte with the upstream HOR working electrode operating at the noted current densities. These data were not shifted to account for the effects of the HOR cell current passing through the HER cell.

Figure 4-8. Cyclic voltammograms from Figure 4-7 with the potentials shifted to account for the effects of the HOR current passing through the HER cell.

Figure 5-1. Plan view SEM micrograph of porous Nb. The white arrows mark Nb silicides located throughout the sample that provided mechanical stability.

Figure 5-2. Cyclic voltammetry curves measured on porous Nb in the flow cell in N2 saturated 100 mM K2SO4 with no flow at the scan rates indicated.

Figure 5-3. Plot of the average current difference between the linear portion of the anodic and cathodic sweeps during cyclic voltammetry measurements from previous figure as a function of the scan rate.

Figure 5-4. SEM micrograph of the surface of an interior Nb ligament after Pt deposition. The ligament was exposed by fracturing the Nb sample immediately prior to imaging. Finely dispersed particles were observed on the surface of the ligament.

Figure 5-5. Cyclic voltammetry measurements (50 mV/s) on a stack of 4 Pt meshes in the flow cell at flow rate of 40 mL/min in electrolytes purged with H2 and N2 as indicated.

Figure 5-6. Cyclic voltammograms (50 mV/sec) of porous Nb HER working electrode in H2 saturated 1M Na2SO4 with the upstream HOR working electrode operating at the noted current densities.

Figure 5-7. Cyclic voltammograms (50 mV/sec) of porous NbPt HER working electrode in H2 saturated 1M Na2SO4 with the upstream HOR working electrode operating at the noted current densities.

Figure 5-8. Cyclic voltammograms (50 mV/sec, average of 2 CV cycles) of stack of 6 Pt mesh HER working electrode in H2 saturated 1M Na2SO4 with the upstream HOR working electrode operating at the noted current densities.

Figure 5-9. Cyclic voltammograms (50 mV/sec) of stainless-steel mesh HER working electrode in H2 saturated 1M Na2SO4 with the upstream HOR working electrode operating at the noted current densities.

Figure 5-10. Negative going sweep from slow cyclic voltammograms (5 mV/sec) of porous Nb HER working electrode in H2 saturated 1M Na2SO4 with the upstream HOR working electrode operating at the noted current densities. The plotted curves are an average of 4 CV's.

Figure 5-11. Negative going sweep from slow cyclic voltammograms (5 mV/sec) of porous NbPt HER working electrode in H2 saturated 1M Na2SO4 with the upstream HOR working electrode operating at the noted current densities. The plotted curves are an average of 3 CV's.

Figure 5-12. Negative going sweep from slow cyclic voltammograms (5 mV/sec) of 6 Pt mesh HER working electrode in H2 saturated 1M Na2SO4 with the upstream HOR working electrode operating at the noted current densities. The plotted curves are an average of 4 CV's.

Figure 5-13. Negative going sweep from slow cyclic voltammograms (5 mV/sec) of stainless-steel mesh working electrode in H2 saturated 1M Na2SO4 with the upstream HOR working electrode operating at the noted current densities. The plotted curves are an average of 4 CV's.

Figure 5-14. The excess HER current density (compared to the curve obtained at negligible applied HOR current density) versus applied potential using the porous Nb working electrode as a function of the noted HOR current densities. These data were calculated from the negative going sweeps of 5 mV/sec CV's in H2 saturated 1M Na2SO4.

Figure 5-15. The excess HER current density (compared to the curve obtained at negligible applied HOR current density) versus applied potential using the porous NbPt working electrode as a function of the noted HOR current densities. These data were calculated from the negative going sweeps of 5 mV/sec CV's in H2 saturated 1M Na2SO4.

Figure 5-16. The HOR to HER conversion efficiency versus applied potential using the porous Nb working electrode as a function of the noted HOR current densities. These data were calculated from the excess current densities of 5 mV/sec CV's in H2 saturated 1M Na2SO4.

Figure 5-17. The HOR to HER conversion efficiency versus applied potential using the porous NbPt working electrode as a function of the noted HOR current densities. These data were calculated from the excess current densities of 5 mV/sec CV's in H2 saturated 1M Na2SO4.

Figure 5-18. Tafel plot of negative going sweep of 5 mV/sec CV of Nb in H2 saturated 1M Na2SO4.

Figure 5-19. Tafel plot of negative going sweep of 5 mV/sec CV of NbPt in H2 saturated 1M Na2SO4.

Figure 5-20. Cyclic voltammograms (scan rate of 50 mV/sec) of 3 and 6 mesh Pt electrodes in H2 saturated 1M Na2SO4.

Figure 5-21. Cyclic voltammetry measurement from NbPt electrode in H2 and N2 saturated 1M Na2SO4 at 50 mV/s scan rate and 40 mL/min flow rate.

Figure 5-22. Equilibrium potential of NbPt electrode as determined from Tafel plots of slow CV data as a function of the theoretical pH of the electrode due to the upstream HOR oxidation current.

Figure 5-23. Calculated Pourbaix diagram for Niobium-H2O system. Lines a and b show the potentials corresponding to reductive and oxidative reactions of H2O. Figure adapted from Asselin, et. al [28].

Figure 7-1 Cyclic voltammetry measurements from 0.190 M CuSO4 + 0.007 M H2SO4 + HOAc (a) and 0.190 M CuSO4 + 0.007 M H2SO4 + HTar (b) on the Cu foil electrode. All scans obtained at 10 mV/sec. Adapted from Ref. [31].

Figure 7-2. Cyclic voltammetry measurements from 0.15 M $Cu(ClO4)_2$ *with and without PbClO4 on the Cu foil electrode. All scans obtained at 10 mV/sec. Adapted from Ref. [31].*

Figure 7-3. Sectional SEM micrographs of Cu films deposited from 0.30 M CuSO4 + 0.79 M HOAc [pH = 2.25] for 155 sec at 80 mV overpotential (a), 84 sec at 120 mV overpotential (b), and 54 sec at 200 mV overpotential (c). Figure from Ref. [31].

Figure 7-4. Sectional SEM micrographs of Cu films deposited from 0.19 M CuSO4 + 0.16M HTar [pH = 2.26] for 229 sec at 40 mV overpotential (a), 125 sec at 80 mV overpotential (b), and 14 sec at 500 mV overpotential (c). Figure from Ref. [31].

Figure 7-5. Sectional SEM micrograph of Cu film deposited from 0.19 M CuSO4 + 0.009 M H2SO4 [pH = 2.26] for 49 sec at 160 mV overpotential. Figure from Ref. [31].

Figure 7-6. Sectional SEM micrographs of Cu films deposited from 0.30 M CuSO4 + 0.79 M HOAc for 84 sec (a) and 163 sec (b) at 120 mV overpotential. Figure from Ref. [31].

Figure 7-7. Sectional SEM micrographs of Cu films deposited from 0.19 M $Cu(OAc)_2$ *+ 0.12 M HOAc + 0.38 M H2SO4 [pH =2.12] for for 15 sec (a), 29 sec (b), and 120 sec (c) at 240 mV overpotential. Figure from Ref. [31].*

Figure 7-8. Sectional SEM micrographs of Cu films deposited from 0.30 M CuSO4 + 0.79 M HTar for 229 sec (a), 455 sec (b), and 1011 sec (c) at 40 mV overpotential. Figure from Ref. [31].

Figure 7-9. Sectional SEM micrographs of Cu films deposited from 0.19 M $Cu(OAc)_2$ *+ 0.12 M HOAc + 0.38 M H2SO4 for 60 sec at 120 mV overpotential followed by 20 sec (a) and 60 sec (b) at 600 mV overpotential. Figure from Ref. [31].*

Figure 7-10. Sectional SEM micrographs of Cu films deposited galvanostatically at current density of 5 mA/cm2 from 0.19 M $Cu(OAc)_2$ *+0.12 M HOAc+0.38 M H2SO4 for 45 sec (a), 60 sec (b), and 150 sec (c). Figure from Ref. [31].*

Figure 7-11. Sectional SEM micrographs of Cu films deposited galvanostatically at current density of 8 mA/cm2 from 0.19 M Cu(OAc)2 +0.12 M HOAc+0.38 M H2SO4 for 15 sec (a), 30 sec (b), and 120 sec (c). The white arrows denote center seam defects common to films with conformal deposition across the profile. Figure from Ref. [31].

Figure 7-12 Sectional SEM micrographs of copper films deposited from 0.15 M $Cu(ClO4)_2$ *for 34 sec at trenches of varying widths (a) and (b) and 0.15 M* $Cu(ClO4)_2$ *+ 0.30 M PbClO4 for 9.3 (c)* *and 54 sec (d). All depositions were potentiostatic at -690 mV vs MSE. The white arrows denote center seam defects common to films with conformal deposition across the profile. Figure from Ref. [31].*

Figure 7-13. Tafel plots of Cu current density at the various sections of the trench features as calculated by thickness measurements from sectional SEM micrographs from 0.30 M CuSO4 + 0.79 M HOAc, (a), 0.19 M Cu(OAc)$_{2+}$ *0.12 M HOAc + 0.38 M H2SO4 (b), 0.19 M Cu(OAc)*$_{2+}$ *0.12 M HOAc + 0.40 M H2SO4 (c), and 0.19 M CuSO4 + 0.016 M HTar electrolytes. Figure adapted from Ref [31].*

Figure 7-14. Ratios of the bottom/sidewall current densities in the patterned trenches as a function of Cu2+/Cu overpotential from several organic acid containing electrolytes. Figure adapted from Ref [31].

Figure 7-15. Least squares fitting result (shown by solid lines) overlaid on the Tafel data (a) current density ratios (b) as a function of overpotential for Cu2+/Cu reduction for films deposited from 0.19 M Cu(OAc)$_{2+}$ *0.12 M HOAc + 0.40 M H2SO4. Adapted from Ref [31].*

Chapter 1 - Electrochemical Concepts

A recurring theme in the majority of the research presented in this work is applied electrochemistry of nanoporous materials. The research involving nanoporous materials focuses on synthesis and electrocatalytic application of porous materials created by dissolution of one or more components from a parent phase leaving behind a characteristic structure of the non-dissolving components. This introduction serves as a brief discussion of the fundamentals and concepts of these topics which are explored in greater detail within the research presented later.

An electrochemical reaction is a chemical reaction which also involves transfer of charge with the reacting species. The reaction is commonly carried out with a charged solid electrode submerged in a liquid electrolyte where ionic species in the electrolyte react and exchange charge at electrode/electrolyte interface during the electrochemical reaction. Using the common convention, a reduction reaction occurs when an electron passes from the charged electrode to the ionic species, and an oxidation reaction occurs when the electron passes from the ionic species to the charged electrode. Equation 1.1 gives a generic reduction reaction (the oxidation reaction is simply the reaction in the opposite direction), where M^{z+} represents the ionic species that is reduced during the reaction, e^- represents electrons transferred from the electrode to the ionic species and M represents the reduced product. The reaction shows complete reduction of the ionic reactant, but partial reduction is also common.

$$M_{aq}^{z+} + ze^{-} \rightarrow M_{s,l,g} \tag{1.1}$$

The electrochemical potential of the reactants, products or electrons (individual species denoted x) can be defined in standard thermodynamic terms according to Equation 1.2.

$$\mu_x = \mu_x^0 + RT \ln a_x - zFE_x \tag{1.2}$$

Where: μ = electrochemical potential, μ^0 = electrochemical potential at STP, R = ideal gas constant, T = temperature, a = activity, F = Faraday's Constant and E = electric potential. At equilibrium, the change in electrochemical potential during the reduction reaction is equal to zero. As a result of the equilibrium condition, we can write Equation 1.3.

$$\mu_M = \mu_{M^{z+}} + \mu_{e^-} \tag{1.3}$$

Substituting in Equation 1.2 for each species and solving for the potential difference between the electrolyte and charged electrode (while noting the charge on the solid atom is 0 in this case) yields Equation 1.4.

$$zF\left(E_{aq} - E_s\right) = \left(\mu_{M^{z+}}^0 + \mu_{e^-}^0 - \mu_M^0\right) + RT \ln\left(\frac{a_{M^{z+}} a_{e-}^{z}}{a_M}\right) \tag{1.4}$$

By grouping terms, the classic Nernst Equation that defines the reduction potential of the reduction reaction relative to a reference electrodes in terms of activities of its oxidized and reduced species is revealed according to Equation 1.5.

$$E = E^0 + \frac{RT}{zF}\ln\left(\frac{a_O}{a_R}\right) \tag{1.5}$$

Where: E = reduction potential and E^0 = standard reduction potential (when all activities = 1). The Nernst Equation marks the equilibrium potential (E_{eq}) for given reactant and product activities at which there is no net reduction or oxidation of the reacting species. When discussing elemental or solid species, the magnitude of the equilibrium potential provides a benchmark for the nobility of a material. Materials with large positive equilibrium potentials are noble and favor the reduced state when exposed to electrolyte, while materials with large negative equilibrium potential favor the oxidized state (or oxidize to passive compounds in some cases). When measuring the potential difference at the electrode/solution interface, if the potential at the electrode is less than the reduction potential as indicated by the Nernst Equation the ions in solution will spontaneously reduce at the electrode (assuming no kinetic barriers). If the potential at the electrode is greater than the reduction potential of the electrode material or reduced ions in solution, solid material at the working electrode will dissolve (or oxidize) to form ions while reduced ions will oxidize. This behavioral dependence on potential stems from the thermodynamic considerations and allows for experimental control over the reaction taking place at the electrode.

So far, the potential at the electrode has been described as a difference between the electrode and the electrolyte. In practice, it is not possible to directly measure the potential difference across the electrode/electrolyte interface. To form a complete circuit required to measure the potential with a standard voltmeter, a second electrode must be placed in electrical contact with the electrolyte. Any material chosen as the second electrode will have its own inherent potential difference with the electrolyte, just as the electrode of interest where the electrochemical reaction we wish to control and measure occurs (this electrode of interest is often referred to as the working electrode).

Since a voltmeter is limited to measure only the potential difference between the two electrodes, common conventions for electrochemical cells have been developed to accurately measure the absolute potential at the working electrode. At the most basic level, a complete electrochemical cell requires only two electrodes, with a reduction reaction occurring at one electrode (the cathode) and an oxidation reaction occurring at the other (the anode). In the research described later, we are primarily interested in the details of the reaction at the working electrode, and the second electrode (termed the counter electrode) is present to pass charge. The same amount of charge is passed at each electrode and current must pass through the electrolyte by ionic species to maintain charge neutrality. A potentiostat is typically connected in the circuit outside of the electrolyte to control and measure characteristics of the electrochemical reaction. Accurate control and measurement of the potential at the working electrode is paramount to obtaining accurate results, and important measures are taken to minimize error in the potential measurement. Measuring the potential relative to the counter can seem like a natural choice, however there is inherent ohmic resistance in the electrolyte and a necessary potential drop across the electrolyte between the working and counter electrodes due to current passing through the electrolyte across this resistance. This potential drop varies with passed current and can comprise a significant portion of the measured potential difference between the working and counter electrodes which typically makes measurement of the potential drop between the working and counter electrodes an undesirable way to accurately measure the potential at the working electrode.

Most commonly, a third electrode (termed the reference electrode) is immersed in the electrolyte. This electrode is chosen to have a stable potential, and the potentiostat allows a negligible amount current to pass through this electrode during experiments. The potential is then measured between the stable reference electrode and the working electrode allowing for precise control and measurement of the potential difference between the electrolyte and working electrode. The absolute potential of the working electrode (rather than a potential difference between the working and reference) is often calculated based off the potential of the hydrogen electrode. By definition, the reversible hydrogen electrode has a potential of zero in any electrolyte and corresponds to the potential required to reduce hydronium ions or water to hydrogen (depending on pH) at 1 atm pressure. Conventional reference electrodes can be calibrated to this scale, allowing for precise measurement of the absolute potential on a fixed scale in an electrochemical experiment.

While the Nernst equation describes the thermodynamic relation between potential and activity at the working electrode, it does not describe kinetic aspects or rates of the electrochemical reactions. To find the governing equations for the reaction rates, we first consider the dependence of the change in Gibbs free energy based on the electric potential of the cell (Equation 1.6) which is the governing thermodynamic potential for an electrochemical reaction under constant temperature and pressure (the conditions we use for all experiments in the research presented in this work).

$$\Delta G = -zF\Delta E \tag{1.6}$$

If we consider a general reaction rate (k) to have a classic Arrhenius form (Equation 1.7) we can substitute Equation 1.6 to yield the measured current density dependence (j) on deviation from the Nernst potential as shown in Equation 1.7.

$$j = zFCk^0 \exp\left(-\frac{\Delta G}{RT}\right) = zFCk^0 \exp\left(\frac{zF\left(E^{appl} - E^{eq}\right)}{RT}\right) \tag{1.7}$$

Where (k^0) = rate constant, and (C) = concentration of the reacting species. At this point it is helpful to define the overpotential (η) which is the excess potential driving the electrochemical reaction as shown in Equation 1.8.

$$\eta = E^{appl} - E^{eq} \tag{1.8}$$

When both the forward (j_f) and backward (j_b) current densities are considered to yield the net current density (j_{net}), the dependence of the measured current density in the cell as a function of overpotential can be written as shown in Equation 1.9.

$$j_{net} = -j_f + j_b = -zFC_{ox}k^0 \exp\left(-\frac{zF\alpha_c\eta}{RT}\right) + zFC_{red}k^0 \exp\left(\frac{zF(1-\alpha_c)\eta}{RT}\right) \tag{1.9}$$

Where: α_c = symmetry parameter which ranges from 0 to 1 for a single step electrochemical reaction as shown, C_{ox} = concentration of oxidized species and C_{red} = concentration of reduced species.

When the concentration of species at the electrode is equal to that in the bulk electrode (such as a dilute solution). Equation 1.9 simplifies to Equation 1.10 which is the classic Butler-Volmer equation describing electrochemical reaction rates as a function of overpotential. At a net reaction rate of zero this equation also can be rearranged to the Nernst Equation, fulfilling the requirement that a valid kinetic equation satisfies the thermodynamic conditions at equilibrium.

$$j_{net} = j^0\left[-\exp\left(-\frac{zF\alpha_c\eta}{RT}\right) + \exp\left(\frac{zF(1-\alpha_c)\eta}{RT}\right)\right] \tag{1.10}$$

The exchange current density (j^0) represents the reduction and oxidation rate at equilibrium (zero net current). The symmetry term is introduced to reflect that the geometry of the free energy surfaces near the minima corresponding to the reactant and product states are not necessarily symmetric. If we consider decreasing the applied potential at the working electrode to favor the reduction reaction, the symmetry considerations reflect that a change in free energy due to a change the in applied potential at the working electrode might not be distributed equally as a reduction in the free energy barrier for the reduction reaction along with an increase in the free energy barrier for the oxidation reaction, but rather could have an asymmetric distribution. This constant can be calculated from Tafel style plots of current density versus the logarithm of applied potential, as we will discuss in later work.

Characteristic current versus applied potential curves as measured at an electrode have three primary regions determined by the rate limiting reaction step as illustrated for a cathodic electrochemical reaction in Figure 1-1. At very low overpotentials, in the activation-controlled region, the reaction rate is rate limited by the rate of charge transfer at the electrode interface and shows exponential dependence on the overpotential. At very large overpotentials in the transport limited range, the reaction rate is constant with increasing overpotential as the charge transfer is fast compared to the rate limiting step which is the potential independent rate at which reactants arrive and products leave the electrode. At moderate overpotentials in the mixed regime, the rates of charge transfer and mass transport are similar so both contribute meaningfully to determining the rate limiting step in the reaction.

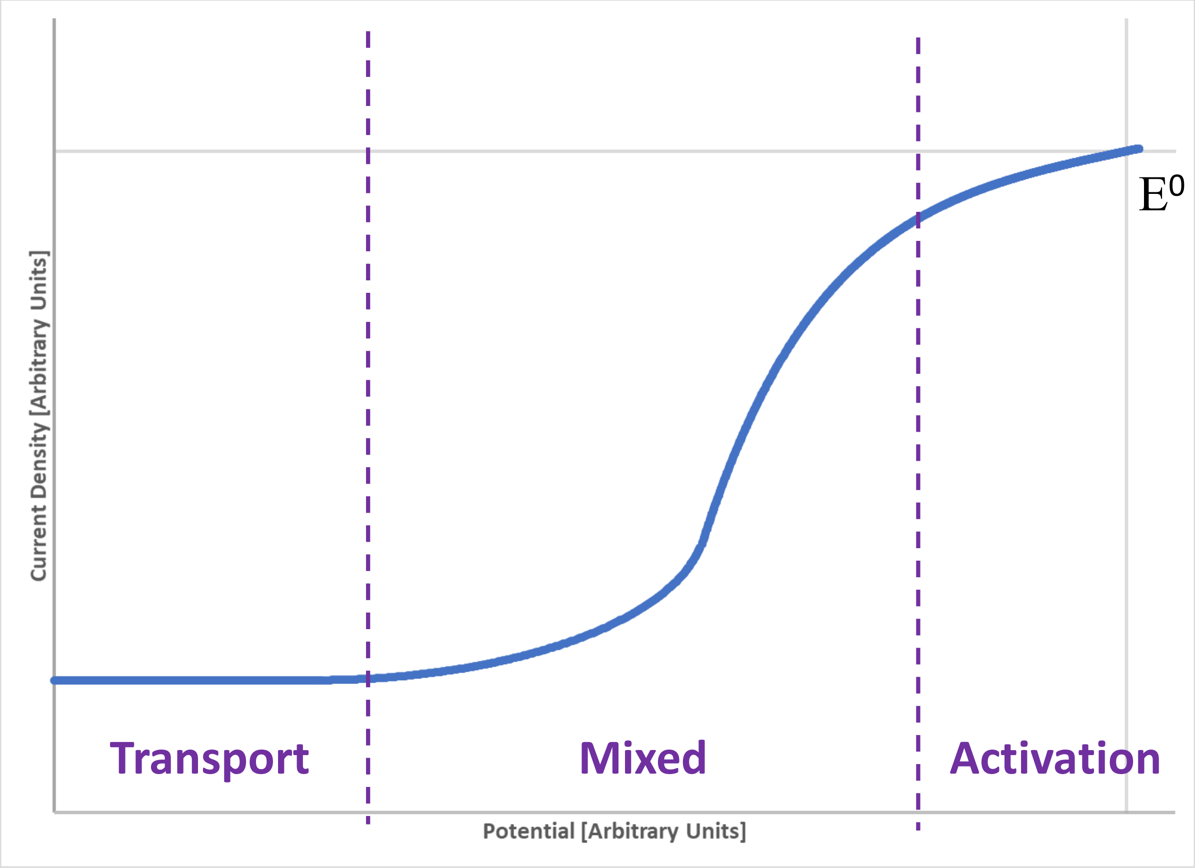

Figure 1-1. Ideal current density versus potential curve for a cathodic reaction showing the three characteristic regions corresponding to variation in the rate limiting reaction step. The equilibrium potential is denoted E^0.

The synthesis of nanoporous materials often draws on the fundamentals of electrochemistry described above. In this work, a nanoporous (NP) material refers to a specific type of porous material formed by removal of one or more components from a parent phase containing two or more components. One or more of the components remain to form the characteristic structure of the nanoporous material (shown in Figure 1-2), which is a bicontinuous network of open porosity with connected ligaments of the remaining material. In addition to the network of open porosity, these materials have unique structural features relative to other nanoscale materials.

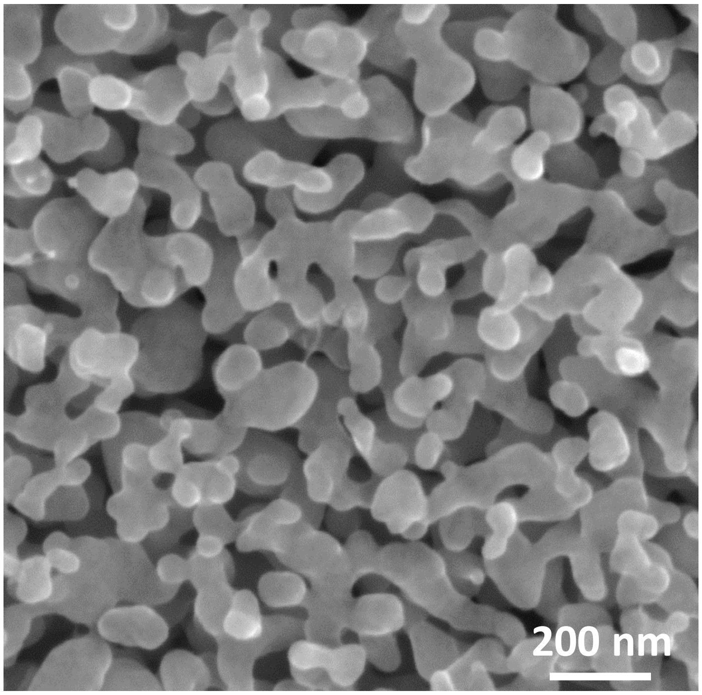

Figure 1-2. Plan view SEM image of nanoporous Cu synthesized by dealloying of brass in 3M H_2SO_4.

The mechanism for formation of the NP structure is as follows (see Figure 1-3). The multicomponent parent material is placed under conditions where dissolution of one or more components is thermodynamically favorable. The discussion will be simplified by considering immersing an AB parent material (where A represents noble atoms and B non-noble atoms) in an electrolyte where the non-noble B atoms dissolve to form ions in solution. At the interface of the parent material and the electrolyte, dissolution of B atoms from terraces is the rate limiting step in formation of the NP material. When a terrace B atom dissolves, the terrace vacancy left behind allows for rapid solvation and dissolution of any B atoms neighboring the vacancy. This process repeats across the terrace leaving behind a large concentration of A adatoms on the surface. In solution, these A atoms quickly diffuse to step edges where they passivate the step edges from further dissolution. The rate of surface diffusivity is the other key rate determining step in the process, as it determines the scale of the porosity and composition of the ligaments (greater diffusivity yields larger feature sizes with less non-noble component remaining). The newly exposed surface beneath the previous terrace undergoes the same dissolution process. The A adatoms attach to edges that are an atomic spacing extended into the exposed terrace compared to the layer above, and mounds of passivated material with widening bases form, eventually forming the characteristic network of ligaments. As the terrace dissolution/adatom diffusion process repeats, the bases of the growing ligaments expand, and eventually insufficient A adatoms are liberated from surrounding terraces to passivate the expanding network of step edges around the base of the ligaments. At this point, new porosity bifurcates into the mound, and the connected network of porosity characteristic to NP materials forms in this manner.

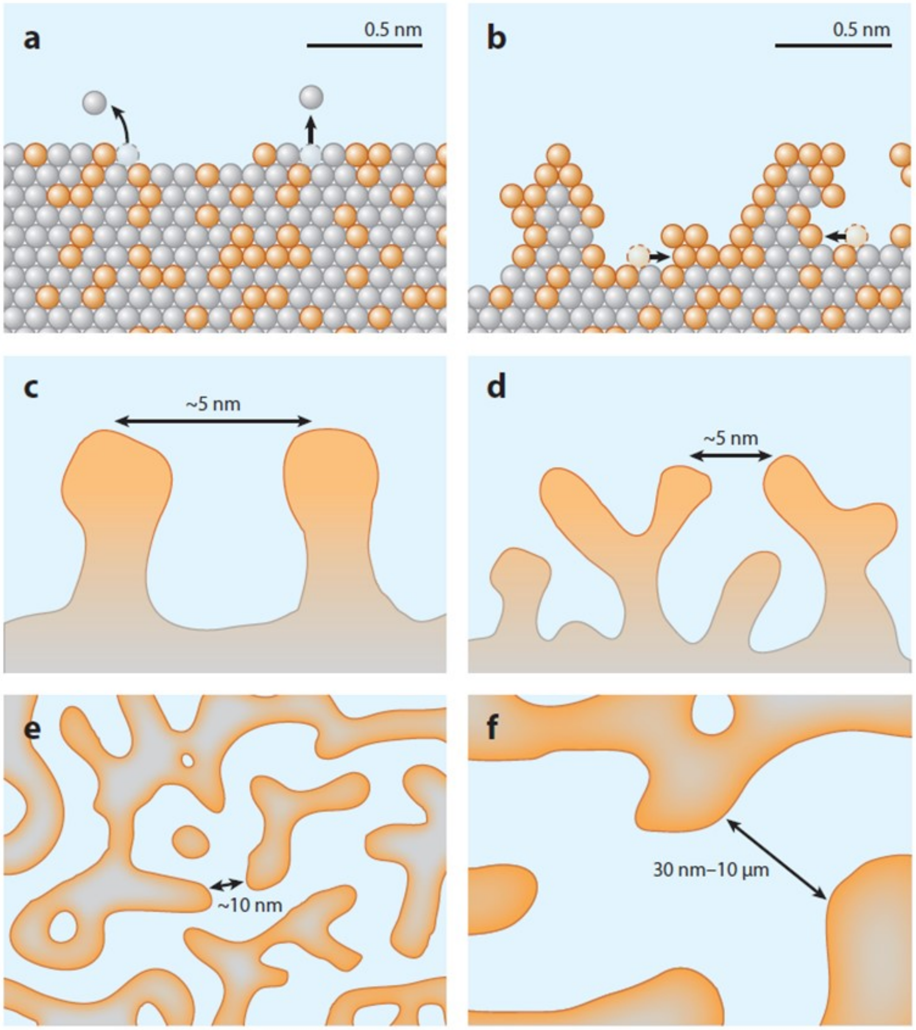

Figure 1-3. Schematic details of dealloying process. (a) Less noble elements [silver] dissolve from terrace sites. (b) Noble adatoms [gold] diffuse to more stable surface sites exposing the terrace beneath for further dissolution. (c) Initial ligaments form with characteristic length scales on the order of nm. (d) Ligaments are undercut leading to new connected porosity when insufficient noble adatoms are liberated to passivate ligament bases. (e) Characteristic length scales on the order of 10 nm are initially observed, (f) which can be coarsened by annealing or electrochemical cycling. Image courtesy of [1].

The characteristic ligament and pore size that forms for dissolution at room temperature for precious metals that have been successfully dealloyed (including Au, Pt, Ag, Cu and Ni) is on the order of 5 to 50 nm [1]. The feature size is a function of homologous temperature (fraction of the dealloying temperature relative to the melting temperature), with higher melting point materials having lower surface diffusivities at a given temperature and therefore forming finer features [2]. The NP structure can be coarsened by annealing or electrochemical cycling, as both processes drive surface diffusion and cause coarsening as the material eliminates surface area and its associated surface energy. Typical NP metals can be coarsened to the scale of tens of microns. It is also important to note that the ligaments may not be pure A material. The interior can consist of A and B atoms, with A atoms passivating the outer surface.

The structure of the nanoporous material that forms is unique from other forms of nanostructures in several ways, and these differences make NP materials attractive for many applications. The nanoporous material is bicontinuous with the solid ligaments forming a connected structure, and the porosity is open and bicontinuous. The nanoporous structure retains the grain structure of the parent material, so the resulting material is large grains of connected single crystals, each grain being itself nanoporous material. Because the dealloyed structure is not a sintered agglomeration of nanoparticles, the dealloying process leads to the formation of areas of positive and negative curvature as well as saddle points with zero curvature on the surface of the ligaments, while solid nanostructures tend to have areas of positive curvature (and possibly negative for open, hollow structures such as nanowires). Since catalytic selectivity and efficiency can be sensitive to the surface structure of the catalyst, these unique surface structures may lead to exposure of uncommonly observed crystallographic planes and steps beneficial for a specific catalytic reaction that aren't available on other nanostructures. The open porosity inherent to a nanoporous material also lends itself to mass transport effects on catalysis that aren't necessarily available on non-porous or smoother nanostructures.

The composition of a parent material that can be dealloyed electrochemically is typically limited to approximately 15-40 atomic percent of the noble element [1]. At lower concentrations of A, the parent material temporarily dissolves and redeposits as discrete particles rather than forming the typical connected structure with all types of surface curvature. There also exists an upper limit on the concentration of A, termed the parting limit, at which the exposed A atoms during dissolution fully passivate the surface of the parent material at the interface with the electrolyte and halt the dealloying process.

In our theoretical example dissolution of the less noble element was driven by free corrosion in an appropriate electrolyte. In an electrolyte, the corrosion can be driven by or assisted by application of a potential to the parent material. The applied potential allows for tighter control of the dissolution rate compared to free corrosion, as the rate is potential dependent and can be set externally. Sufficient anodic overpotential to drive dissolution from terraces is required to drive dealloying under such conditions, and the onset potential of significant dissolution is termed the critical potential.

More recently a new technique termed Liquid Metal Dealloying (LMD) has been discovered that allows for synthesis of refractory NP-metals such as Nb and Ta that have not been formed by electrochemical dealloying [3], [4]. In this process, the parent material is immersed in a molten bath of one or more additional elements held at a temperature where the parent material remains solid. Only one or more of the elements in the parent material is soluble in the melt, and these element(s) dissolve into solution leaving behind the insoluble element as a nanoporous material with the characteristic bicontinuous structure described above. In this work, we have used LMD to synthesize np-Nb for use in our electrochemistry experiments.

References

[1] I. McCue, E. Benn, B. Gaskey, and J. Erlebacher, “Dealloying and Dealloyed Materials,” *Annu. Rev. Mater. Res.*, vol. 46, no. 1, pp. 263–286, Jul. 2016.

[2] Q. Chen and K. Sieradzki, “Spontaneous evolution of bicontinuous nanostructures in dealloyed Li-based systems,” *Nat. Mater.*, vol. 12, no. 12, pp. 1102–1106, Dec. 2013.

[3] P.-A. Geslin, I. McCue, B. Gaskey, J. Erlebacher, and A. Karma, “Topology-generating interfacial pattern formation during liquid metal dealloying,” *Nat. Commun.*, vol. 6, no. 1, p. 8887, Dec. 2015.

[4] I. McCue, B. Gaskey, P.-A. Geslin, A. Karma, and J. Erlebacher, “Kinetics and morphological evolution of liquid metal dealloying,” *Acta Mater.*, vol. 115, pp. 10–23, Aug. 2016.

Chapter 2 - Nanoporous Copper Thin Films for CO_2 Reduction

Introduction

A recent report from the Intergovernmental Panel on Climate Change (IPCC) documenting possible scenarios to limit average global temperature rise to 1.5 C due to anthropogenic greenhouse gas emissions projects the use of carbon dioxide removal (CDR) technologies in all emissions scenarios that would achieve this goal [1]. The report indicates that emissions scenarios that don’t include substantial reduction in CO_2 emissions by 2030 will have to rely on CDR to a greater extent to limit global temperature rise in the 21st century. The most recent data (Figure 2-1) show that annual CO_2 emissions have grown at a slower rate than earlier in the century and may be peaking with decreased emissions to follow, but absent large decreases in the near future as forecast by the most optimistic IPCC scenarios CDR technologies will be needed to reach the 1.5 C warming benchmark [1], [2].

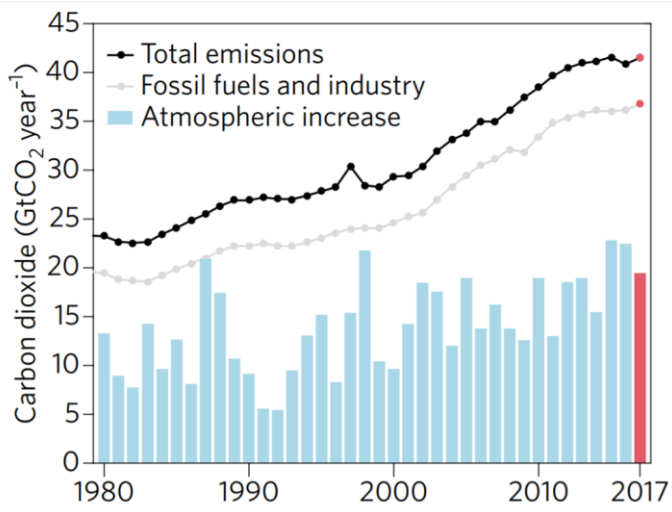

Figure 2-1. Annual worldwide CO2 emissions since 1980. Figure adapted from Ref [2].

While several CDR technologies exist, electrochemical reduction of CO_2 to carbon based fuels has generated a great deal of research interest in recent years as this process could be powered with alternative energy sources to provide an emission free cycle for fuel synthesis [3]. Electrochemical reduction of CO_2 (CO2RR) over a heterogeneous catalyst at economically viable current densities is challenging since current catalyst technologies do not provide sufficient selectivity, activity or durability for realistic employment at industrial scale. As a result researchers are actively searching for a viable catalyst, and copper based catalysts are a prime focus since Cu is the only known elemental catalyst that forms valuable hydrocarbons, alcohols and other higher order products (containing multiple carbon atoms) at non-negligible rates [4]–[7]. The ideal catalyst for CO2RR would selectively produce valuable chemicals (such as hydrocarbons or alcohols for fuels) at low overpotentials (many of the desirable CO_2

reduction reactions have equilibrium potentials within 100 mV versus RHE at moderate pH) such that renewable energy sources could power the CO2RR. The carbon containing products formed by a Cu catalyst include carbon monoxide (CO), formate species ($CHOO^-$ or CHOOH), formaldehyde (CH_2O), oxalate species ($C_2O_4^{2-}$ or $H_2C_2O_4$), methane (CH_4), ethane (C_2H_6), ethylene (C_2H_4), ethanol ($C2H_5OH$) and other higher order alcohols in minor quantities. Carbon monoxide and formate species are formed by other metals, but these products are generally considered less desirable as their practical use at industrial scales requires further processing to make more valuable fuels. In addition to carbon containing species, the competitive and detrimental hydrogen evolution reaction (HER) due to water and proton reduction occurs at Cu catalysts in the potential range of CO2RR. This undesirable side reaction limits the efficiency of Cu catalysts for CO_2 reduction, and preventing HER is a primary concern in development of selective CO2RR electrocatalysts.

Copper is abundant and inexpensive adding to its an attractiveness as a CO2RR catalyst. However, a suitable Cu catalyst for large scale CO2RR remains undiscovered due to non-optimal selectivity towards one of the more useful fuel products, activity and durability. Many forms of Cu catalysts generate multiple products in addition to hydrogen, and the most desirable products are often generated at large overpotentials requiring inefficient use of the input energy.

Cu based catalysts have been extensively evaluated and modeled in many forms as an electrocatalyst for CO2RR (and CO reduction) with the aim of discovering a form with sufficient selectivity, activity and durability for economically viable production of a valuable product [4]–[53]. Single crystal Cu surfaces can exhibit large Faradaic efficiency (FE) for valuable carbon products, and detailed research has shown that the selectivity and efficiencies of Cu surfaces are greatly influenced by crystallographic structure of the catalyst surface [38], [49], [50].

Nanostructured Cu and Cu derived from engineered surfaces are the focus of much of the recent research into potential Cu catalysts for CO2RR. In general, engineered surfaces such as oxide derived Cu and nanostructures can limit competitive HER, while enhancing geometric current densities for desirable products. These types of surfaces include nanostructured Cu derived from reduction of copper, nanoparticles, arrays of nanowires, nanotubes and accumulated nests of nanowires with porosity due to the loose packing [4] –[13], [51]–[53] . While the results of the multitude of studies on nanostructures have yet to definitively reveal clear systematic rules that might be used to design and tailor CO2RR properties of a highly selective, efficient and durable catalyst, some trends are evident. These trends are that the catalytic properties are influenced by: surface structure; roughness (which can create beneficial local pH effects at the surface); grain boundaries and nanostructure size and shape effects (which can create highly active catalyst sites due to dangling Cu surface bonds); porosity (which can lead to mass transport effects that enhance selectivity and activity towards desirable products); surface strain; and alloying with minor quantities of other elements [4]–[7].

With these considerations in mind, nanoporous Cu (NP-Cu) is an obvious candidate to assess as a potential CO2RR catalyst. The material has large surface area, roughness and porosity. Nanoporous Cu inherently forms unique surfaces with zero and negative curvature typically not present in other Cu nanostructures, and the surface structure can be tuned simply through changing the dealloying method [54]. As we demonstrate in this study, large surface areas of supported films of NP-Cu are simple to make with inexpensive raw materials at low temperatures, suggesting that the material might be more economically viable to manufacture than other forms of nanostructured Cu manufactured by more complex processes. Past research in our lab has demonstrated that the inherent porosity allows NP metals to suppress HER during oxygen reduction and also effectively support ionic liquids in flowing electrolyte which enhanced the efficiency of the oxygen reduction reaction (ORR) on NP-Pt [55], [56]. Similar studies with electrolytes containing ionic liquids have demonstrated that their presence improves selectivity for desired products on metallic electrodes in CO2RR experiments [14]–[19], [57]. NP-Au and NP-Ag formed by selective dealloying have been evaluated as a catalyst for CO2RR, and both have been shown to have excellent selectivity and efficiency for CO production compared to planar films [21]–[23].

Nanoporous copper (NP-Cu) formed by dissolution of a less noble element was noted in detail in 1970 through dealloying of Zn rich brass (Cu/Zn) [58]. More recently, NP-Cu has been fabricated by dealloying of alloys, intermetallics and rapidly solidified ribbons that contained Zn, Al, Mn, Mg, Hf, Y and Ti as the dealloying elements [54], [59]–[69]. In the majority of these studies, NP-Cu was fabricated from homogeneous parent phases, meaning that the entire sample of the parent phase could be dealloyed to form NP-Cu. These homogeneous parent materials are generally made by melting Cu with the alloying elements. Subsequent solidification, heat treatment and dealloying yields NP-Cu, which exhibits the characteristic structure observed in other NP metals such as Au and Pt.

The melting and dealloying process is convenient for fabrication of a dealloyable parent phase. However, the homogeneous parent phases made by these methods tend to yield NP materials with some characteristics that limit their study in certain applications. For electrocatalytic applications, one major limitation is the range of secondary elements that are used (and theoretically possible to use) as the sacrificial dissolving element in the parent phase with Cu as the noble element. Copper has a standard reduction potential of 340 mV, and the secondary elements mentioned earlier have reduction potentials which are significantly negative making them prone to dissolution in almost all conditions encountered during electrocatalytic use in aqueous environments outside of strongly reducing potentials that are undesirable for efficient catalysis. For this reason, a fully dealloyed piece of NP-Cu is most useful as a catalyst in the potential range of typical electrocatalytic applications such as low overpotential CO_2 reduction. Complete dealloying of a bulk piece of parent material can require a matter of days and yield a NP metal where the vast majority of the surface area will be inactive as a catalyst. Without a fully dealloyed catalyst, the secondary element will continue to dissolve, contaminating the electrolyte and superimposing detrimental anodic current over the reductive current we desire to accurately measure. In contrast, widely studied precious NP metals, such as Au, can be formed by dealloying more noble secondary elements, such as Ag, that are stable under electrolytic conditions, so the methods used to produce highly active NP and stable catalyst layers supported on the parent alloy aren't applicable to NP-Cu.

As a non-trivial practical matter, bulk pieces of NP metals tend to be delicate as they are extremely brittle (even for ductile bulk metals such as Au, Pt and Cu) making them difficult to handle and susceptible to mechanical failure unless supported on a mechanically stable substrate. Very thin films of NP-Cu, such as those made from melt-spun ribbons of the parent alloy can exhibit ductility [59]. Based these two limitations, we developed techniques to inexpensively and rapidly synthesize thin films of NP-Cu supported on a bulk substrate for CO2RR evaluation. We show that thin films of NP-Cu fully dealloyed in several hours to prevent secondary dealloying during electrocatalytic experimentation while maintaining sufficient mechanical robustness to be conveniently handled and used as an electrode.

Experimental Methods

Thin films of NP-Cu were fabricated on bulk Cu foil and Cu mesh substrates. The parent phases were synthesized on the Cu substrates through solid state diffusion bonding with 80-120 µm thick foils of Zn and Al to form a series of intermetallics between the pure Cu and Zn or Al phases as shown schematically in Figure 2-2 with the associated phase diagrams Figure 2-3.

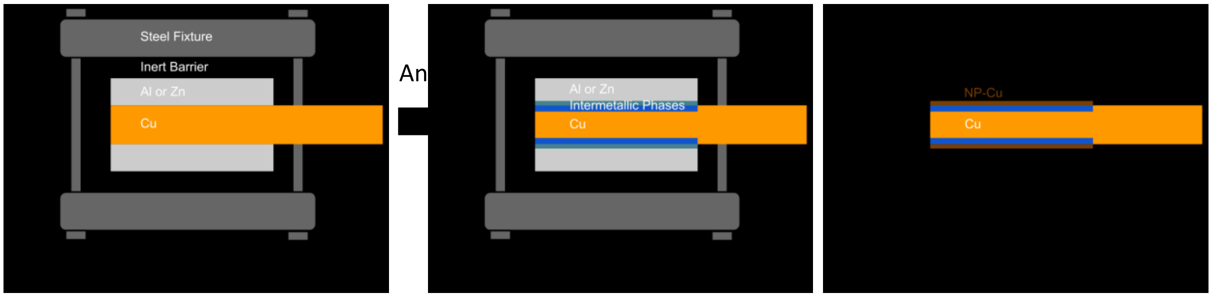

Figure 2-2. Schematic of process used to create supported NP-Cu thin films by diffusion bonding of elemental foils followed by dealloying.

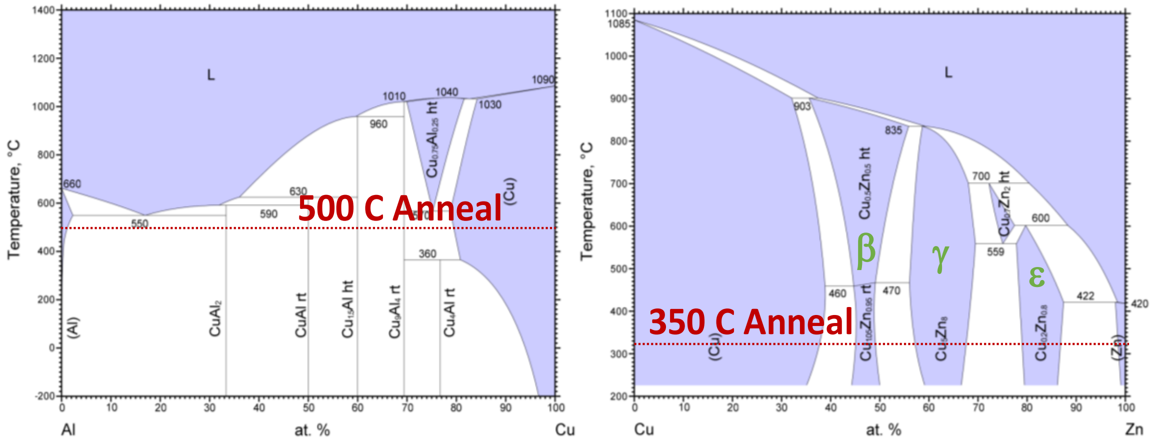

Figure 2-3. Phase diagrams of Cu-Al and Cu-Zn. The red lines denote the annealing temperatures used for diffusion bonding and formation of dealloyable intermetallic phases. The common shorthand symbols for the brass phases are denoted in green.

All foils were formed by rolling of 99.9% purity pellets purchased from Kurt Lesker. Cu mesh (100 Mesh, McMaster Carr) was used to make Cu-Zn. Prior to bonding, Zn and Cu foils were immersed in sulfuric or hydrochloric acids to remove outer oxide layers, then rinsed and dried. The foils were held in compression with a steel fixture during annealing under an N_2 or N_2 + 5% H_2 environment. Annealing was performed in a quartz tube in a Lindberg Blue M tube furnace. Cu-Zn phases were made by annealing at 350 C for 12 to 44 minutes, while Cu-Al phases were made by annealing at 500 C for a minimum of one hour. Samples were quenched in room temperature water after annealing to maintain consistency among the samples. According to the phase diagrams shown in Figure 2-3, Cu forms a series of intermetallics with both Zn and Al. According to the composition of these intermetallics, we expect only ε and γ brasses and $CuAl_2$ to be dealloy on a practical timescale. Pure Zn or Al were fully dissolved from the outer surfaces exposing these phases, while the more Cu rich phases were passivated with Cu at the interface with the dealloying electrolyte, leaving a stable supported NP-Cu film.

Dealloying was performed by free corrosion in several electrolytes: 1M or 3M HCl, 3M H_2SO_4 with or without 100 mM KOAc (potassium acetate), 3M H_3PO_3 and 1M KOH, with the open circuit potential sometimes tracked with a Gamry Interface 1000 potentiostat to follow dealloying progress.

Evaluation of NP-Cu as a CO2RR catalyst was performed in a two chambered cell with planar geometry using a Metrohm Autolab potentiostat as described in previous work [51]. The electrolyte was 100 mM $KHCO_3$ purged with CO_2 at 20 sccm. Gaseous products were detected with GCMS (Shimadzu model GCMS-QP2010SE) at 6 minute intervals and liquid phase products measured by liquid NMR (Bruker 400 MHz NMR spectrometer) from electrolyte sampled after 30 minutes of constant electrolysis at each potential.

Hydrophobic, aprotic ionic liquids (IL) 1- Butyl-3-methyl-imidazolium Hexafluorophosphate ([BMIM][PF6]) and Methyltributylammonium Bis(trifluoromethane)sulfonomide ([M3BN][Tf2N]) were fabricated from equimolar aqueous solutions of the appropriate cation salts (1- Butyl-3-methyl-imidazolium chloride 95%, Sigma Aldrich for [BMIM] or Methyltributylammonium chloride 75%

solution, Sigma Aldrich for [M3BN]) with anion salts (Potassium Hexafluorophosphate 99% for [PF6], Acros Organics or Bis(trifluoromethane)sulfonomide Lithium 99.5%, Sigma Aldrich for [Tf2N]) and stirring for 24 hours to form the IL. Excess water was decanted, and the IL further dried by treatment in a vacuum oven at 70 C for a minimum of 24 hours to remove residual moisture. The NP-Cu catalysts were impregnated with IL by dripping excess IL directly on the catalyst surface, and placing the samples under vacuum at 70 C for a minimum of 30 minutes to drive wetting of the catalyst surface. After impregnation with IL's the NP-Cu/IL composites were evaluated as CO_2 reduction catalysts to determine the effects of the IL.

Results and Discussion

NP-Cu Synthesis

Figure 2-4 shows samples created by diffusion bonding before and after dealloying. The samples were synthesized with a geometric surface area of approximately 1 cm^2. Figure 2-5 and Figure 2-6 show sectional images of Cu-Zn and Cu-Al films before and after dealloying. The NP-Cu formed was 6.9 μm thick derived from Cu-Al for diffusion bonding time of 80 minutes and 4.1, 7.9 and 13.7 μm thick derived from Cu-Zn for diffusion bonding times of 12, 20 and 44 minutes respectively. When bonding to the Cu mesh, the intermetallic structure and subsequently derived NP-Cu did not form on the interior of the mesh pores.

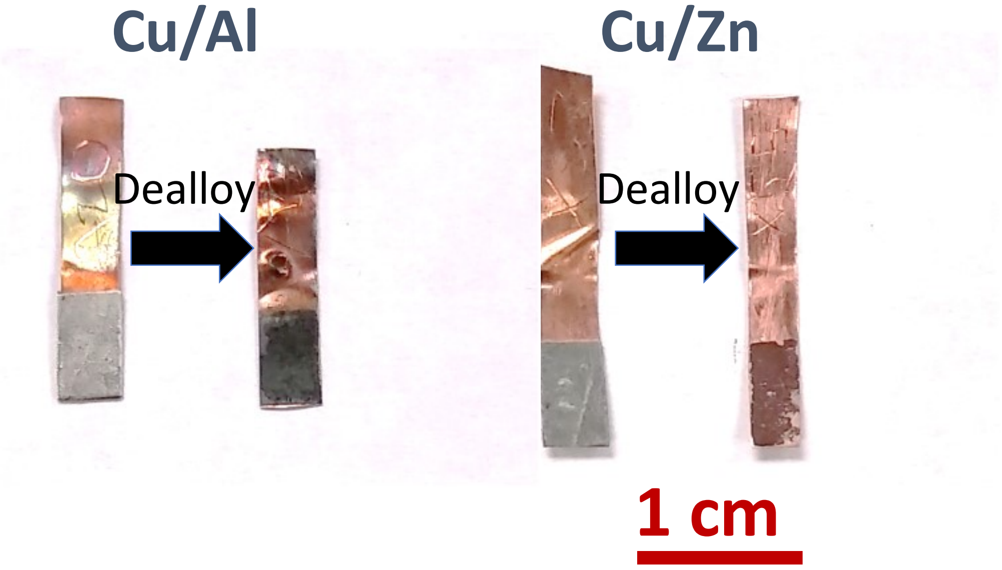

Figure 2-4. Images of NP-Cu films supported on Cu foil synthesized by dealloying of diffusion couples.

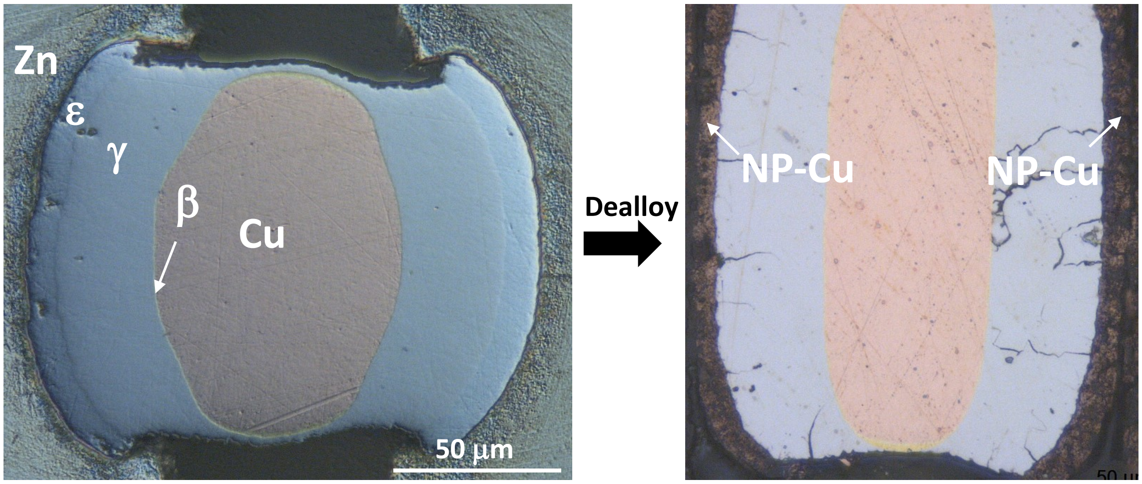

Figure 2-5. Sectional micrographs of Cu mesh and Zn foil after annealing at 350 C for 20 minutes prior to dealloying (left) and after dealloying (right) in 3M H_2SO_4.

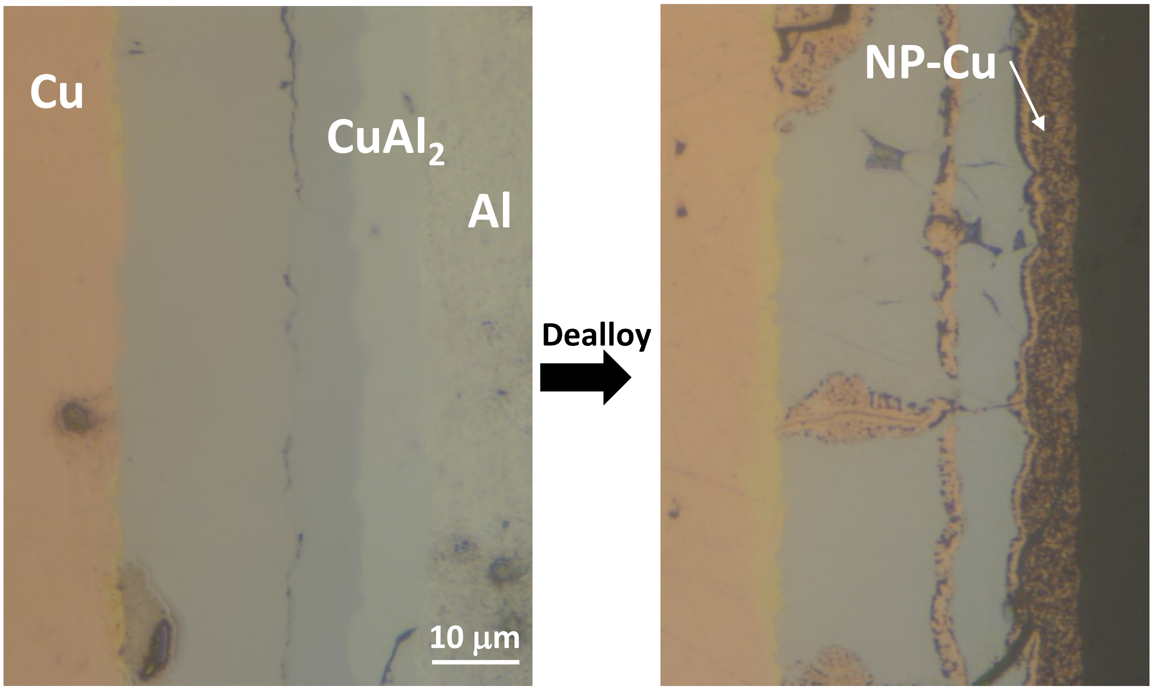

Figure 2-6. Sectional micrographs of Cu and Al foils after annealing at 500 C for 240 minutes prior to dealloying (left) and after dealloying (right) in 1M HCl.

Figure 2-7 shows Cu-Al derived NP-Cu films dealloyed in acidic and basic electrolytes. The dealloying conditions strongly affected the morphology of the NP-Cu, and the NP-Cu formed in basic conditions had finer features (~50 nm in acidic conditions compared to ~20 nm in alkaline) as might be expected since copper oxide, rather than pure copper, was thermodynamically stable in the alkaline conditions (with copper oxide presumably having decreased surface mobility compared to pure copper preventing coarsening through surface diffusion). Figure 2-8 shows NP-Cu supported on a Cu mesh substrate demonstrating that the diffusion bonding and dealloying technique yielded a uniform film across the planar surface of the mesh. Figure 2-9 shows Cu-Zn films dealloyed in various acids, and we again observed that the dealloying conditions strongly affected the morphology of the NP-Cu with the use of HCl notably yielding coarser pores and ligaments than the other acids. The addition of acetate ions to the sulfuric acid based dealloying electrolyte also strongly affected the morphology of the NP-Cu by causing a higher degree of faceting on the ligaments and less uniform feature size distribution due to adsorbed acetate ions affecting dealloying kinetics. Based on the results from CO2RR on NP-Cu derived from-Al couples, we produced the hierarchal NP-Cu on mesh substrates in order to explore the use of this material as an electrocatalyst in flowing electrolyte.

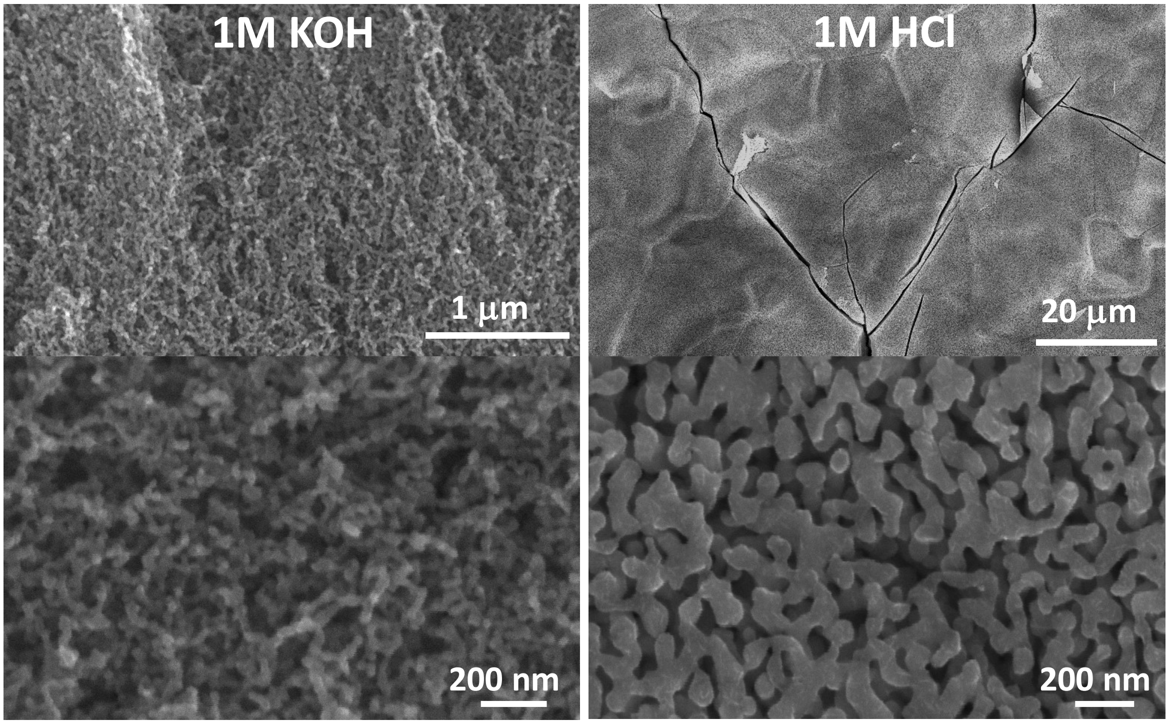

Figure 2-7. Plan view SEM micrographs of NP-Cu synthesized from dealloyed Cu-Al in the noted electrolytes.

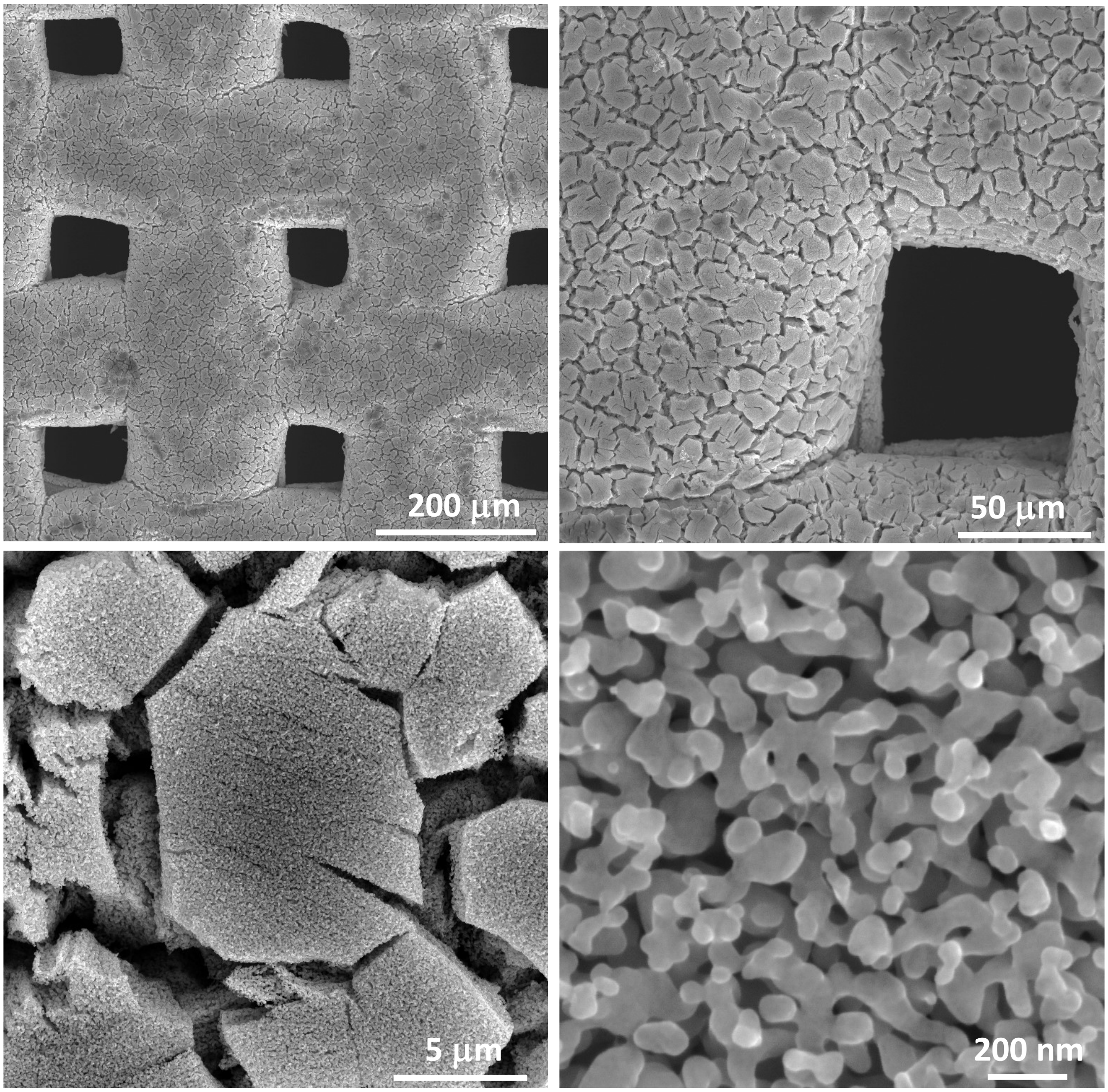

Figure 2-8. Plan view SEM micrographs of NP-Cu synthesized from Cu-Zn parent supported on Cu mesh and dealloyed in 3M H_2SO_4.

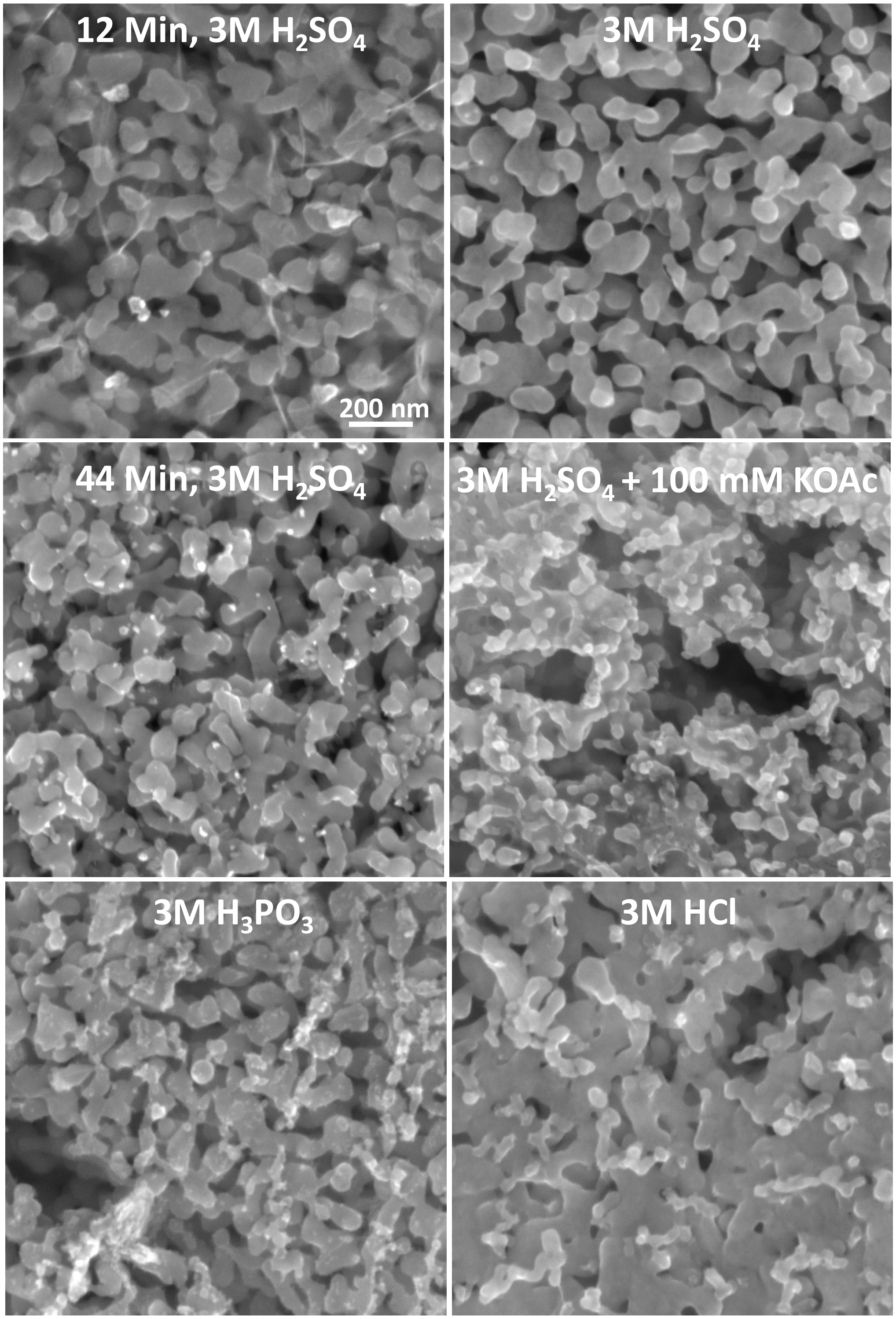

Figure 2-9. Plan view SEM micrographs of NP-Cu synthesized from dealloyed Cu-Zn (annealed for 20 minutes at 350 C unless noted) supported on Cu mesh in the noted electrolytes.

The thin films of intermetallics formed by diffusion bonding dealloyed in the span of hours. Figure 2-10 shows the open circuit potential (OCP) during free corrosion dealloying of Cu-Zn films in 1M H_2SO_4. The OCP stabilized after approximately three hours, and longer immersion demonstrated that the material had reached steady state as the OCP settled at a potential of approximately -600 mV versus an MSE reference (and remained there in excess of 10 hours) which was approximately 150 mV below the measured OCP of pure Cu in the electrolyte. We observed similar trends for dealloying of Cu-Al intermetallics. Compositional measurements by EDS showed the Cu-Al derived NP-Cu retained ~3.5 at% Al and Cu-Zn derived retained ~6.5 at% Zn.

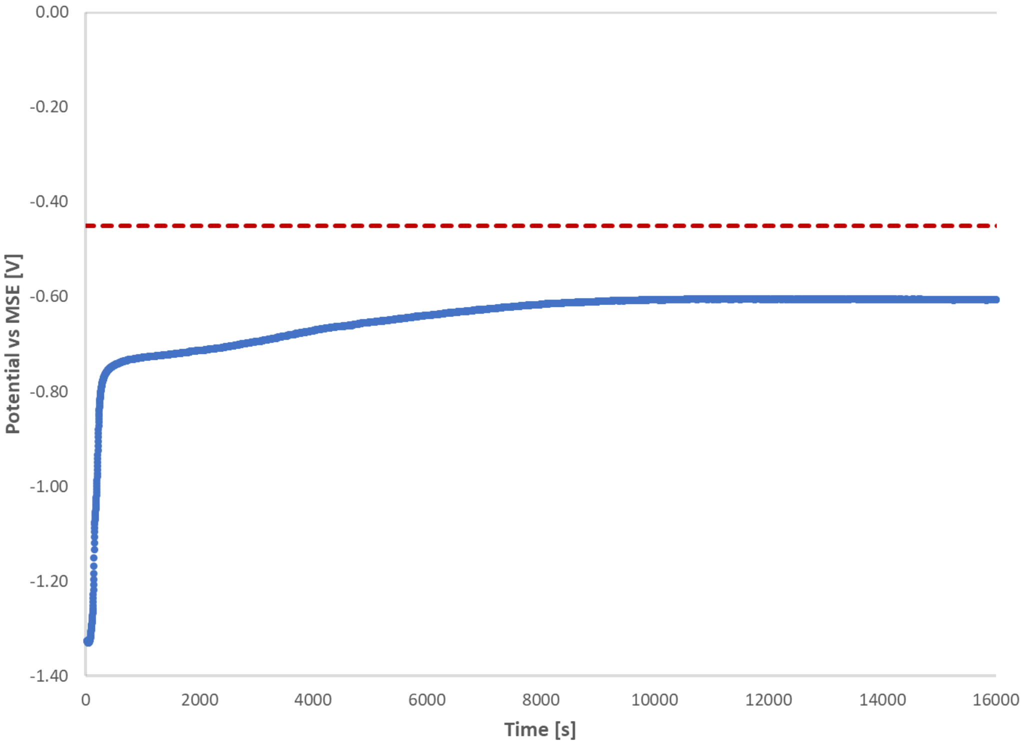

Figure 2-10. Open circuit potential versus time for dealloying in 1M H_2SO_4 of Cu/Zn bonded at 350 C for 18 min. The dashed red line denotes the open circuit potential of pure Cu in the electrolyte.

The roughness factors of Cu/Zn derived NP-Cu supported on Cu mesh were measured by underpotential deposition (UPD) of Zn on the NP-Cu. Figure 2-11 through Figure 2-13 show cyclic voltammograms of various Cu-Zn samples with the Zn UPD prevalent around -1.10 and -1.25 V versus MSE on the deposition sweep and -1.20 and -1.10 V on the stripping peak. We measured the average charge under the Zn UPD stripping peak and divided by that of a bare mesh to calculate a roughness factors of various NP-Cu films as indicated in Table 2-1.

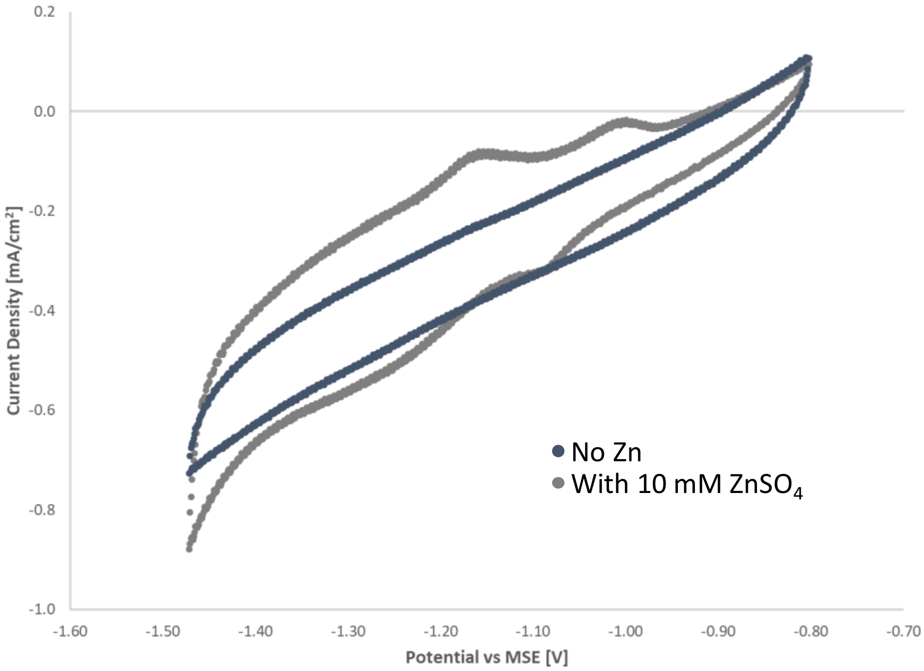

Figure 2-11. Cyclic voltammograms (50 mV/sec) of Cu mesh in 250 mM K_2SO_4 *with and without* $ZnSO_4$ *as indicated.*

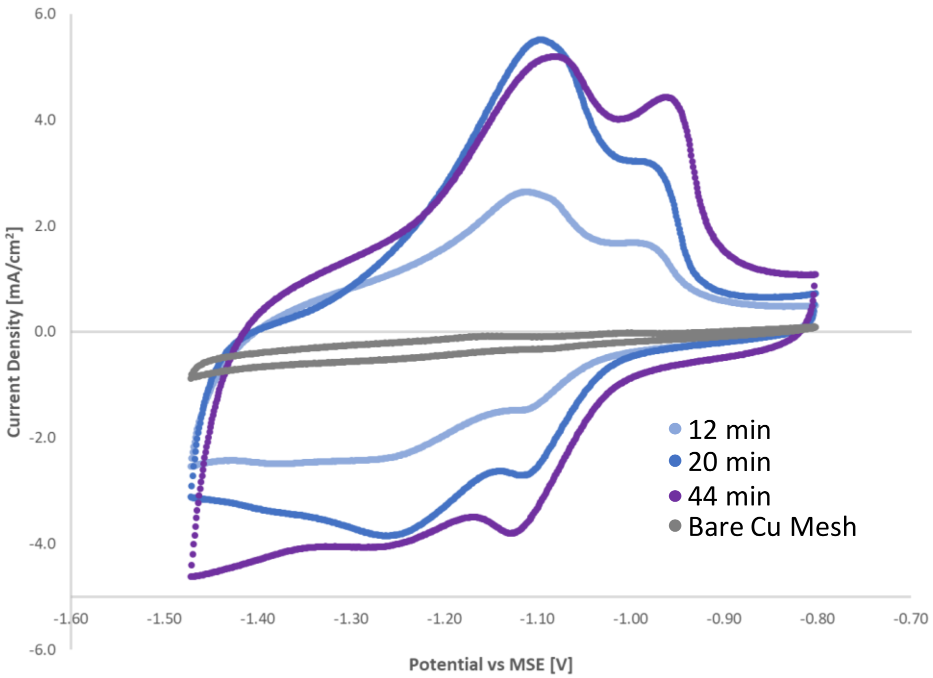

Figure 2-12. Cyclic voltammograms (50 mV/sec) in 250 mM K_2SO_4 + 10 mM $ZnSO_4$ of NP-Cu formed by diffusion bonding Cu-Zn at 350 C for the noted times.

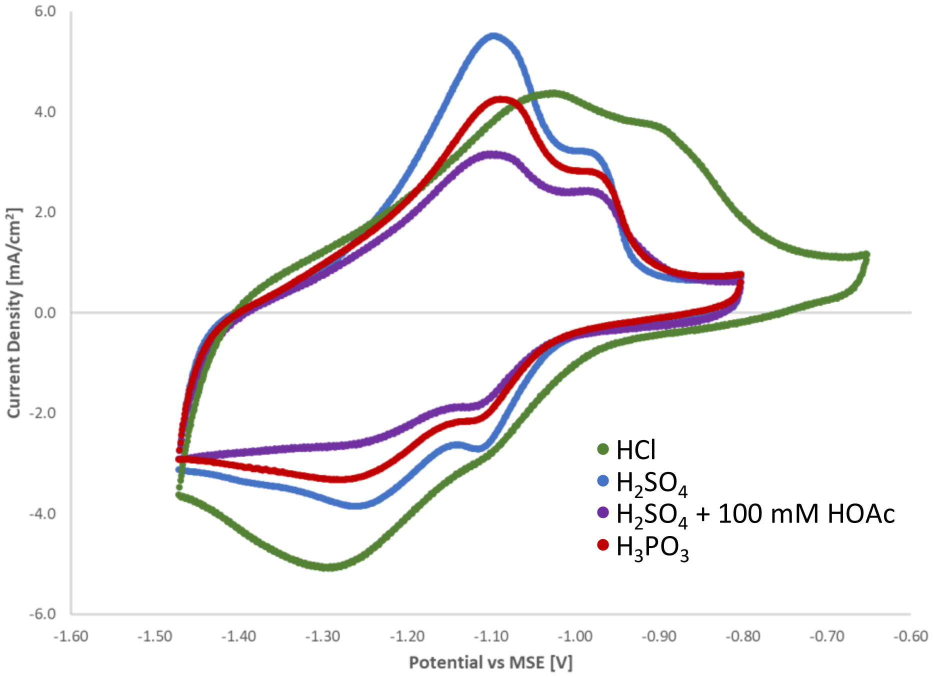

Figure 2-13. Cyclic voltammograms (50 mV/sec) in 250 mM K_2SO_4 + 10 mM $ZnSO_4$ of NP-Cu formed by diffusion bonding Cu-Zn at 350 C for 20 minutes and subsequently dealloyed in the noted electrolytes.

Table 2-1. Measured roughness factors of NP-Cu films by Zn UPD. Cu-Zn samples were bonded at 350 C, and Cu-Al samples were bonded at 500 C.

Sample	**Bonding Time [Min]**	**Dealloying Electrolyte**	**Roughness**
Cu Mesh/Zn	12	3M H_2SO_4	21
Cu Mesh/Zn	20	3M H_2SO_4	44
Cu Mesh/Zn	44	3M H_2SO_4	44
Cu Mesh/Zn	20	3M H_2SO_4 + 100 mM KOAc	28
Cu Mesh/Zn	20	3M H_3PO_3	34
Cu Mesh/Zn	20	3M HCl	47
Cu/Al	60	1M HCl	23
Cu/Al	60	1M KOH	17

The Cu-Al based samples exhibited lower roughness factors than the Cu-Zn due to decreased film thickness despite the NP-Cu feature size being similar for samples dealloyed in acid, and notably finer for Cu-Al samples dealloyed in alkaline conditions. For the Cu-Zn sample bonded for 20 minutes and dealloyed in HCl the Zn UPD stripping peaks broadened and shifted in a positive direction relative to all other samples. The SEM micrographs of this sample also show significantly coarser NP-Cu, which was a result of the large enhancement of surface diffusivity of Cu with adsorbed Cl^-.

Another interesting trend of note from Table 2-1 was the scaling of the roughness factor with the measured thickness of the NP-Cu layer. While the thickness of the NP-Cu initially increased with increasing heat treatment bonding time as expected, the roughness was calculated as nearly constant for samples bonded for 20 minutes or longer. The cause of the apparent plateau in the calculated roughness was attributed to several factors. For samples dealloyed in H_2SO_4, the roughness factor as measured by Zn UPD remained constant for the samples annealed for 20 and 44 minutes despite the thickness of the NP-Cu layer being 73% thicker for the 44 minute anneal sample. As the phase diagram indicates (Figure 2-3), the ε phase has a range of compositions from approximately $Cu_{20}Zn_{80}$ to $Cu_{12}Zn_{88}$. The technique used for production of the Cu-Zn couples would lead to a compositional gradient in the ε brass phase, and this compositional gradient likely resulted in a variation in the morphology of the NP-Cu throughout the thickness of the NP-Cu layer. The effects of parent phase composition on the morphology of dealloyed have been studied for NP-Au derived from Au-Ag solid solutions [70]. In this study, NP-Au produced by dealloying Ag80Au20 was notably finer than NP-Au produced from Ag91Au9. The sectional images of the Cu-Zn couples showed a complex structure with widely varying thickness of the various brass phases that indicated large relative variations in diffusional fluxes of Cu and Zn across the interfaces between the phases. While EDS measurements on Cu-Zn compositions in individual brass phases weren’t sensitive enough to accurately measure small differences in composition, the roughness and coarseness of the NP-Cu derived from ε brass films of differing thickness both suggested that longer bonding times resulted in dealloyable ε brass films with lesser average amounts of Cu resulting in measured roughness factors that didn’t scale linearly with NP-Cu layer thickness.

However, such an effect likely didn’t cause such a drastic change in the calculated roughness factor as evidenced by the relative consistency in the NP-Cu morphologies between the samples bonded for 20 and 44 minutes evident in the SEM micrographs. The UPD of Zn on Cu hasn’t been well characterized as other well established UPD systems, and the results here indicated that the calculated roughness factors by Zn UPD were affected by subtle changes in the NP-Cu structure or underlying ligament composition. The shift and broadening of the UPD peaks in the Cu-Zn sample dealloyed in HCl (which underwent significant potential shifts relative to other samples) and the discrepancy in the roughness factors of the Cu-Al samples (the finer NP-Cu from dealloying in alkaline conditions had a lesser apparent roughness factor than the coarser NP-Cu from acidic dealloying) provided strong evidence that the Zn UPD peaks were very sensitive to changes in NP-Cu structure and composition. Since the compositional measurements showed that there was significant residual Zn in the ligaments, there is a strong possibility that error was introduced by the Zn UPD technique and was reflected in the roughness calculations. Even accounting for this apparent error, the synthesized NP-Cu exhibited significant enhancements in surface area relative to the unaltered substrates.

We also noted from cross-sectional images that the γ brass phase did not dealloy as has been previously demonstrated [54]. The cause for the lack of dealloying of this phase and the settling of the OCP below that of pure Cu in our samples was cathodic protection caused by the layered structures created from both Cu-Al and Cu-Zn parent phases. As the outer layers dealloyed, the OCP subsequently increased as expected. The steady state OCP that was reached then represented the value at which the layer beneath the NP-Cu was passivated. This intermetallic layer supporting the NP-Cu had less Zn or Al than the dealloyable layer and thus a greater reduction potential, but even if the supporting intermetallic could be dealloyed in homogeneous form, a significant overpotential above the critical potential would have been required to prevent passivation as is inherent to dealloying in general [71]. At such a point in the dealloying process, the NP-Cu layer and the supporting intermetallic would have the same electric potential (excluding contact potential negligible for this discussion) which would have prevented further dealloying as each phase would be providing a means of cathodic protection to the other phase. This effect would also explain the amounts of residual Zn and Al we detected in the NP-Cu that isn’t common in other studies of NP-Cu.

The thin films of NP-Cu supported directly on Cu substrates fabricated in this study were well suited for electrocatalytic applications (as will be discussed in detail for CO2RR in a later chapter). The measured roughness factors showed that the NP-Cu contained large surface area, and synthesis of the NP-Cu was straightforward and should be directly scalable to considerably larger geometric surface areas (we were limited only by furnace size).

The variation in the structure of the NP-Cu based on dealloying conditions provided a simple way to altering the surface structure, and the presence of adsorbing molecules during dealloying further altered the morphology of the NP-Cu. We also explored addition of polyvinylpyrrolidone (a strong capping agent employed in solution-based synthesis techniques) to 3M HCl during Cu-Zn dealloying, and found that the NP-Cu didn't fully dealloying due to the presumed adsorption of the organic molecule on the dealloying surfaces. As is demonstrated in CO2RR experiments, the catalytic properties were sensitive to the dealloying medium, which predictably indicated the catalytic properties were sensitive to the surface structure and composition of the NP-Cu. In the case of NP-Cu, some of the secondary elements used for dissolution are prone to dissolution in a wide range of electrolytes and dealloying conditions, especially compared to those secondary elements used to make precious NP-metals. While our NP-Cu retained some of the less noble elements, the samples did not continue to dealloy during CO2RR experiments as all tested potentials were negative of the OCP of the NP-Cu.

The settling of the OCP below that of pure Cu and compositional measurements showed that the NP-Cu formed a structure with Cu passivating the surfaces of ligaments containing residual amounts of the secondary element. While not explored in detail in this work, techniques already developed for coarsening and further dealloying would allow for further removal of the secondary element and possible tuning of the electronic properties of the NP-Cu which could affect catalytic properties an provide another method for tuning the catalytic properties.

The thin films of NP-Cu synthesized during this work have several advantages for electrocatalytic applications compared to monolithic samples of bulk Cu produced in much of the previous research into synthesis of NP-Cu, suggesting that these supported thin films might be less expensive and faster to produce than bulk NP-Cu without sacrificing active surface area. We demonstrated that the film can be manufactured and dealloyed to a stable condition in several hours at processing temperatures well below those required to form parent phases through melting of Cu (1085 C melting point). Previous studies of bulk NP-Cu employ dealloying treatments exceeding a day, suggesting that a supported thin film might be more economically viable for practical applications [54], [68]. The electrochemically active surface area of nanoporous catalysts has been demonstrated to be a function of applied overpotential and nanoporous film thickness, and previous results for ORR on NP-Pt suggests that micron-thick films of NP-Cu should be significantly thick enough to reduce all reactants entering the pores with no loss of ECSA compared to bulk NP-Cu [72].

Qualitatively, NP-Cu supported on the Cu foils are mechanically robust. The samples could be handled without apparent damage to the NP-Cu. The samples were also mechanically stable under subsequent CO2RR electrocatalytic testing in vigorous bubbling. Since fully dealloyed pieces of unsupported NP-Cu are brittle and prone to cracking, the techniques for producing the supported NP-Cu on a ready-made electrode represent a significant improvement in the ease of use for electrochemical applications.

In some recent research on synthesis of NP-Cu, other methods have been devised to form mechanically robust thin foils of NP-Cu as well as an electrodeposition technique to form films of Cu-Zn which dealloy to NP-Cu on an electrode. The methods to form thin foils (tens of micron scale thickness) rely on the use of melt spun ribbons of Cu with Al and Hf in the parent materials [59]. When dealloyed, these ribbons can form NP-Cu that is flexible rather than brittle. Melt spinning techniques require expensive capital equipment and are limited to formation of strands of narrow ribbons.

At least one group has demonstrated co-electrodeposition of Cu and Zn to form a thin film that can be dealloyed to form thin films of NP-Cu [61]. Other groups have demonstrated synthesis of NP-Cu by electrodeposition of thin films of Zn (~2 μm) on

Cu followed by annealing (at 150 to 250 C for 1 to several hours) and dealloying [73]–[76]. (Some of these examples do not appear to have characteristic NP-Cu structure or ligament size as observed in typical samples dealloyed at room temperature, an effect we also found in similar testing summarized below.)

We also investigated several similar methods of co-electrodeposition of Cu-Zn and Cu-Mn or Zn electrodeposition followed by annealing and did produce some NP-Cu films but also found it challenging to form a highly uniform, homogeneous parent film by these methods, whereas diffusion bonding of Cu and the foils of the secondary element produced reliable, repeatable, uniform films of NP-Cu after dealloying. It should also be noted that co-electrodeposition of the parent alloy in our preliminary testing was prone to formation of poor-quality films when using Zn or Mn as the alloying element with Cu in the electrolyte due to the low reduction potentials of the secondary elements, meaning that deposition potentials were in the range where H_2 evolution dominated the electrode reaction.

We found that electrodeposition of pure Zn followed by annealing had a primary drawback to the diffusion bonding technique: the high quality, uniform film of Zn that could be deposited in reasonable time frames was much thinner than the foils used for diffusion bonding, limiting the thickness of the NP-Cu film we could form and necessitating strict annealing environments (the samples were susceptible to detrimental oxidation penetrating to the Zn/Cu interface even in inert annealing atmospheres). This difference in Zn film thickness also meant that annealing on the thinner Zn films had to be performed at significantly lower temperatures and often resulted in non-uniformity of the sample following dealloying in our experiments.

CO2RR on NP-Cu

Figure 2-14 shows faradaic efficiency of CO2RR on NP-Cu films derived from Cu-Al parent phases including samples impregnated with two aprotic, hydrophobic IL's and evaluated as CO2RR catalysts under the same conditions. Figure 2-15 shows partial current densities for NP-Cu derived from Cu-Al and dealloyed under alkaline conditions. Similar curves were obtained for all other NP-Cu samples evaluated, with H_2 being the dominant product and comprising the majority of the current density.

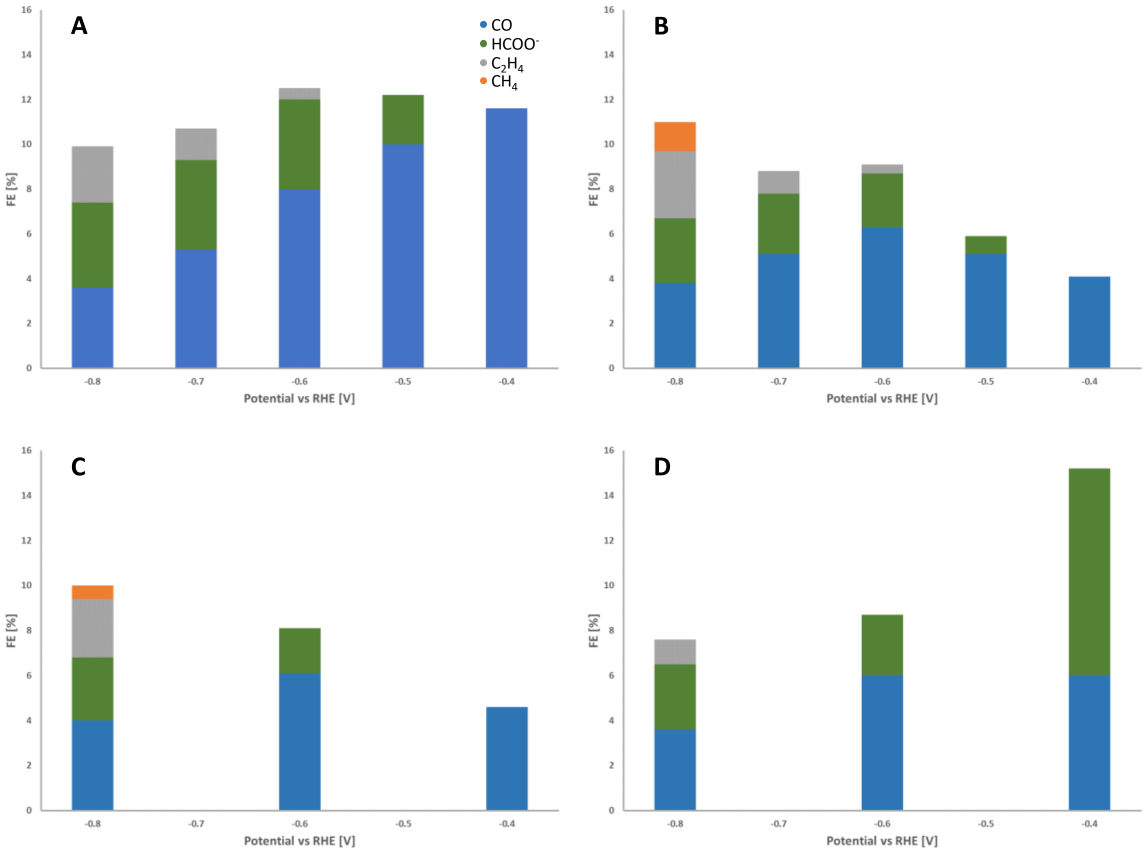

Figure 2-14. Faradaic efficiencies of CO2RR with NP-Cu thin films derived from Cu-Al: A) dealloyed in 1M KOH, B) dealloyed in 1M HCl, C) dealloyed in 1M HCl and impregnated with [M3BN][Tf2N], and D) dealloyed in 1M HCl and impregnated with [BMIM][PF6]. The balance of the FE leading to 100% total efficiency was H_2.

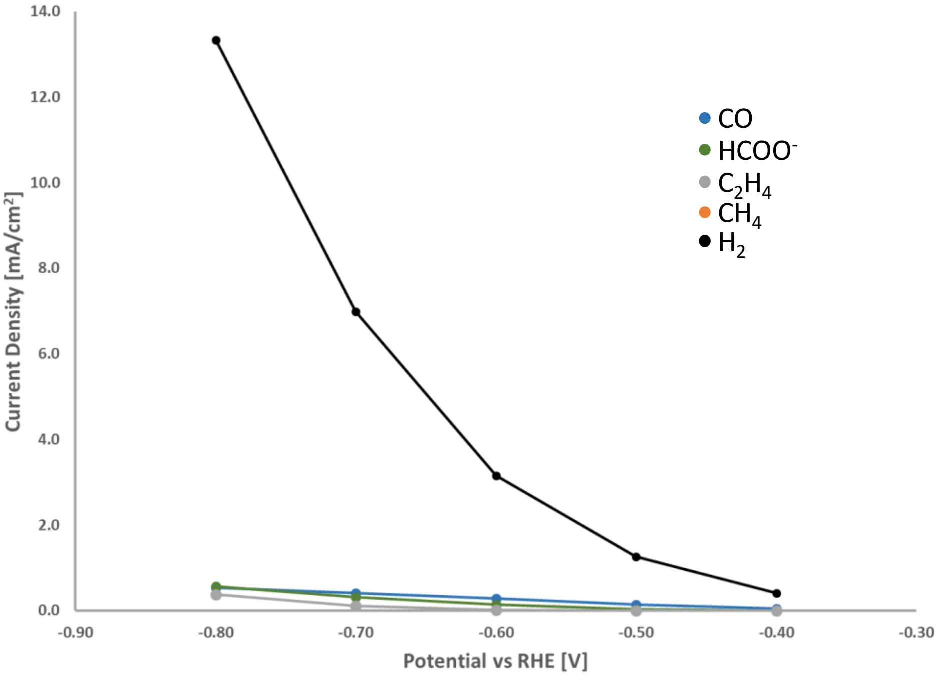

Figure 2-15. Partial current densities for CO2RR products on NP-Cu catalyst derived from Cu-Al and dealloyed in 1M KOH.

As the above data indicate, all of the NP-Cu catalysts primarily produced H_2 during CO2RR experiments with the Faradaic efficiency for H_2 exceeding 80% under all conditions evaluated. Our results were qualitatively different than one recent study using similarly produced Cu film from dissolution of Zn from a Cu-Zn parent phase, where a NP-Cu film notably increased CO selectivity at low overpotentials relative to other films roughened by Zn dissolution [75]. (The other films investigated in the study were not NP-Cu according to SEM micrographs). In that study, no residual Zn was detected (in contrast to our NP-Cu films) in the one sample that exhibited a porous structure characteristic of NP metals. With respect to Hydrogen evolution, the distribution of products from the NP-Cu in this work more closely matched those for electropolished polycrystalline Cu foil and planar electrodeposited Cu films tested under similar conditions than nanostructured forms of Cu [12], [24]. Planar Cu catalysts evaluated in these previous studies exhibited greater selectivity for CO_2 reduction to CO and formate species (up to approximately 70% Faradaic efficiency) at -800 mV versus RHE than we observed. We attribute the cause of this poor CO_2 reduction efficiency to the residual subsurface Al remaining in the NP-Cu catalyst. Previous studies on CO2RR with pure Al catalysts under strongly reducing conditions in bicarbonate electrolytes have shown that Al catalysts are selective at near unit efficiency for H_2 production [25], [50]. With several atomic percent of Al remaining in the synthesized NP-Cu, the residual Al certainly affected interaction of the Cu rich surface with adjacent electrolyte, and the results suggested that the Al imparted a more Al like character on NP-Cu. Altering the character of the NP-Cu catalyst surface relative to pure Cu would also have strong effects on the selectivity of CO2RR which is extremely sensitive to binding energies of CO_2 intermediates, protons and water. Hori compiled numerous examples of Cu based alloys (not including Cu-Al alloys of which we found no previous studies for CO2RR) exhibiting varied CO2RR characteristics relative to pure Cu showing the minor alloying affected CO2RR characteristics of Cu [50].

Despite the poor CO_2 reduction selectivity of the NP-Cu derived from Cu-Al, we observed clear differences in selectivity for products based on the dealloying electrolyte and use of IL's with the NP-Cu. We opted to first evaluate NP-Cu derived from Cu-Al as dealloying in acidic and alkaline conditions produced vastly different morphologies of NP-Cu. The CO2RR results (Figure 2-14 A and B) show that the resulting NP-Cu clearly influenced the selectivity for CO2RR. The alkaline derived NP-Cu produced significantly more CO (especially at the lowest overpotentials probed) and no CH_4, while the acidic derived NP-Cu produced a minor amount of CH_4 at the largest overpotential. Formate production began at the same overpotential in each sample and showed a similar trend of remaining nearly constant over the remainder of the larger overpotentials, with the alkaline derived sample producing formate at approximately twice greater efficiency. The onset of ethylene production occurred at the same potential in each NP-Cu sample and showed similar trends with the FE increasing with increasing overpotential.

While the FE trends show that the alkaline derived NP-Cu had increased selectivity for CO2RR rather than HER, the HCl derived NP-Cu showed a smaller fraction of its carbon containing products were formate. This finding suggests that the HCl derived NP-Cu was better optimized towards formation of higher value products. Carbon monoxide has been demonstrated as an intermediate for production of C_2H_4 and CH_4 as well as other multi-carbon products while formate does not further reduce to desirable fuel products [26]. The formation of formate proceeds through reaction pathways involving initial adsorption of O (in a CO_2 molecule) or an H atom in contrast to those leading to the CO intermediate which involve adsorption of C (in a CO_2 molecule).

Impregnating the HCl derived NP-Cu with IL's had varying effects depending on the IL employed. Both IL's were aprotic and hydrophobic, although only [BMIM][PF6} meaningfully affected the catalytic properties. Previous ORR experiments with [M3BN][Tf2N] impregnated NP-Pt in our lab have suggested that this IL did not remain on the surface of the catalyst in flowing electrolyte. Due to the similarities in the FE between the NP-Cu with and without [M3B][Tf2N], the same issue was suspected as occurring in our CO2RR experiments, where this IL didn't remain on the NP-Cu and we therefore observed CO2RR over a bare NP-Cu surface. While HER was the dominant product for all samples evaluated, the NP-Cu impregnated with [BMIM][PF6] exhibited strong variation in the FE in carbon containing products compared to the bare NP-Cu. At low overpotentials we observed a substantial increase in the amount of formate produced. At larger overpotentials, the formate production was similar to the non-impregnated NP-Cu, and FE for CO was similar over the entire potential range. Ethylene was only observed at the largest overpotential and at lower FE than bare NP-Cu, and we did not detect any methane at the largest overpotentials for the IL containing NP-Cu. While the results did show that the IL could have a strong effect on the selectivity of the CO2RR while suppressing HER at low overpotentials and lowering the overpotential required for at least one of the carbon-containing products, the IL used in this case promoted formate production suggesting that the [BMIM][PF6] wasn't an ideal IL for enhancing CO2RR along CO reaction paths towards higher order products. The results here at the lowest overpotential measured were qualitatively similar to CO2RR results with dendritic Cu catalysts in an aqueous electrolyte containing an imidazolium based IL (such as [BMIM]), where production of formic acid was promoted in the IL containing electrolyte at decreased onset overpotentials compared to similar catalyst in aqueous environment [26], [77].

Copper mesh was used as the substrate for Cu-Zn diffusion couples based on the CO2RR results from the NP-Cu derived from Cu-Al. Our aim in using a mesh substrate was demonstrating the flexibility of the diffusion bonding technique to produce NP-Cu with porosity of multiple length scales while also making a sample with a supported NP-Cu film that electrolyte could flow through when the sample was used in electrolytic flow cell. Employing NP-Cu as a flow-through electrode could offer experimental controls not available in a more conventional setup of a supported porous sample. The concentrations of the various reactants and products could vary significantly as the electrolyte passed through the NP-Cu, possibly biasing the various reaction paths and altering the selectivity of the NP-Cu. Roughness has been shown as beneficial to the selectivity of CO2RR in several studies with the selectivity changes due to roughness being modeled as a result of local pH effects at the electrode (rougher films enhance localized pH increase at the catalyst surface due to reduction reactions at the electrode surface) [11], [26], [28], [51]. Flowing electrolyte entirely through the NP-Cu electrode might amplify such effects relative to a roughness supported on a planar substrate where only the outermost layer of the film is active in the case of NP-Cu. Flowing through the porous copper might also more efficiently use the available surface area and increase the reductive current density achievable at given potentials. For reasons discussed in detail in the following chapters, the NP-Cu thin films supported on Cu mesh weren't quite ideal for a flow cell use. Notably, the absence of NP-Cu thin films on the interior pore surfaces of the mesh was not ideal as this is the most active area of the electrode in a flow cell setup. These issues would be most easily remedied with a Cu substrate with smaller pores (such a mesh size which we found is not commonly sold), and a diffusion bonding fixture capable of compressing the Zn film such that it deforms into the pore structure. A fixed volume fixture to prevent later plastic deformation of the substrate and Zn foils (the sides of the one used here were open) may suffice.

Conclusion

Rapid synthesis of thin films of high-quality NP-Cu supported on Cu foil or mesh was demonstrated through solid state diffusion bonding of foils of the secondary sacrificial element (Al or Zn) to a Cu foil. The diffusion bonding process yielded layers of intermetallics at the interface of the Cu and secondary element where the outermost layer was a dealloyable intermetallic layer up to 10 microns in thickness. Subsequent dealloying by free corrosion yielded pristine layers of NP-Cu with small amounts of residual Zn or Al, and the choice of dealloying medium had a significant impact on the structure of the NP-Cu. Bonding time also impacted the measured roughness of NP-Cu derived from Cu-Zn alloys and was attributed to variation in the composition inherent to the ε brass phase that was dealloyed to form the NP-Cu as well as compositional and structural effects on the Zn UPD technique used to measure roughness. In all dealloying conditions, pore and ligament sizes were on the magnitude of tens of nm giving the NP-Cu roughness factors ranging from approximately 10 to 50. The NP-Cu was dealloyed to a stable state for CO2RR within several hours. The technique developed here has several advantages compared to other methods for producing NP-Cu, including shorter processing times and lower temperatures for synthesis of the parent material, ease of producing stably dealloyed NP-Cu (with potential geometric surface area limited only by furnace size), mechanical robustness due to the underlying substrate, a convenient form for use as an electrocatalyst, and lower capital cost compared to rapid solidification techniques.

The NP-Cu films produced from Cu-Al were evaluated as CO2RR catalysts, and the NP-Cu showed enhanced selectivity for HER compared to pure Cu in many other forms. Residual, subsurface Al in the NP-Cu was attributed as the cause of enhanced HER selectivity relative to pure Cu as Al is a poor CO_2 reduction catalyst. Despite the low efficiency for CO_2 reduction, the dealloying technique did strongly affect the selectivity of the CO_2 reduction reactions with alkaline dealloying conditions yielding enhanced formate selectivity. Impregnating the NP-Cu with an imidazolium based ionic liquid prior to CO_2 reduction dramatically altered the CO_2 reduction selectivity at low overpotentials leading to enhanced formate production.

References

[1] IPCC, “GLOBAL WARMING OF 1.5°C,” 2018.

[2] G. P. Peters *et al.*, “Towards real-time verification of CO2 emissions,” *Nat. Clim. Chang.*, vol. 7, no. 12, pp. 848–850, Dec. 2017.

[3] B. Kumar *et al.*, “New trends in the development of heterogeneous catalysts for electrochemical CO2 reduction,” *Catal. Today*, vol. 270, pp. 19–30, Jul. 2016.

[4] W. Zhang *et al.*, “Progress and Perspective of Electrocatalytic CO_2 Reduction for Renewable Carbonaceous Fuels and Chemicals,” *Adv. Sci.*, vol. 5, no. 1, p. 1700275, Jan. 2018.

[5] G. Zhao, X. Huang, X. Wang, and X. Wang, “Progress in catalyst exploration for heterogeneous CO_2 reduction and utilization: a critical review,” *J. Mater. Chem. A*, vol. 5, no. 41, pp. 21625–21649, Oct. 2017.

[6] R. J. Lim *et al.*, “A review on the electrochemical reduction of CO2 in fuel cells, metal electrodes and molecular catalysts,” *Catal. Today*, vol. 233, pp. 169–180, Sep. 2014.

[7] J. Qiao, Y. Liu, F. Hong, and J. Zhang, “A review of catalysts for the electroreduction of carbon dioxide to produce low-carbon fuels,” *Chem. Soc. Rev.*, vol. 43, no. 2, pp. 631–675, Dec. 2014.

[8] J. W. Vickers, D. Alfonso, and D. R. Kauffman, “Electrochemical Carbon Dioxide Reduction at Nanostructured Gold, Copper, and Alloy Materials,” *Energy Technol.*, vol. 5, no. 6, pp. 775–795, Jun. 2017.

[9] H. Mistry *et al.*, “Highly selective plasma-activated copper catalysts for carbon dioxide reduction to ethylene,” *Nat. Commun.*, vol. 7, p. 12123, Jun. 2016.

[10] R. G. Mariano, K. McKelvey, H. S. White, and M. W. Kanan, “Selective increase in CO2electroreduction activity at grain-boundary surface terminations.,” *Science*, vol. 358, no. 6367, pp. 1187–1192, Dec. 2017.

[11] C. W. Li and M. W. Kanan, “CO $_2$ Reduction at Low Overpotential on Cu Electrodes Resulting from the Reduction of Thick Cu $_2$ O Films,” *J. Am. Chem. Soc.*, vol. 134, no. 17, pp. 7231–7234, May 2012.

[12] T. T. H. Hoang, S. Ma, J. I. Gold, P. J. A. Kenis, and A. A. Gewirth, “Nanoporous Copper Films by Additive-Controlled Electrodeposition: CO $_2$ Reduction Catalysis,” *ACS Catal.*, vol. 7, no. 5, pp. 3313–3321, May 2017.

[13] K. P. Kuhl, T. Hatsukade, E. R. Cave, D. N. Abram, J. Kibsgaard, and T. F. Jaramillo, “Electrocatalytic Conversion of Carbon Dioxide to Methane and Methanol on Transition Metal Surfaces,” *J. Am. Chem. Soc.*, vol. 136, no. 40, pp. 14107–14113, Oct. 2014.

[14] D. Vasilyev, E. Shirzadi, A. V. Rudnev, P. Broekmann, and P. J. Dyson,

"Pyrazolium Ionic Liquid Co-catalysts for the Electroreduction of CO $_2$," *ACS Appl. Energy Mater.*, p. acsaem.8b01086, Sep. 2018.

[15] Y. Oh and X. Hu, "Ionic liquids enhance the electrochemical CO $_2$ reduction catalyzed by MoO $_2$," *Chem. Commun.*, vol. 51, no. 71, pp. 13698–13701, Aug. 2015.

[16] X. Zhang *et al.*, "Electrochemical Reduction of Carbon Dioxide to Formic Acid in Ionic Liquid [Emim][N(CN)2]/Water System," *Electrochim. Acta*, vol. 247, pp. 281–287, Sep. 2017.

[17] G. Iijima *et al.*, "CO $_2$ Reduction Promoted by Imidazole Supported on a Phosphonium-Type Ionic-Liquid-Modified Au Electrode at a Low Overpotential," *ACS Catal.*, vol. 8, no. 3, pp. 1990–2000, Mar. 2018.

[18] E. E. L. Tanner, C. Batchelor-McAuley, and R. G. Compton, "Carbon Dioxide Reduction in Room-Temperature Ionic Liquids: The Effect of the Choice of Electrode Material, Cation, and Anion," *J. Phys. Chem. C*, vol. 120, no. 46, pp. 26442–26447, Nov. 2016.

[19] B. A. Rosen *et al.*, "Ionic liquid-mediated selective conversion of CO_2 to CO at low overpotentials.," *Science*, vol. 334, no. 6056, pp. 643–4, Nov. 2011.

[20] J. T. Feaster *et al.*, "Understanding Selectivity for the Electrochemical Reduction of Carbon Dioxide to Formic Acid and Carbon Monoxide on Metal Electrodes," *ACS Catal.*, vol. 7, no. 7, pp. 4822–4827, Jul. 2017.

[21] Q. Lu *et al.*, “A selective and efficient electrocatalyst for carbon dioxide reduction,” *Nat. Commun.*, vol. 5, no. 1, p. 3242, Dec. 2014.

[22] S. Sen, D. Liu, and G. T. R. Palmore, “Electrochemical Reduction of CO $_2$ at Copper Nanofoams,” *ACS Catal.*, vol. 4, no. 9, pp. 3091–3095, Sep. 2014.

[23] X. Wen *et al.*, “A reassembled nanoporous gold leaf electrocatalyst for efficient CO $_2$ reduction towards CO,” *Inorg. Chem. Front.*, vol. 5, no. 5, pp. 1207–1212, May 2018.

[24] K. P. Kuhl, E. R. Cave, D. N. Abram, and T. F. Jaramillo, “New insights into the electrochemical reduction of carbon dioxide on metallic copper surfaces,” *Energy Environ. Sci.*, vol. 5, no. 5, p. 7050, Apr. 2012.

[25] M. Azuma, K. Hashimoto, M. Hiramoto, M. Watanabe, and T. Sakata, “Electrochemical Reduction of Carbon Dioxide on Various Metal Electrodes in Low-Temperature Aqueous KHCO[sub 3] Media,” *J. Electrochem. Soc.*, vol. 137, no. 6, p. 1772, Jun. 1990.

[26] R. Kortlever, J. Shen, K. J. P. Schouten, F. Calle-Vallejo, and M. T. M. Koper, “Catalysts and Reaction Pathways for the Electrochemical Reduction of Carbon Dioxide,” *J. Phys. Chem. Lett.*, vol. 6, no. 20, pp. 4073–4082, Oct. 2015.

[27] A. Dutta, M. Rahaman, N. C. Luedi, M. Mohos, and P. Broekmann, “Morphology Matters: Tuning the Product Distribution of CO $_2$ Electroreduction on Oxide-

Derived Cu Foam Catalysts," *ACS Catal.*, vol. 6, no. 6, pp. 3804–3814, Jun. 2016.

[28] D. Raciti, M. Mao, and C. Wang, "Mass transport modelling for the electroreduction of CO_2 on Cu nanowires," *Nanotechnology*, vol. 29, no. 4, p. 044001, Jan. 2018.

[29] A. A. Peterson, F. Abild-Pedersen, F. Studt, J. Rossmeisl, and J. K. Nørskov, "How copper catalyzes the electroreduction of carbon dioxide into hydrocarbon fuels," *Energy Environ. Sci.*, vol. 3, no. 9, p. 1311, Aug. 2010.

[30] L. L. Snuffin, L. W. Whaley, and L. Yu, "Catalytic Electrochemical Reduction of CO2 in Ionic Liquid EMIMBF3Cl," *J. Electrochem. Soc.*, vol. 158, no. 9, p. F155, Sep. 2011.

[31] W. J. Durand, A. A. Peterson, F. Studt, F. Abild-Pedersen, and J. K. Nørskov, "Structure effects on the energetics of the electrochemical reduction of CO2 by copper surfaces," *Surf. Sci.*, vol. 605, no. 15–16, pp. 1354–1359, Aug. 2011.

[32] W. Tang *et al.*, "The importance of surface morphology in controlling the selectivity of polycrystalline copper for CO2 electroreduction," *Phys. Chem. Chem. Phys.*, vol. 14, no. 1, pp. 76–81, Dec. 2012.

[33] A. A. Peterson and J. K. Nørskov, "Activity Descriptors for CO_2 Electroreduction to Methane on Transition-Metal Catalysts," *J. Phys. Chem. Lett.*, vol. 3, no. 2, pp. 251–258, Jan. 2012.

[34] H. A. Hansen, J. B. Varley, A. A. Peterson, and J. K. Nørskov, "Understanding Trends in the Electrocatalytic Activity of Metals and Enzymes for CO $_2$ Reduction to CO," *J. Phys. Chem. Lett.*, vol. 4, no. 3, pp. 388–392, Feb. 2013.

[35] K. J. P. Schouten, E. Pérez Gallent, and M. T. M. Koper, "The influence of pH on the reduction of CO and CO2 to hydrocarbons on copper electrodes," *J. Electroanal. Chem.*, vol. 716, pp. 53–57, Mar. 2014.

[36] K. Manthiram, B. J. Beberwyck, and A. P. Alivisatos, "Enhanced Electrochemical Methanation of Carbon Dioxide with a Dispersible Nanoscale Copper Catalyst," *J. Am. Chem. Soc.*, vol. 136, no. 38, pp. 13319–13325, Sep. 2014.

[37] C. W. Li, J. Ciston, and M. W. Kanan, "Electroreduction of carbon monoxide to liquid fuel on oxide-derived nanocrystalline copper," *Nature*, vol. 508, no. 7497, pp. 504–507, Apr. 2014.

[38] C. Hahn *et al.*, "Engineering Cu surfaces for the electrocatalytic conversion of CO2: Controlling selectivity toward oxygenates and hydrocarbons.," *Proc. Natl. Acad. Sci. U. S. A.*, vol. 114, no. 23, pp. 5918–5923, Jun. 2017.

[39] R. Kas, R. Kortlever, H. Yılmaz, M. T. M. Koper, and G. Mul, "Manipulating the Hydrocarbon Selectivity of Copper Nanoparticles in CO $_2$ Electroreduction by Process Conditions," *ChemElectroChem*, vol. 2, no. 3, pp. 354–358, Mar. 2015.

[40] M. B. Ross *et al.*, "Tunable Cu Enrichment Enables Designer Syngas

Electrosynthesis from CO_2," *J. Am. Chem. Soc.*, vol. 139, no. 27, pp. 9359–9363, Jul. 2017.

[41] J. Resasco *et al.*, "Promoter Effects of Alkali Metal Cations on the Electrochemical Reduction of Carbon Dioxide," *J. Am. Chem. Soc.*, vol. 139, no. 32, pp. 11277–11287, Aug. 2017.

[42] D. Raciti *et al.*, "Low-Overpotential Electroreduction of Carbon Monoxide Using Copper Nanowires," *ACS Catal.*, vol. 7, no. 7, pp. 4467–4472, Jul. 2017.

[43] H. Ooka, M. C. Figueiredo, and M. T. M. Koper, "Competition between Hydrogen Evolution and Carbon Dioxide Reduction on Copper Electrodes in Mildly Acidic Media," *Langmuir*, vol. 33, no. 37, pp. 9307–9313, Sep. 2017.

[44] T. N. Huan, P. Simon, G. Rousse, I. Génois, V. Artero, and M. Fontecave, "Porous dendritic copper: an electrocatalyst for highly selective CO_2 reduction to formate in water/ionic liquid electrolyte," *Chem. Sci.*, vol. 8, no. 1, pp. 742–747, Dec. 2017.

[45] J. T. Feaster *et al.*, "Understanding the Influence of [EMIM]Cl on the Suppression of the Hydrogen Evolution Reaction on Transition Metal Electrodes," *Langmuir*, vol. 33, no. 37, pp. 9464–9471, Sep. 2017.

[46] E. L. Clark, C. Hahn, T. F. Jaramillo, and A. T. Bell, "Electrochemical CO_2 Reduction over Compressively Strained CuAg Surface Alloys with Enhanced Multi-Carbon Oxygenate Selectivity," *J. Am. Chem. Soc.*, vol. 139, no. 44, pp.

15848–15857, Nov. 2017.

[47] Y. Wang, D. Raciti, and C. Wang, "High-Flux CO Reduction Enabled by Three-Dimensional Nanostructured Copper Electrodes," *ACS Catal.*, vol. 8, no. 7, pp. 5657–5663, Jul. 2018.

[48] J. Feng, S. Zeng, J. Feng, H. Dong, and X. Zhang, "CO_2 Electroreduction in Ionic Liquids: A Review," *Chinese J. Chem.*, vol. 36, no. 10, pp. 961–970, Oct. 2018.

[49] Y. Hori, H. Wakebe, T. Tsukamoto, and O. Koga, "ELECTROCATALYTIC PROCESS OF CO SELECTIVITY IN ELECTROCHEMICAL REDUCTION OF CO2 AT METAL ELECTRODES IN AQUEOUS MEDIA," 1994.

[50] Y. Hori, "Electrochemical CO2 Reduction on Metal Electrodes," in *Modern Aspects of Electrochemistry*, New York, NY: Springer New York, 2008, pp. 89–189.

[51] D. Raciti, K. J. Livi, and C. Wang, "Highly Dense Cu Nanowires for Low-Overpotential CO_2 Reduction," *Nano Lett.*, vol. 15, no. 10, pp. 6829–6835, Oct. 2015.

[52] R. Reske, H. Mistry, F. Behafarid, B. Roldan Cuenya, and P. Strasser, "Particle Size Effects in the Catalytic Electroreduction of CO_2 on Cu Nanoparticles," *J. Am. Chem. Soc.*, vol. 136, no. 19, pp. 6978–6986, May 2014.

[53] F. S. Roberts, K. P. Kuhl, and A. Nilsson, "High Selectivity for Ethylene from

Carbon Dioxide Reduction over Copper Nanocube Electrocatalysts," *Angew. Chemie Int. Ed.*, vol. 54, no. 17, pp. 5179–5182, Apr. 2015.

[54] T. Egle *et al.*, "Multiscale Morphology of Nanoporous Copper Made from Intermetallic Phases," *ACS Appl. Mater. Interfaces*, vol. 9, no. 30, pp. 25615–25622, Aug. 2017.

[55] E. Benn, H. Uvegi, and J. Erlebacher, "Characterization of Nanoporous Metal-Ionic Liquid Composites for the Electrochemical Oxygen Reduction Reaction," *J. Electrochem. Soc.*, vol. 162, no. 10, pp. H759–H766, Jan. 2015.

[56] E. E. Benn, B. Gaskey, and J. D. Erlebacher, "Suppression of Hydrogen Evolution by Oxygen Reduction in Nanoporous Electrocatalysts," *J. Am. Chem. Soc.*, vol. 139, no. 10, pp. 3663–3668, Mar. 2017.

[57] J. T. Feaster *et al.*, "Understanding the Influence of [EMIM]Cl on the Suppression of the Hydrogen Evolution Reaction on Transition Metal Electrodes," *Langmuir*, vol. 33, no. 37, pp. 9464–9471, Sep. 2017.

[58] H. W. Pickering, "Formation of New Phases during Anodic Dissolution of Zn-Rich Cu-Zn Alloys," *J. Electrochem. Soc.*, vol. 117, no. 1, p. 8, Jan. 1970.

[59] Z. Wang, J. Liu, C. Qin, L. Liu, W. Zhao, and A. Inoue, "Fabrication and new electrochemical properties of nanoporous Cu by dealloying amorphous Cu–Hf–Al alloys," *Intermetallics*, vol. 56, pp. 48–55, Jan. 2015.

[60] Z. Qi *et al.*, “Formation and Characterization of Monolithic Nanoporous Copper by Chemical Dealloying of Al−Cu Alloys,” *J. Phys. Chem. C*, vol. 113, no. 16, pp. 6694–6698, Apr. 2009.

[61] C. Zhang, H. Yue, H. Wang, G. Ding, and Z. Xiaolin, “Nanoporous Copper Films with High Surface Area Formed by Chemical Dealloying from Electroplated CuZn Alloy,” *Micro Nanosyst.*, vol. 8, no. 1, pp. 13–18, Dec. 2016.

[62] I. C. Cheng and A. M. Hodge, “Morphology, Oxidation, and Mechanical Behavior of Nanoporous Cu Foams,” *Adv. Eng. Mater.*, vol. 14, no. 4, pp. 219–226, Apr. 2012.

[63] Z. Dan, F. Qin, Y. Sugawara, I. Muto, and N. Hara, “Fabrication of nanoporous copper by dealloying amorphous binary Ti–Cu alloys in hydrofluoric acid solutions,” *Intermetallics*, vol. 29, pp. 14–20, Oct. 2012.

[64] Z. Dan, F. Qin, A. Makino, Y. Sugawara, I. Muto, and N. Hara, “Fabrication of nanoporous copper by dealloying of amorphous Ti–Cu–Ag alloys,” *J. Alloys Compd.*, vol. 586, pp. S134–S138, Feb. 2014.

[65] C. Hou *et al.*, “Integrated Solid/Nanoporous Copper/Oxide Hybrid Bulk Electrodes for High-performance Lithium-Ion Batteries,” *Sci. Rep.*, vol. 3, no. 1, p. 2878, Dec. 2013.

[66] T. Aburada, J. M. Fitz-Gerald, and J. R. Scully, “Synthesis of nanoporous copper by dealloying of Al-Cu-Mg amorphous alloys in acidic solution: The effect of

nickel," *Corros. Sci.*, vol. 53, no. 5, pp. 1627–1632, May 2011.

[67] C. Zhao, Z. Qi, X. Wang, and Z. Zhang, "Fabrication and characterization of monolithic nanoporous copper through chemical dealloying of Mg–Cu alloys," *Corros. Sci.*, vol. 51, no. 9, pp. 2120–2125, Sep. 2009.

[68] J. R. Hayes, A. M. Hodge, J. Biener, A. V. Hamza, and K. Sieradzki, "Monolithic nanoporous copper by dealloying Mn–Cu," *J. Mater. Res.*, vol. 21, no. 10, pp. 2611–2616, Oct. 2006.

[69] X. Luo, R. Li, L. Huang, and T. Zhang, "Nucleation and growth of nanoporous copper ligaments during electrochemical dealloying of Mg-based metallic glasses," *Corros. Sci.*, vol. 67, pp. 100–108, Feb. 2013.

[70] J. Snyder and J. Erlebacher, "Kinetics of Crystal Etching Limited by Terrace Dissolution," *J. Electrochem. Soc.*, vol. 157, no. 3, p. C125, Mar. 2010.

[71] J. Weissmüller and K. Sieradzki, "Dealloyed nanoporous materials with interface-controlled behavior," *MRS Bull.*, vol. 43, no. 01, pp. 14–19, Jan. 2018.

[72] J. Snyder and J. Erlebacher, "The Active Surface Area of Nanoporous Metals during Oxygen Reduction," in *ECS Transactions*, 2011, vol. 41, no. 1, pp. 1021–1030.

[73] B. Hecker, C. Dosche, J. Knake, and M. Oezaslan, "Preparation and

Characterization of Nanoporous Copper Films by Chemical Dealloying," *ECS Trans.*, vol. 80, no. 10, pp. 541–550, Oct. 2017.

[74] F. Jia, J. Zhao, and X. Yu, "Nanoporous Cu film/Cu plate with superior catalytic performance toward electro-oxidation of hydrazine," *J. Power Sources*, vol. 222, pp. 135–139, Jan. 2013.

[75] Y. Peng, T. Wu, L. Sun, J. M. V. Nsanzimana, A. C. Fisher, and X. Wang, "Selective Electrochemical Reduction of CO_2 to Ethylene on Nanopores-Modified Copper Electrodes in Aqueous Solution," *ACS Appl. Mater. Interfaces*, vol. 9, no. 38, pp. 32782–32789, Sep. 2017.

[76] F. Jia, C. Yu, D. Kejian, and Z. Lizhi, "Nanoporous Metal (Cu, Ag, Au) Films with High Surface Area: General Fabrication and Preliminary Electrochemical Performance," 2007.

[77] A. Dutta, M. Rahaman, N. C. Luedi, M. Mohos, and P. Broekmann, "Morphology Matters: Tuning the Product Distribution of CO_2 Electroreduction on Oxide-Derived Cu Foam Catalysts," *ACS Catal.*, vol. 6, no. 6, pp. 3804–3814, Jun. 2016.

Chapter 3 - Motivation for a Flow Cell for Sequential Electrolysis

Introduction

Ammonia (NH_3) is an important industrial chemical with a wide range of uses, the most common being the nitrogen containing component in fertilizers used to increase crop yields. The nitrogen supplied from ammonia is so critical to agricultural yields that researchers have estimated that up to 50% of nitrogen in the typical human diet originates from ammonia based fertilizers [1]. Figure 3-1 illustrates the clear correlation between global population expansion and use of NH_3 derived from fertilizer throughout the 20th century [2]. These trends suggest that the demand for NH_3 and the energy required to produce it will increase as worldwide population increases throughout the remainder of the 21st century.

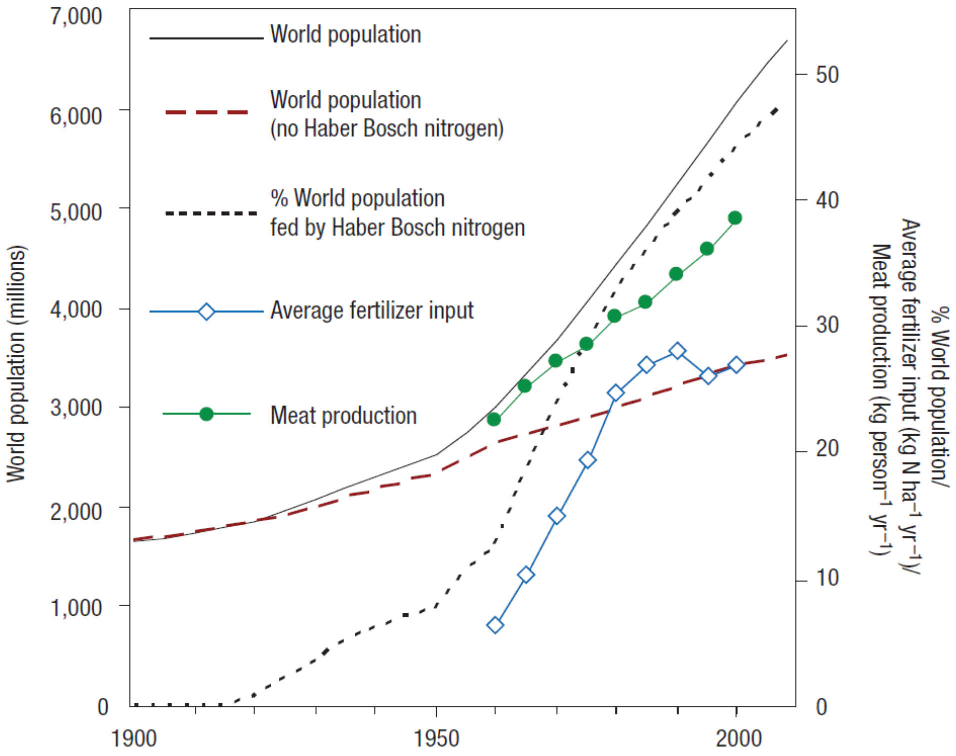

Figure 3-1. Trends in world population and Haber-Bosch derived nitrogen use in the 20th century. Figure reproduced from [2].

New NH_3 synthesis techniques that are environmentally friendly are needed in order to meet growing NH_3 demands while minimizing environmental harm associated with the energy intensive industrial process currently used to manufacture NH_3, the Haber-Bosch (HB) process. This famous process fixes hydrogen from H_2 to nitrogen from N_2 to form NH_3 over Fe based catalysts according to the reaction shown in Equation 3.1.

$$N_{2(g)} + 3H_{2(g)} \rightarrow 2NH_{3(g)} \qquad 3.1$$

The HB process has been well optimized and operates most effectively around 450 C and 150 atm with annual production exceeding 200 million metric tons globally [3]. The process is extremely energy intensive and requires large capital investments for the processing facilities in addition to large costs to transport and store ammonia away from these facilities [4]. Up to six percent of NH_3 produced by the HB process is lost during transport and storage away from the large central manufacturing facilities [5]. Since the H_2 used by HB is also typically supplied by steam methane reforming or other fossil fuels, the entire process to produce NH_3 contributes to a large portion of CO_2 emissions with 1.87 tons of CO_2 released per 1 ton of NH_3 generated by HB [6]. Production of NH_3 has accounts for almost 2% of energy use globally [7], and associated hydrogen production via steam methane reforming is associated with 100 million metric tons of CO_2 emissions. Development of a less energy intensive technique for NH_3 production capable of localized production would significantly lessen environmental impact, and is thus a widely researched topic.

Several alternative NH_3 synthesis techniques to the HB process have been discovered. Some processes focus on replicating the method found in nature, where enzymes produce NH_3 at ambient temperatures and pressures [8]–[11]. In lab settings, these processes can exhibit excellent selectivity but typically suffer from poor catalyst stability and the inability to supply necessary electrons for the reduction reaction from a conventional power supply as would be logically required for industrial scale production. Among other techniques that have been evaluated, electrochemical synthesis is a particularly attractive option as calculations have suggested that a low temperature and low pressure process with moderate overpotential (< 1 V) could be powered by renewable energy sources and performed at local scale [12]. The overall reaction for cathodic electrochemical reduction of N_2 to NH_3 is described by Equation 3.2 with an equilibrium potential nearly the same as the hydrogen evolution reaction (HER), and a solid catalyst is likely to be more robust with longer lifetime than current molecular based catalysts [13].

$$N_2 + 6H^+ + 6e^- \rightarrow 2NH_3 \qquad 3.2$$

In practice, this electrochemical reaction is a complex multistep process that exhibits poor kinetics due to correlated adsorption energies between key intermediates that must either adsorb or desorb and low selectivity as HER tends to dominate at the cathode and severely limits ammonia selectivity in aqueous environments [12], [14]. The origin of the selectivity for HER over ammonia synthesis lies in the nature of the reactants. Since protons (and water) are polar and N_2 is non-polar, driving the NH_3 reaction with large overpotentials at a negatively charged cathode naturally results in a large surface coverage of positively charged protons and negligible coverage of non-polar N_2 necessary for NH_3 synthesis. Computational researchers have modeled transition metals as possible catalysts and determined that Zr, Sc, Y and Ti might preferentially adsorb N_2 instead of protons under NH_3 reducing conditions in aqueous environments [15]. These elements are not at the peak of the volcano plot for NH_3 synthesis rates. Highly stepped Ru surfaces are the best elemental electrocatalyst and HB catalyst based on the conventional volcano plots when considering only nitrogen binding [16]–[18]. However, accounting only for nitrogen binding to the catalyst surface ignores the issue of competitive HER which dominates at most elemental surfaces and leads to low NH_3 formation rates. More recently nitrides have been proposed and demonstrated as promising electrocatalysts as the nitrided surface provides nitrogen for NH_3 rather than gaseous N_2, allowing for a differing reaction mechanism [19]–[22].

To date, many catalysts and electrochemical systems have been evaluated for low temperature low pressure electrocatalysis of NH3 [3], [23]–[32]. Regardless of the catalyst employed, these studies have yet to identify a competitive route for NH_3 synthesis with the HB process due to issues with poor catalyst selectivity and NH_3 synthesis rates.

Modeling and experimental work have clearly demonstrated the need for new catalysts or synthesis schemes to avoid detrimental HER for an electrocatalytic NH_3 synthesis technique competitive with the HB process. A study focusing on the selectivity of NH_3 electrocatalysts proposed that limiting the number of available protons at the electrocatalyst could limit the amount of HER and make NH_3 formation favorable at ambient conditions [12]. The use of an alkaline electrolyte is an obvious candidate for such a reaction scheme, and available water would supply the necessary hydrogen for the NH_3 product in this case. The limited experiments on NH_3 synthesis in alkaline conditions (including non-aqueous electrolytes) have shown promising selectivity results with some major drawbacks including severely limited catalyst life [33], [34].

In this work, we investigate a new technique that allows for precise control of proton delivery to the cathodic electrocatalyst through the use of sequential electrolysis in a flow cell with porous electrodes to allow for well controlled sequential electrochemical reactions. For production of NH_3 in such a setup, the proposed process works as follows: an electrolyte saturated with a mixture of N_2 and H_2 is flowed through porous electrodes where the first electrode oxidizes the H_2 to protons (HOR) to yield a specific concentration in the downstream flowing electrolyte. The potential applied at this electrode would have negligible effect on N_2 in the electrolyte. The second working electrode downstream reduces those protons generated at the first working electrode at high efficiency in the presence of adsorbed N_2 to form NH_3. The proposed process would allow for very specific control of reactant concentrations and reduction conditions through the use of the multiple working electrode approach that isn't available in a single cell setup. Since it's clear from past research that the local pH is critical to catalyst selectivity, this approach would add an extra degree of control for pH control beyond changing the pH of the electrolyte. It would also allow for tuning of H_2

and H^+ concentrations in the electrolyte and associated shifts in the Nernst potential for HER, which lies near that of N_2 reduction to NH_3, which also might affect catalyst selectivity. Use of two working electrodes would also allow for research of more complex reduction schemes, such as periodically pulsing the HOR electrode while maintaining sufficient potential at the reducing electrode to allow large N_2 surface coverage to develop prior to delivery of protons.

The use of a liquid electrolyte in the flow cell could avoid costs associated with expensive electrolytes as are used in many researched systems described above. H_2 or other hydrogen containing gases or fuels could be used as the H source as is done by the HB process. H_2 in particular might be conveniently supplied by renewable sources through electrolysis of water. It may also be possible to oxidize trace amounts of water in non-aqueous electrolytes to supply protons for NH_3 synthesis in the proposed flow cell setup. In any method of supplying H, the flow cell would no longer have to rely on acidic protons or concurrent water reduction at the NH_3 producing electrode for the hydrogen source as is required in a single cell approach.

The flow cell technique used above also seems well suited to other complex electrochemical reactions requiring intermediates, including electrochemical CO_2 reduction experiments. Other research has shown that Cu based catalysts exhibit greater Faradaic efficiencies towards useful products when reducing CO rather than CO_2 [35]–[37]. Approaches using numerous forms of bimetallic Au and Cu catalysts have yielded interesting results demonstrating that catalyst selectivity and efficiency can be dramatically altered by the composition and form of these catalysts.[38] Since certain metals can reduce CO_2 to CO at very large efficiencies and current densities (Au and Ag in particular) [39], it seems promising to adapt the flow cell approach presented here to decouple the CO_2 to CO to C reduction path through the use of a porous Au or Ag catalyst as the upstream electrode for efficient conversion of CO_2 to CO with a downstream working electrode of porous Cu for efficient conversion of CO to useful products.

Prior to attempting sequential electrolysis, we first focus on design aspects of the flow cell containing two separate and complete electrochemical cells, which exhibited electrochemical behavior typically avoided in conventional electrochemical cells due to the use of two separate electrochemical cells, one of which had behavior dependent on the other.

References

[1] V. Smil, “Detonator of the population explosion,” *Nature*, vol. 400, no. 6743, pp. 415–415, Jul. 1999.

[2] J. W. Erisman, M. A. Sutton, J. Galloway, Z. Klimont, and W. Winiwarter, “How a century of ammonia synthesis changed the world,” *Nat. Geosci.*, vol. 1, no. 10, pp. 636–639, Oct. 2008.

[3] V. Kyriakou, I. Garagounis, E. Vasileiou, A. Vourros, and M. Stoukides, “Progress in the Electrochemical Synthesis of Ammonia,” *Catal. Today*, vol. 286, pp. 2–13, May 2017.

[4] I. Chorkendorff and J. W. Niemantsverdriet, *Concepts of Modern Catalysis and Kinetics*. New York: Wiley-VCH, 2003.

[5] J. N. Galloway and E. B. Cowling, “Reactive Nitrogen and The World: 200 Years of Change,” *AMBIO A J. Hum. Environ.*, vol. 31, no. 2, pp. 64–71, Mar. 2002.

[6] R. Lan, J. T. S. Irvine, and S. Tao, “Synthesis of ammonia directly from air and water at ambient temperature and pressure.,” *Sci. Rep.*, vol. 3, p. 1145, 2013.

[7] C. J. M. van der Ham, M. T. M. Koper, and D. G. H. Hetterscheid, “Challenges in reduction of dinitrogen by proton and electron transfer,” *Chem. Soc. Rev.*, vol. 43, no. 15, pp. 5183–5191, Jul. 2014.

[8] J. S. Anderson, J. Rittle, and J. C. Peters, "Catalytic conversion of nitrogen to ammonia by an iron model complex," *Nature*, vol. 501, no. 7465, pp. 84–87, Sep. 2013.

[9] K. Arashiba, Y. Miyake, and Y. Nishibayashi, "A molybdenum complex bearing PNP-type pincer ligands leads to the catalytic reduction of dinitrogen into ammonia," *Nat. Chem.*, vol. 3, no. 2, pp. 120–125, Feb. 2011.

[10] B. K. Burgess and D. J. Lowe, "Mechanism of Molybdenum Nitrogenase," *Chem. Rev.*, vol. 96, no. 7, pp. 2983–3012, 1996.

[11] S. Mukherjee *et al.*, "Metal-organic framework-derived nitrogen-doped highly disordered carbon for electrochemical ammonia synthesis using N2 and H2O in alkaline electrolytes," *Nano Energy*, vol. 48, pp. 217–226, Jun. 2018.

[12] A. R. Singh *et al.*, "Electrochemical Ammonia Synthesis—The Selectivity Challenge," *ACS Catal.*, vol. 7, no. 1, pp. 706–709, Jan. 2017.

[13] J. Norskov and J. Chen, "Sustainable Ammonia Synthesis DOE Roundtable Report," 2016.

[14] J. H. Montoya, C. Tsai, A. Vojvodic, and J. K. Nørskov, "The Challenge of Electrochemical Ammonia Synthesis: A New Perspective on the Role of Nitrogen Scaling Relations," *ChemSusChem*, vol. 8, no. 13, pp. 2180–2186, Jul. 2015.

[15] E. Skúlason *et al.*, "A theoretical evaluation of possible transition metal electro-catalysts for N_2 reduction," *Phys. Chem. Chem. Phys.*, vol. 14, no. 3, pp. 1235–1245, Dec. 2012.

[16] A. Vojvodic *et al.*, "Exploring the limits: A low-pressure, low-temperature Haber–Bosch process," *Chem. Phys. Lett.*, vol. 598, pp. 108–112, Apr. 2014.

[17] K. Honkala *et al.*, "Ammonia Synthesis from First-Principles Calculations," *Science (80-.).*, vol. 307, no. 5709, pp. 555–558, Jan. 2005.

[18] S. Dahl *et al.*, "Role of Steps in N_2 Activation on Ru(0001)," *Phys. Rev. Lett.*, vol. 83, no. 9, pp. 1814–1817, Aug. 1999.

[19] J. G. Howalt and T. Vegge, "Electrochemical ammonia production on molybdenum nitride nanoclusters," *Phys. Chem. Chem. Phys.*, vol. 15, no. 48, p. 20957, Nov. 2013.

[20] I. Matanović, F. H. Garzon, and N. J. Henson, "Electro-reduction of nitrogen on molybdenum nitride: structure, energetics, and vibrational spectra from DFT," *Phys. Chem. Chem. Phys.*, vol. 16, no. 7, p. 3014, Jan. 2014.

[21] Y. Abghoui, A. L. Garden, V. F. Hlynsson, S. Björgvinsdóttir, H. Ólafsdóttir, and E. Skúlason, "Enabling electrochemical reduction of nitrogen to ammonia at ambient conditions through rational catalyst design," *Phys. Chem. Chem. Phys.*, vol. 17, no. 7, pp. 4909–4918, Feb. 2015.

[22] X. Zhang, R.-M. Kong, H. Du, L. Xia, and F. Qu, “Highly efficient electrochemical ammonia synthesis *via* nitrogen reduction reactions on a VN nanowire array under ambient conditions,” *Chem. Commun.*, vol. 54, no. 42, pp. 5323–5325, May 2018.

[23] Tsuyoshi Murakami, Tokujiro Nishikiori, and Toshiyuki Nohira, and Y. Ito*, “Electrolytic Synthesis of Ammonia in Molten Salts under Atmospheric Pressure,” 2002.

[24] C. G. Yiokari, G. E. Pitselis, D. G. Polydoros, and A. D. Katsaounis, and C. G. Vayenas*, “High-Pressure Electrochemical Promotion of Ammonia Synthesis over an Industrial Iron Catalyst,” 2000.

[25] G. Xu, R. Liu, and J. Wang, “Electrochemical synthesis of ammonia using a cell with a Nafion membrane and SmFe0.7Cu0.3−x Ni x O3 (x = 0−0.3) cathode at atmospheric pressure and lower temperature,” *Sci. China Ser. B Chem.*, vol. 52, no. 8, pp. 1171–1175, Aug. 2009.

[26] R. Lan, K. A. Alkhazmi, I. A. Amar, and S. Tao, “Synthesis of ammonia directly from wet air using new perovskite oxide La0.8Cs0.2Fe0.8Ni0.2O3-δ as catalyst,” *Electrochim. Acta*, vol. 123, pp. 582–587, Mar. 2014.

[27] V. Kordali, G. Kyriacou, and C. Lambrou, “Electrochemical synthesis of ammonia at atmospheric pressure and low temperature in a solid polymer electrolyte cell,”

Chem. Commun., vol. 0, no. 17, pp. 1673–1674, Jan. 2000.

[28] W. B. Wang, X. B. Cao, W. J. Gao, F. Zhang, H. T. Wang, and G. L. Ma, “Ammonia synthesis at atmospheric pressure using a reactor with thin solid electrolyte BaCe0.85Y0.15O3−α membrane,” *J. Memb. Sci.*, vol. 360, no. 1–2, pp. 397–403, Sep. 2010.

[29] L. Zhang *et al.*, “Electrochemical Ammonia Synthesis via Nitrogen Reduction Reaction on a MoS $_2$ Catalyst: Theoretical and Experimental Studies,” *Adv. Mater.*, vol. 30, no. 28, p. 1800191, Jul. 2018.

[30] S. Giddey, S. P. S. Badwal, and A. Kulkarni, “Review of electrochemical ammonia production technologies and materials,” *Int. J. Hydrogen Energy*, vol. 38, no. 34, pp. 14576–14594, Nov. 2013.

[31] D. S. Yun, J. H. Joo, J. H. Yu, H. C. Yoon, J.-N. Kim, and C.-Y. Yoo, “Electrochemical ammonia synthesis from steam and nitrogen using proton conducting yttrium doped barium zirconate electrolyte with silver, platinum, and lanthanum strontium cobalt ferrite electrocatalyst,” *J. Power Sources*, vol. 284, pp. 245–251, Jun. 2015.

[32] I. A. Amar, R. Lan, C. T. G. Petit, V. Arrighi, and S. Tao, “Electrochemical synthesis of ammonia based on a carbonate-oxide composite electrolyte,” *Solid State Ionics*, vol. 182, no. 1, pp. 133–138, Feb. 2011.

[33] J. N. Renner, L. F. Greenlee, K. E. Ayres, and A. M. Herring, "Electrochemical Synthesis of Ammonia: A Low Pressure, Low Temperature Approach," *Interface Mag.*, vol. 24, no. 2, pp. 51–57, Jan. 2015.

[34] S. Licht, B. Cui, B. Wang, F.-F. Li, J. Lau, and S. Liu, "Ammonia synthesis. Ammonia synthesis by N_2 and steam electrolysis in molten hydroxide suspensions of nanoscale Fe_2O_3.," *Science*, vol. 345, no. 6197, pp. 637–40, Aug. 2014.

[35] C. W. Li, J. Ciston, and M. W. Kanan, "Electroreduction of carbon monoxide to liquid fuel on oxide-derived nanocrystalline copper," *Nature*, vol. 508, no. 7497, pp. 504–507, Apr. 2014.

[36] D. Raciti *et al.*, "Low-Overpotential Electroreduction of Carbon Monoxide Using Copper Nanowires," *ACS Catal.*, vol. 7, no. 7, pp. 4467–4472, Jul. 2017.

[37] Y. Wang, D. Raciti, and C. Wang, "High-Flux CO Reduction Enabled by Three-Dimensional Nanostructured Copper Electrodes," *ACS Catal.*, vol. 8, no. 7, pp. 5657–5663, Jul. 2018.

[38] J. W. Vickers, D. Alfonso, and D. R. Kauffman, "Electrochemical Carbon Dioxide Reduction at Nanostructured Gold, Copper, and Alloy Materials," *Energy Technol.*, vol. 5, no. 6, pp. 775–795, Jun. 2017.

[39] Y. Hori, H. Wakebe, T. Tsukamoto, and O. Koga, "ELECTROCATALYTIC

PROCESS OF CO SELECTIVITY IN ELECTROCHEMICAL REDUCTION OF CO2 AT METAL ELECTRODES IN AQUEOUS MEDIA,” 1994.

Chapter 4 - Flow Cell for Sequential Electrolysis

Introduction

In this chapter we demonstrate the principles and performance of a sequential reaction flow cell containing two complete electrochemical cells that we designed and produced to achieve sequential electrochemical reactions of the type described in the previous chapter. We designed the cell to allow the highest degree of control over reactant concentrations at the working electrodes as achieving this objective seemed optimal for studying complex reactions such as NH_3 synthesis and CO_2 reduction. However, the sequence of electrodes that allowed precise control over concentrations prevented one of the electrochemical cells from operating independently. Using fundamental electrochemical analysis of the flow cell, we present a new method for accurately determining the effect of the independent electrochemical cell on the non-independent cell and show how the method allows for accurate control of the non-independent cell using a model set of reactions. Based on these results we demonstrate (in the following chapter) the usefulness of the flow cell through detailed study of the properties of several catalysts for the model electrochemical reaction system.

Experimental

Flow Cell Design

A modular flow cell was designed and manufactured for sequential electrolysis experiments as outlined in the previous chapter. The cell is pictured and diagrammed in Figure 4-1 and Figure 4-2. HDPE plates with aligned center holes were secured together to construct the flow cell with a central cylindrical channel. Neoprene gaskets were placed between the plates to ensure a leak proof cell design. The cell materials were selected to allow for compatibility with non-aqueous electrolytes.

Four stainless steel bolts were used to hold the cell together and apply adequate pressure to prevent leaks. The limiting diameter in the flow channel was 6 mm and located at the HER working electrode. Plates with 6 mm diameters placed immediately upstream and downstream of the HER working electrode extended the 6 mm diameter channel approximately 7 mm both upstream and downstream of the HER working electrode. A series of porous or mesh electrodes were located sequentially in the flow channel to create two complete electrochemical cells within the flow cell. A peristaltic pump circulated the electrolyte. Several hundred mL of the electrolyte was held in an external container to the flow cell and continuously purged with H_2 or N_2 through a 40-60 um porous frit during experiments to provide adequate gas saturation.

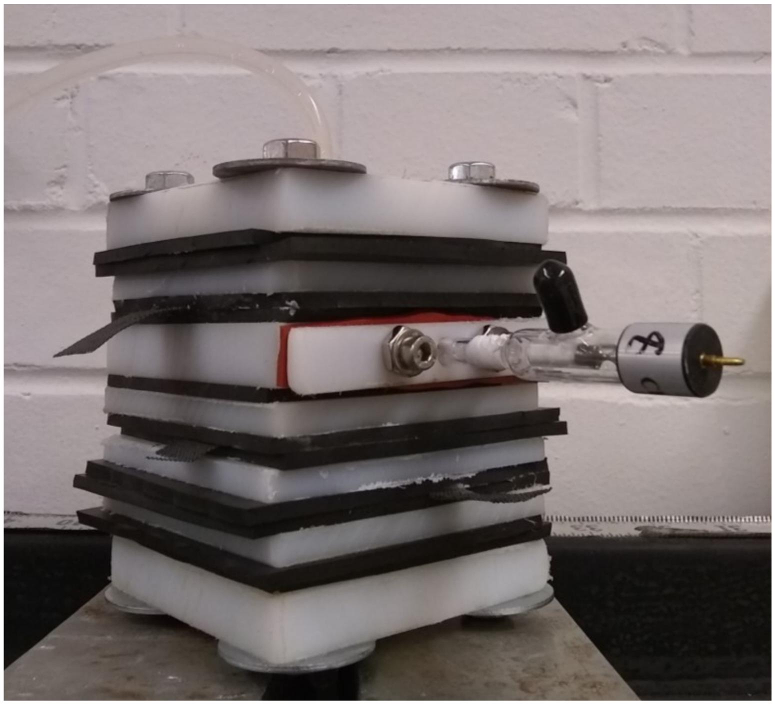

Figure 4-1. The flow cell as assembled.

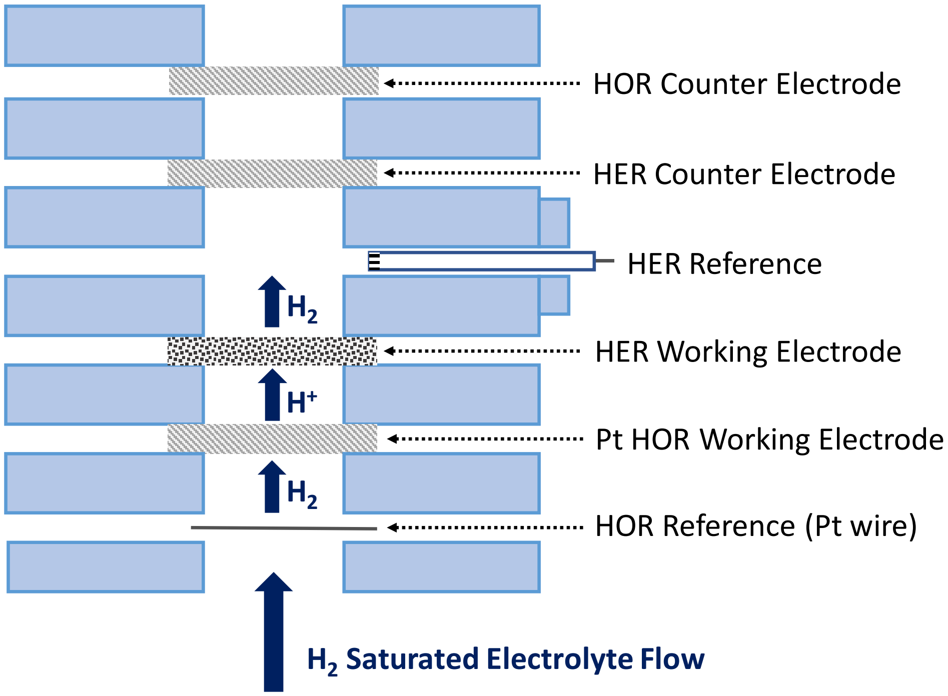

Figure 4-2. Sectional diagram of the flow cell. Blue shapes represent the HDPE plates. Note that gaskets placed between the plates to seal the flow channel are omitted for simplicity.

The HER working electrode was located approximately 6 mm downstream from the HOR working electrode. The porous frit of the reference electrode, a saturated mercury sulfate (MSE), was located just downstream of the Nb working electrode. The MSE reference was placed into the flow cell through a gasket sealed port to the exterior of the cell. Downstream from the HER reference were the counter electrodes of Pt mesh or carbon cloth.

Sequential electrolysis with two complete electrochemical cells has been explored in previous research [1], [2]. This work differs in two key aspects. First, the counter electrodes were placed downstream from the working electrodes and concentrated supporting electrolytes were used to minimize the flow of any reaction products from the counter electrodes through the working electrodes. This setup allowed for finer control over the electrolytic environment at the electrodes of interest. Second, the electrolyte was flowed at 40 mL/min (+/- 1 mL/min) which was approximately an order of magnitude or more or greater than flow rates required for large conversion efficiencies typically employed for detailed study of electrolytic reaction efficiencies under flowing conditions in porous electrodes [1]–[7]. Greater flow rates and thus greater production rates are desirable for industrial applications (provided the hydrodynamic resistance to flow is considered), so we employed larger flow rates to assess the viability of our flow cell approach and porous electrodes. All measurements hereafter were performed at 39-41 mL/min unless noted otherwise.

Electrochemical Considerations in the Flow Cell

The setup of the flow cell presented unique experimental challenges which are typically avoided in other electrochemical cells containing multiple working electrodes, such as conventional rotating ring/disc electrodes (RRDE) and other similar flow cells. In the multi-working electrode setups, coupling of the working electrodes is generally avoided through appropriate setup of the cell geometry, meaning that the working electrodes operate entirely independent of each other even when paired to the same reference and counter electrodes in a bipotentiostat setup. In the flow cell used in this study, the HER cell could not operate independently of the HOR cell as the electrodes of the HER cell were located between the working and counter of the HOR cell.

Use of a bipotentiostat with a shared counter electrode was initially attempted in multiple electrode configurations, but such a setup proved unsuitable as we found no way to arrange the cell that didn’t couple the two working electrodes. For this reason, two independent cells controlled by their own potentiostat were employed. Figure 4-3 shows a simplified schematic of the circuitry of the flow cell along with the resistance between the HER working and reference electrode, which was an important aspect to consider for data interpretation.

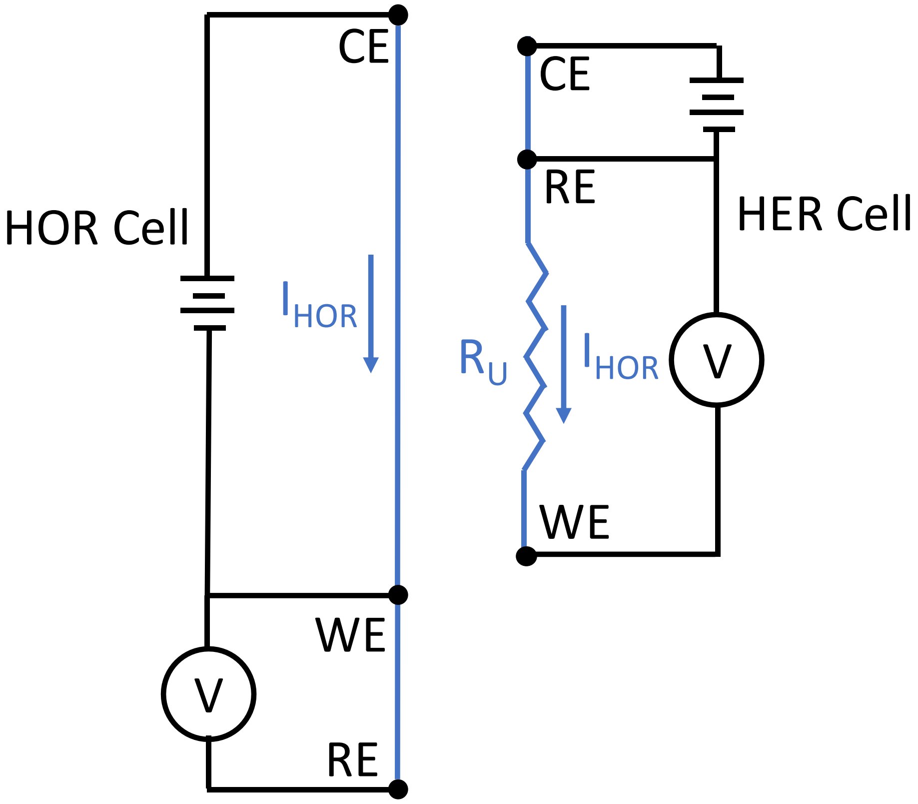

Figure 4-3. Circuit diagram of the flow cell highlighting the HOR current and uncompensated HER resistance responsible for the potential shift observed at the HER cell due to applied current in the HOR cell. Paths and currents shown in blue represent those in the electrolyte. The working, counter and reference electrodes are denoted WE, CE and RE respectively.

The HOR cell operated independently of the HER cell since the HOR cell electrodes were located outside of the HER cell. As the HOR operated in galvanostatic modes, the generated current necessarily flowed between the working and counter electrodes of the HOR cell. As Figure 4-3 shows, the HOR current (I_{HOR}) also had to flow entirely through porous electrodes of the HER cell via the electrolyte. Since the HER cell had inherent solution resistance (R_U) between the working and reference electrodes, an associated potential drop due to current flow across this resistance was unavoidable.

The application of current in the HOR cell therefore caused the potential measured between the HER working electrode and its reference to shift. The shift was an artefact of the cell geometry and unrelated to faradaic processes at the HER working electrodes. This shift was consistent, repeatable and extremely linear with applied current in the HOR cell (and unrelated to applied potential in the HOR cell). We characterized the potential shifts in the HER cell caused by HOR current by measuring the change in open circuit potential or the potential required to pass zero charge at the HER working electrode upon application of brief pulses of current in the HOR cell. Accounting for these shifts allowed for complete characterization of the HOR/HER characteristics of the cell without including non-faradaic effects measured at the HER working electrode due to flow cell geometry.

A Metrohm Autolab potentiostat controlled the HOR cell, and a Gamry Interface 1000 potentiostat controlled the HER cell. A repeating galvanostatic pulse experiment revealed the non-Faradaic effects of the HOR cell current on the HER cell as well as the uncompensated resistance of the HER cell. As the HOR potentiostat pulsed the HOR cell to various currents (-2, 0.5, 1, 2, and 4 mA) for 0.5 seconds, the measured open circuit potential or potential to pass zero current in the HER cell pulsed in response. The slope of the maximum potential shift at the HER electrode plotted as a function current applied through the HOR cell was also assumed to be the uncompensated resistance of the HER cell, and the measured resistance was used to correct the HER data post experiment. A Mettler Toledo SevenExcellence pH meter was used to measure the pH of the electrolytes. All electrolytes consisted of ultrapure water at greater than 18 MOhm resistance and reagent grade Na_2SO_4 (Sigma Aldrich). Since all tests employed 1M Na_2SO_4, we omit this detail in further experimental descriptions. The cell was flushed with ultrapure water prior to use with each working electrode. The flow rate was determined by timing the volumetric flow of ultrapure water into a graduated cylinder for each working electrode. Platinum electrodes were cleaned in concentrated nitric acid followed by flame annealing under an H_2 torch prior to assembly of the electrochemical flow cell.

Results and Discussion

HER Electrode Response to HOR Cell

Prior to measuring the effects of upstream HOR on HER at various working electrodes, the effects of placing all the electrodes of the HER cell within the HOR cell were determined for each working electrode. Figure 4-4 shows the measured open circuit potential at a porous Nb electrode as a function of time while the upstream HOR electrode was pulsed to various currents. Between these pulses, the HOR electrode was held galvanostatically at 0 mA of current for 5 seconds.

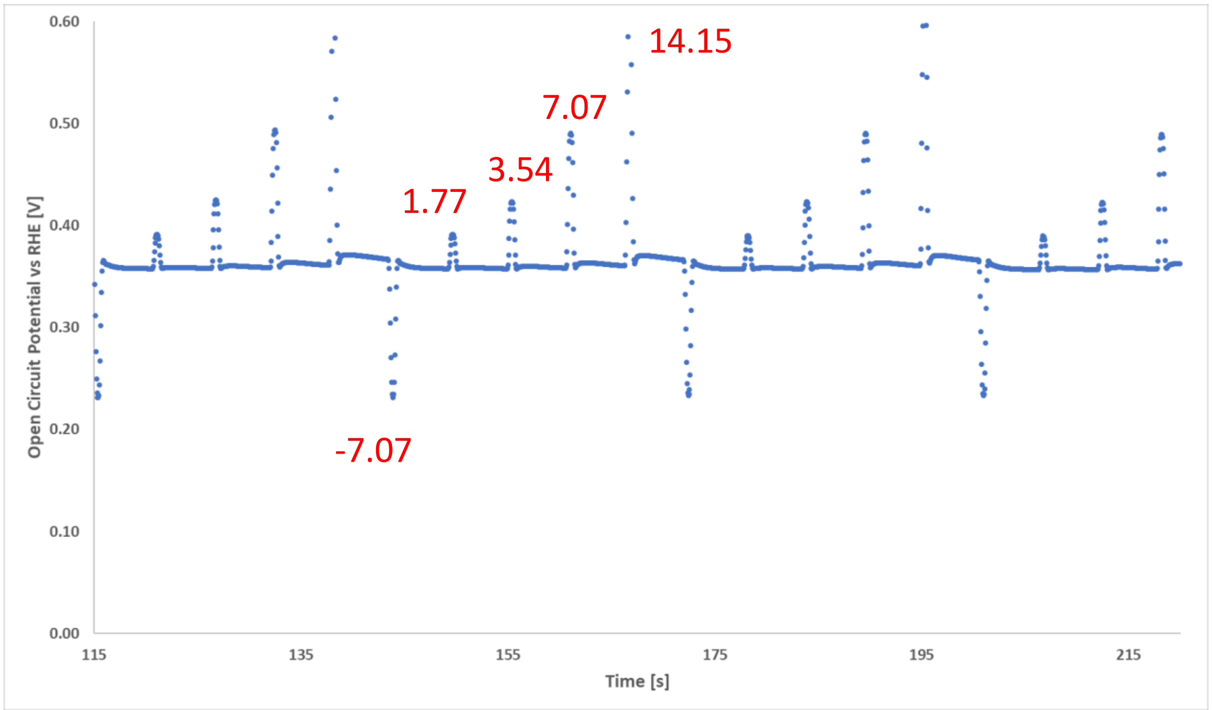

Figure 4-4. Open circuit potential of a porous Nb sample at the HER working electrode while the HOR working electrode (Pt mesh) was pulsed to the current densities noted in red (in mA/cm^2) from a baseline HOR current of 0 mA/cm^2. The

The deviations from the baseline open circuit potential (when the applied HOR current was 0 mA/cm^2) were measured three times for each HOR current pulse and plotted as a function of the applied current in Figure 4-5.

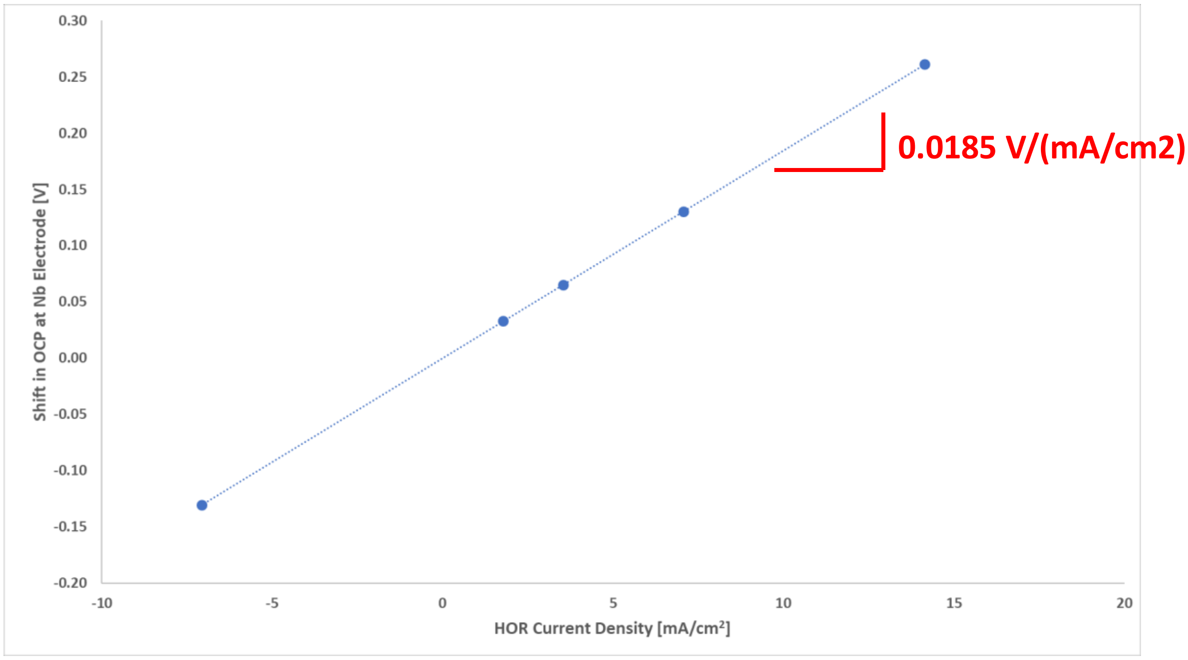

Figure 4-5. Open circuit potential shift at a porous Nb HER working electrode as a function of applied HOR current density obtained from the data in Figure 4-4.

The data in Figure 4-5 exhibit linearity with minimal variation in the response of the HER cell OCP with applied current at the HOR cell. The slope of this line as calculated in with each working electrode was then used to calculate the appropriate potential offset to apply to each data point when the response of the HER cell was evaluated in detail at various HOR current densities. This slope was also used to calculate the uncompensated resistance of the cell for each working electrode (65 ohms based on the slope of 0.0185 V*cm^2/mA and a 6 mm diameter).

The open circuit potential of the working electrode varied depending on electrolyte flow rate in the flow cell. Figure 4-6 shows an example of the open circuit potential of a Pt mesh electrode at 40 mL/min flow rate and no flow. The open circuit potential shifted approximately 60 mV positive when the electrolyte was flowing. While this shift did not affect the catalytic properties of the working electrodes, it proved useful in analysis of polarization curves shown later where HER appears to begin positive of 0 V vs RHE in some cases. The reference electrode was calibrated by conventional techniques employing bubbling of H_2 over a Pt electrode under ambient conditions leading to the apparent shift from 0 mV versus RHE in the flow cell environment.

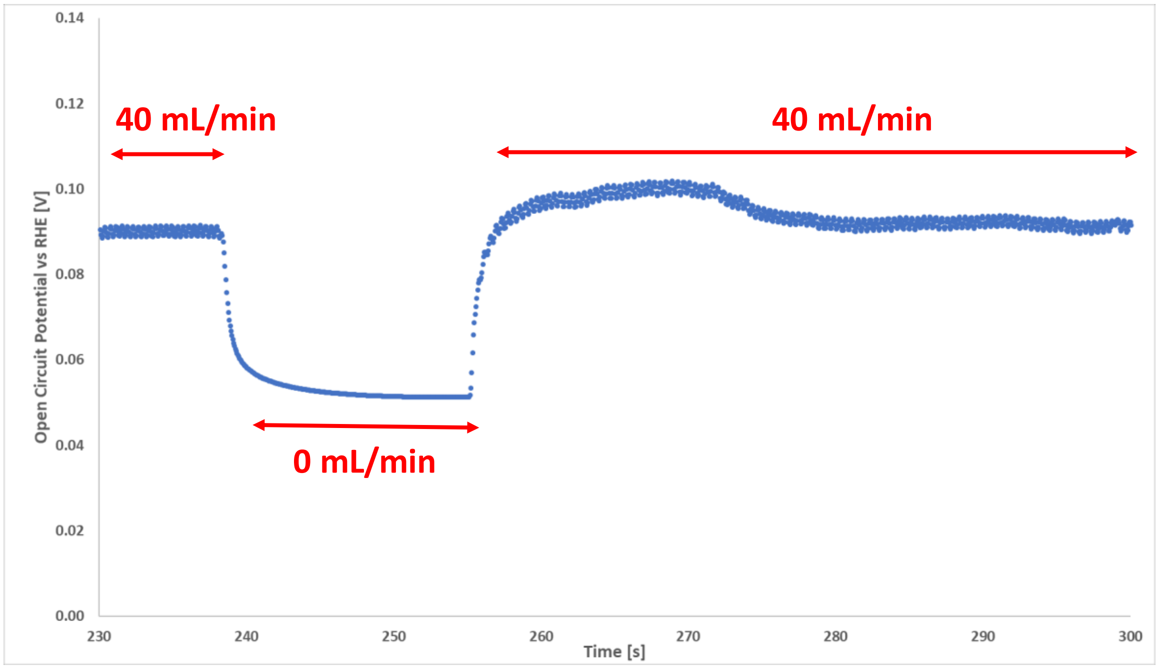

Figure 4-6. Open circuit potential of a Pt mesh electrode as function of time under the noted flow rates in H_2 saturated electrolyte.

The HOR cell was held at fixed current while cyclic voltammetry (CV) was performed on a porous Nb working electrode in order to measure the response of the HER cell to HOR current. Figure 4-7 and Figure 4-8 show collected CV data with (Figure 4-8) and without (Figure 4-7) the calculated potential shift described above applied to the data.

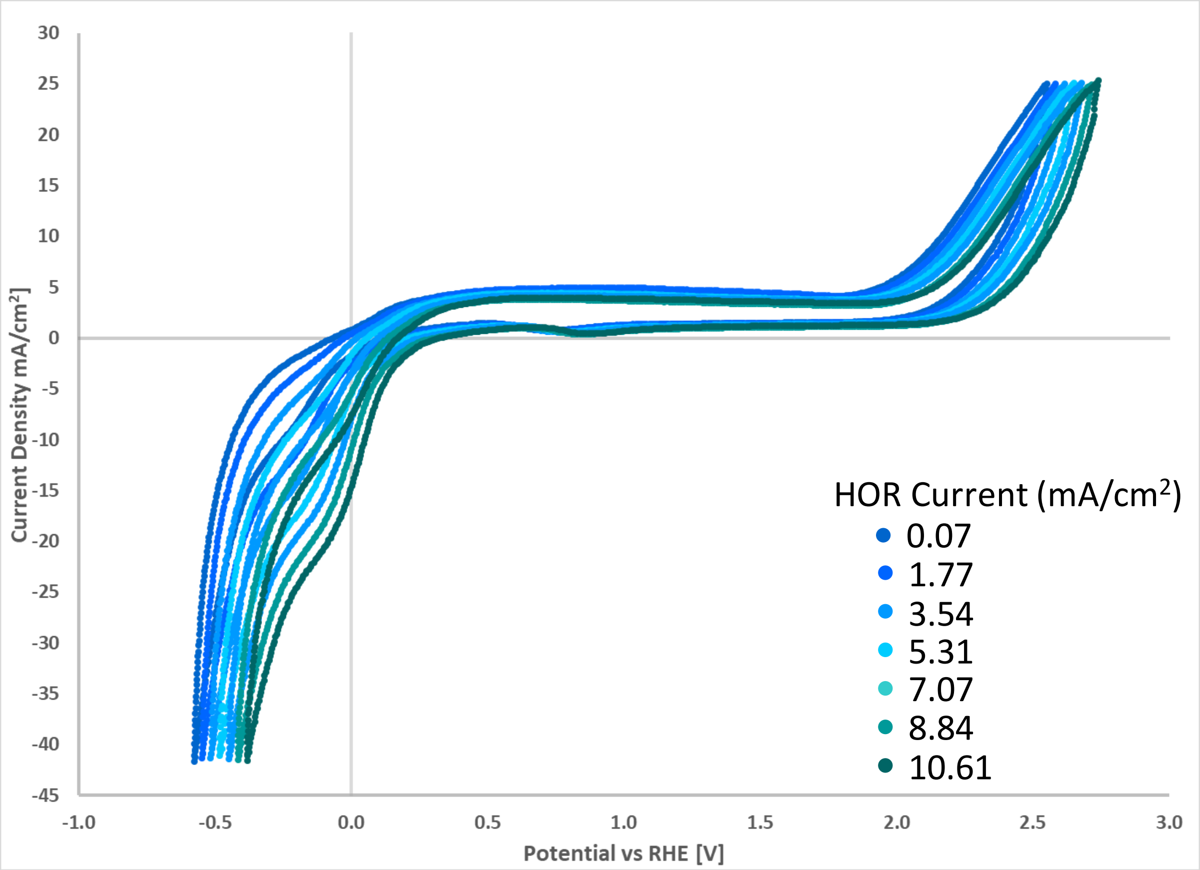

Figure 4-7. Cyclic voltammograms (50 mV/sec) of a porous Nb HER working electrode in H_2 saturated electrolyte with the upstream HOR working electrode operating at the noted current densities. These data were not shifted to account for the effects of the HOR cell current passing through the HER cell.

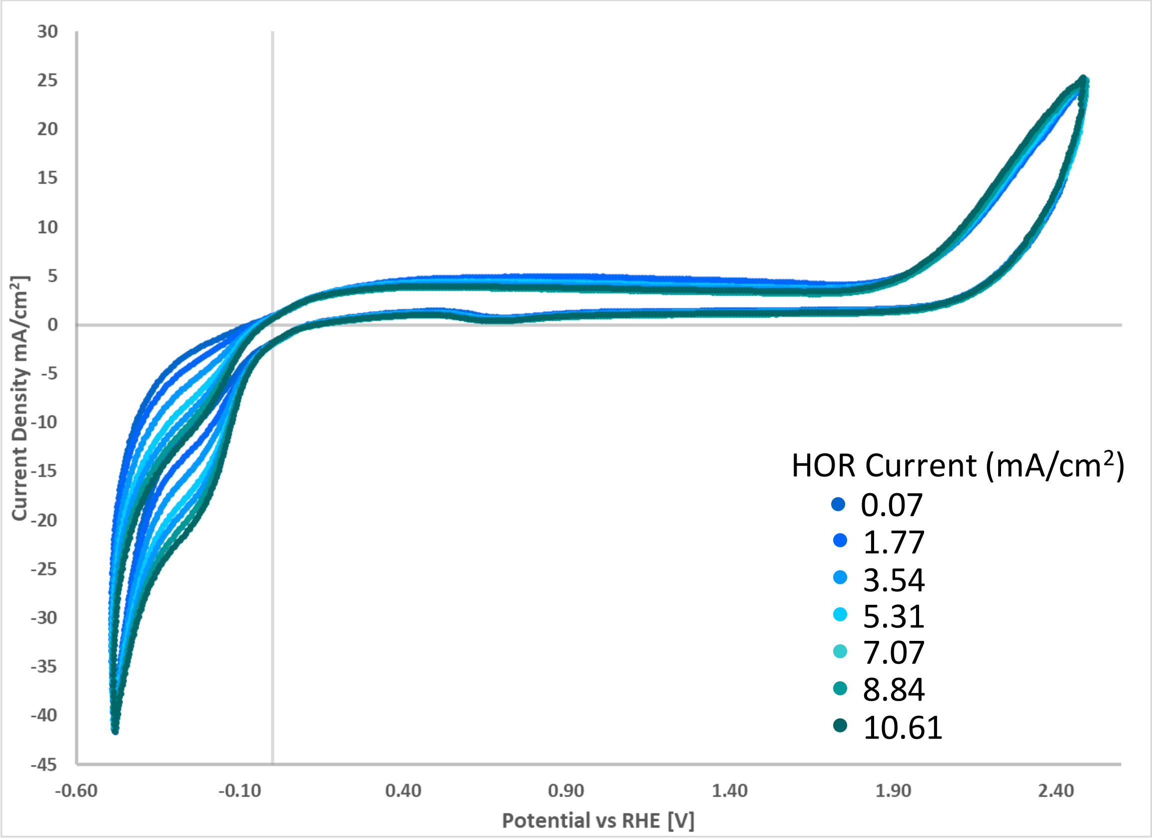

Figure 4-8. Cyclic voltammograms from Figure 4-7 with the potentials shifted to account for the effects of the HOR current passing through the HER cell.

The curves in Figure 4-8 line up well after the applied potential shift especially in the region of water oxidation (> 1.8 V) where the upstream HOR current was expected to have minimal impact on the voltammetry characteristics, showing that the applied shifts due to current passing through the HOR cell were appropriate for analysis of the flow cell system. All HER voltammetry data from here onwards in this work were shifted appropriately to account for HOR current effects.

Conclusions

A sequential flow cell was designed and manufactured to allow for precise control of two separate electrochemical cells with the two working electrodes located at the inlet side of the cell and the counter electrodes at the outlet side. This design allowed for precise control over the reactant concentrations at the working electrodes with minimal exposure of the working electrodes to anodic reaction products, but the design also prevented one of the electrochemical cells from operating independently. This limitation was overcome by characterizing the influence of passing current from the outer HOR cell through the uncompensated resistance of the inner HER cell. The experimental data showed that sequential electrochemical reactions could be performed with precise and independent control over the HOR cell as well as the HER cell by accounting for HOR current effects within the flow cell. The proper potential shifts to apply to the HER cell to account for the uncompensated resistance of the HER cell were accurately determined thorough simple characterization of the effects of the HOR current on the HER cell at open circuit or galvanostatic control at zero current. The HER potential shifts measured during pulsing of the HOR current over a wide range of current densities demonstrated repeatable measurement associated with a linear resistance in the HER cell which matched the prediction that these shifts were associated purely with the uncompensated resistance of the HER cell. Accounting for the potential shift on raw polarization data from an HER working electrode at various

HOR current densities aligned characteristic and fixed H_2O oxidation peaks, which proved the approach could be applied to study of sequential reactions where the effects of the upstream HOR current might strongly affect voltammetry characteristics at the working electrode. In the following chapter, detailed examination of sequential electrolysis is performed with the flow cell.

References

[1] C. Lamoureux, C. Moinet, and A. Tallec, “An electrolysis cell with close consecutive flow-through porous electrodes for particular organic electrosynthesis,” *J. Appl. Electrochem.*, vol. 16, no. 6, pp. 819–824, Nov. 1986.

[2] J. V. Kenkel and A. J. Bard, “A dual working electrode coulometric flow cell,” *J. Electroanal. Chem. Interfacial Electrochem.*, vol. 54, no. 1, pp. 47–54, Jul. 1974.

[3] S. Kihara, T. Yamamoto, K. Motojima, and T. Fujinaga, “Determination of plutonium by two-step flow-coulometry at the column electrode,” *Talanta*, vol. 19, no. 5, pp. 657–668, May 1972.

[4] B. G. Ateya, E. A. S. Arafat, and S. A. Kafafi, “Hydrodynamic effects on the efficiency of porous flow-through electrodes,” *J. Appl. Electrochem.*, vol. 7, no. 2, pp. 107–112, Mar. 1977.

[5] R. E. Sioda, “Electrolysis with flowing solution,” *Electrochim. Acta*, vol. 13, no. 3, pp. 375–382, Mar. 1968.

[6] W. J. Blaedel and J. Wang, “Flow electrolysis on a reticulated vitreous carbon electrode,” *Anal. Chem.*, vol. 51, no. 7, pp. 799–802, Jun. 1979.

[7] E. Beinrohr, M. Nemeth, P. Tschopel, and G. Tolg, “Design and characterization of flow-through coulometric cells with porous working electrodes made of

crushed vitreous carbon," *Fresenius. J. Anal. Chem.*, vol. 343, no. 7, pp. 566–575, 1992.

Chapter 5 – Porous Niobium for Sequential HOR and HER

Introduction

After demonstrating that the flow cell in the previous chapter allowed for precise control over both electrochemical cells within the flow channel, we examine in this chapter a sequential electrochemical reaction performed at large current densities as a simple model for analogous and complex protonation reactions using H_2 as a proton source. The studied reactions have direct implications for NH_3 synthesis as hydrogen is employed in current industrial processes and is a feasible emission-free proton source for a large-scale electrochemical synthesis technique. The research presented in this chapter focuses on the general ability of the system to utilize hydrogen and protons in electrochemical reactions in the flow cell as well as the specific effects that morphology and activity have on the efficiency of various porous catalysts. Special attention is given to a robust form of NP-Nb, which exhibits high efficiency for reducing protons created by upstream H_2 oxidation as a bare catalyst and can be improved for the reaction through functionalization with Pt nanoparticles.

The sequential electrochemical reactions consist of oxidation of gaseous Hydrogen to protons (HOR) and reduction of those created protons back to Hydrogen (HER) in an aqueous environment under mildly acidic conditions. Equation 5.1 shows the simple electrochemical reduction reaction (the oxidation simply runs in the reverse order), which has an equilibrium potential of 0 mV versus RHE in aqueous acidic electrolytes by definition.

$$2H^{+} + 2e^{-} \rightarrow H_{2(g)} \qquad 5.1$$

These well studied oxidation and reduction reactions were chosen for several reasons [1]–[8]. The reaction avoided fixing the protons to a different atom or molecule, which would have added additional complexity to the reduction reaction and complicated analysis of the efficiency of the cell. We performed the well characterized HOR and HER reactions in an aqueous environment such that we with knew with a high degree of confidence what the reactants and products of each electrochemical reaction were (hydrogen and protons) without requiring additional characterization by GCMS, liquid NMR or other techniques to determine the products as is necessary in reactions, such as ammonia synthesis, with multiple reaction pathways to multiple products. The simple reactions then allowed us to assign the current measured to either oxidation of H_2 or reduction of H^+ (with one exception discussed later), and this simplification over a more complex reaction allowed for simple calculation of HER conversion efficiencies. The use of H_2 as the source gas for protons was also directly applicable to NH_3 synthesis and allowed us to determine if this type of flow cell with large flow rates and current densities compared could be a feasible choice for studies of NH_3 production from simple source gases in future studies.

Experimental

Gas purged 1M Na_2SO_4 was pumped through the flow cell described in the previous chapter. HOR was performed at a Pt mesh electrode of the HOR electrochemical cell, and sustained oxidative current on the order of several mA was possible with four Pt meshes. A Pt wire pseudo-reference was used for the HOR cell rather than a conventional reference electrode due to the high pressure in the flow cell between the peristaltic pump rollers and the porous Nb electrode when it was used for HER. The pressure in the cell at the location of the HOR reference was great enough to pump electrolyte through the porous frits of conventional reference electrodes when the porous Nb was used as the working electrode downstream.

Porous Nb electrodes were fabricated through a liquid metal dealloying process recently developed in the lab. Briefly, a thin slice of homogenous and solid solution $Nb_{60}Ti_{37}Si_3$ was immersed in liquid copper at approximately 1200 C for several minutes to obtain complete dealloying through the TiNbSi sample. Since Nb is virtually insoluble in liquid Cu, only the Ti and a fraction of the Si dissolved, leaving behind a characteristic porous structure generated by dealloying as described earlier in Chapter 1. The Si and Nb also formed a silicide during dealloying that grew in plate morphologies perpendicular to the dealloying front and spanned grain boundaries within the porous Nb. These silicides stabilized the porous Nb which was inherently brittle in their absence, adding strength to the material and making it suitable for use in the flow cell. The porous Nb electrode was 1.04 mm thick with pore sizes on the order of 1-10 μm. Figure 5-1 shows an SEM micrograph of the porous Nb material.

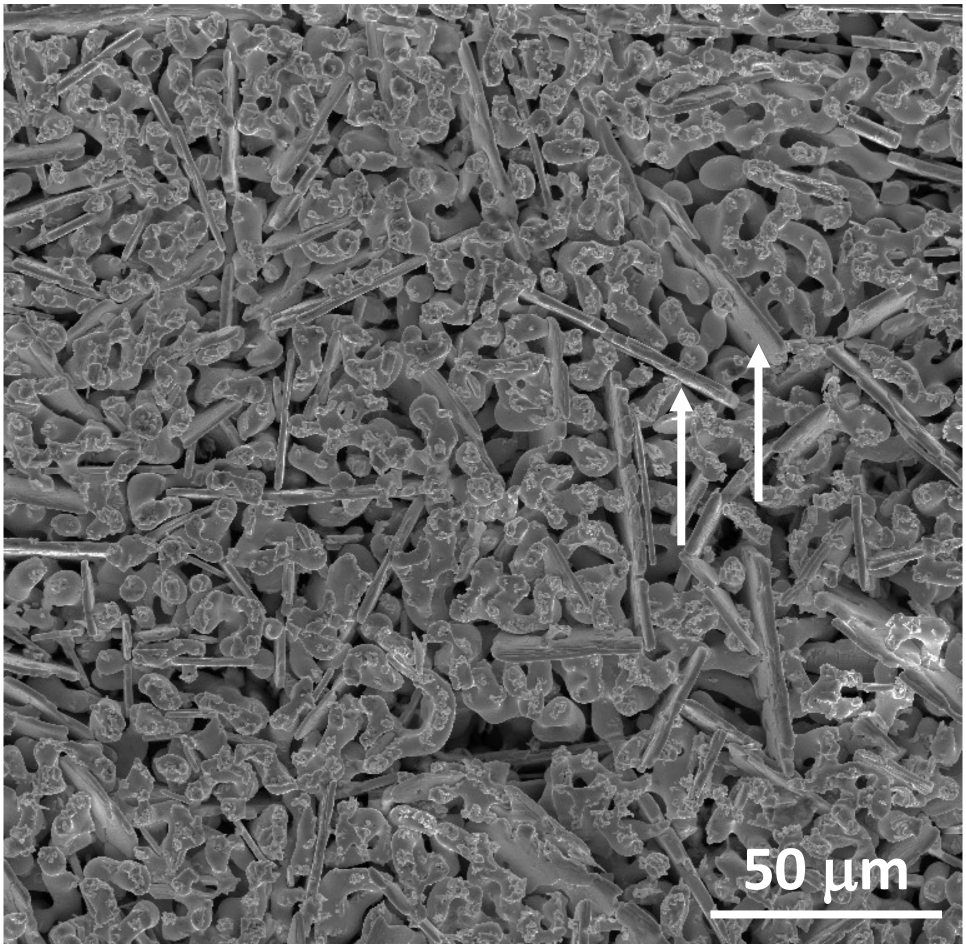

Figure 5-1. Plan view SEM micrograph of porous Nb. The white arrows mark Nb silicides located throughout the sample that provided mechanical stability.

The surface area of the Nb electrodes was characterized through capacitance measurements on a porous Nb sample in the flow cell in 100 mM K_2SO_4 saturated with

N_2. Figure 5-2 shows cyclic voltammetry performed on porous Nb at various scan rates within the potential range of 100 mV and -200 mV versus a saturated mercury sulfate reference (MSE). Figure 5-3 shows the plot of the difference in current on the positive and negative slopes versus scan rate, and the slope of the linear fit was used to calculate the capacitance. Similar capacitance measurements were performed on a piece of polished Nb (polished to 0.5 micron finish) with an exposed surface of known area. The capacitance per area (30.3 uF/cm^2) was used to calculate the specific surface area of porous Nb, which was calculated to be 161 cm^2/g. The total volume of the piece of porous Nb was also measured and the surface area per geometric volume was found to be 482 cm^{-1}. The porosity fraction of the Nb sample was determined to be 49% as calculated by measuring the solid volume of the sample in a Micromeritics AccuPyc II 1340 pycnometer.

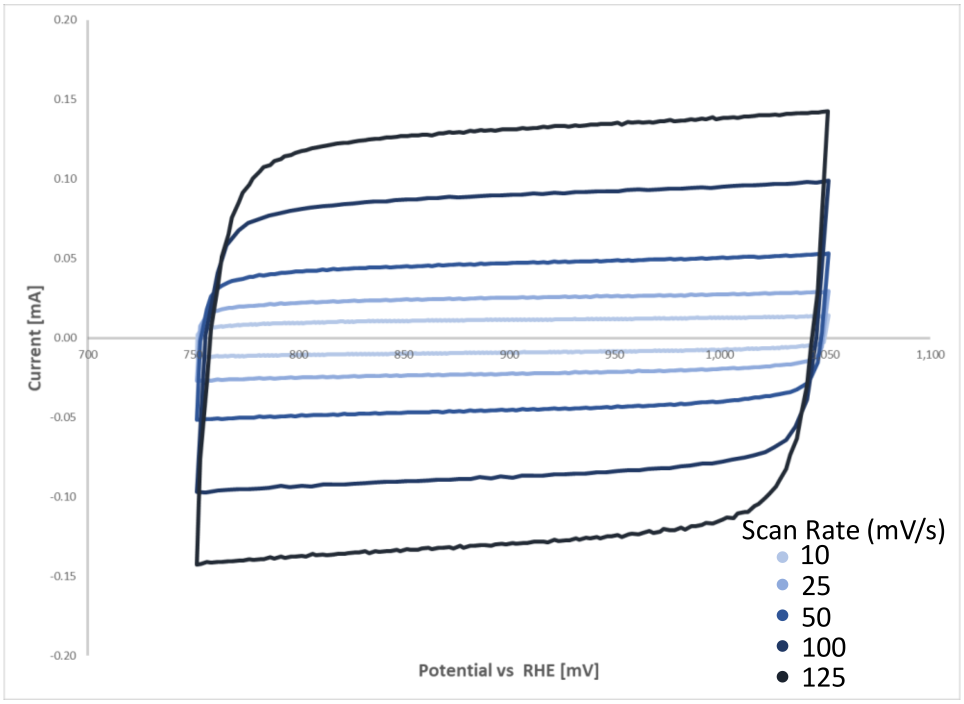

Figure 5-2. Cyclic voltammetry curves measured on porous Nb in the flow cell in N_2 *saturated 100 mM* K_2SO_4 *with no flow at the scan rates indicated.*

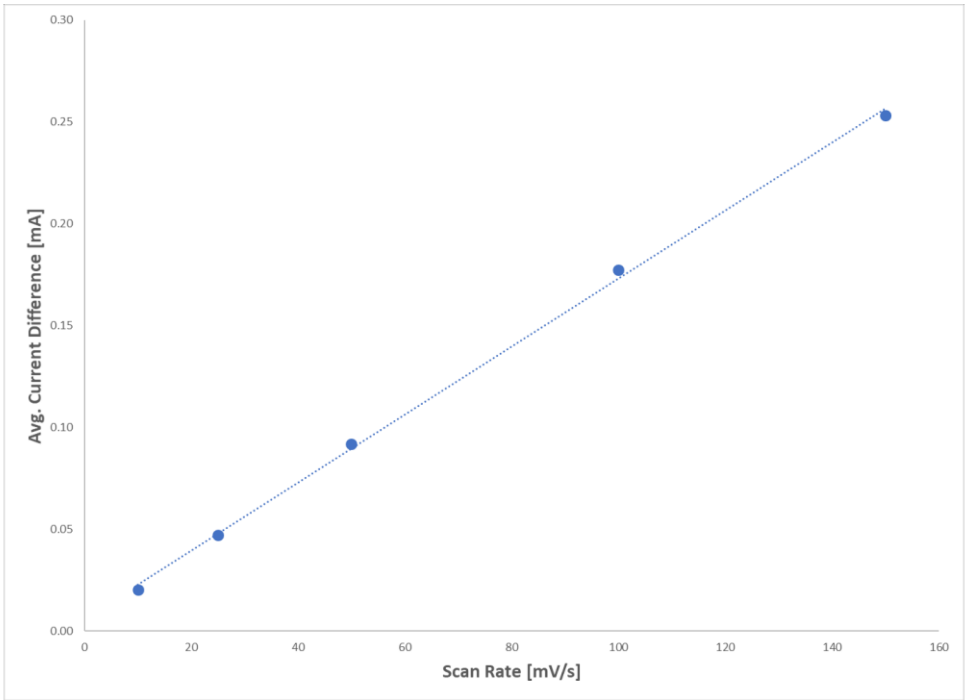

Figure 5-3. Plot of the average current difference between the linear portion of the anodic and cathodic sweeps during cyclic voltammetry measurements from previous figure as a function of the scan rate.

After initial HOR/HER experiments, the Nb was also functionalized with a small amount of Pt following a published solvothermal deposition method in order to improve the HER catalytic activity of the Nb electrode [9]. The porous Nb electrode was lightly etched by immersion in aqua regia at 50 C for several seconds to clean its surfaces. The sample was then rinsed and Pt deposition performed by the following procedure: 16 mL of an electrolyte containing 20 mM potassium citrate (Alfa Aesar) and 20 mM hexachloroplatinic acid (Alfa Aesar) were mixed with 300 mL of 10 mM sodium nitrate (Sigma). The pH of the mixed solution was adjusted to 10 with 100 mM NaOH and the Nb substrates were added. The flask containing the solution was held at 95 to 100 C in an oil bath under reflux conditions in excess of 10 hours, and the solution turned dark brown as noted in the cited reference due to completion of the Pt reduction reaction. The porous Nb sample changed in mass from 0.2270 g prior to Pt deposition to 0.2364 g after deposition. Figure 5-4 shows high magnification SEM micrographs of the composite catalyst (referred to NbPt hereafter). Although Pt couldn’t be conclusively detected by EDS, finely dispersed round particles were present across the surface of the porous Nb that weren’t present on untreated Nb. Visual measurement of several particles indicated the majority of the particles had diameters up to 10 nm. These particle sizes, shapes and distribution were consistent with those synthesized in the referenced article used to determine the deposition process. The Pt surface area of the Nb and Pt composite electrode was calculated by measuring hydrogen UPD in the flow cell in N_2 saturated 1M Na_2SO_4 and determined to be 2.1 times greater than the bare Nb.

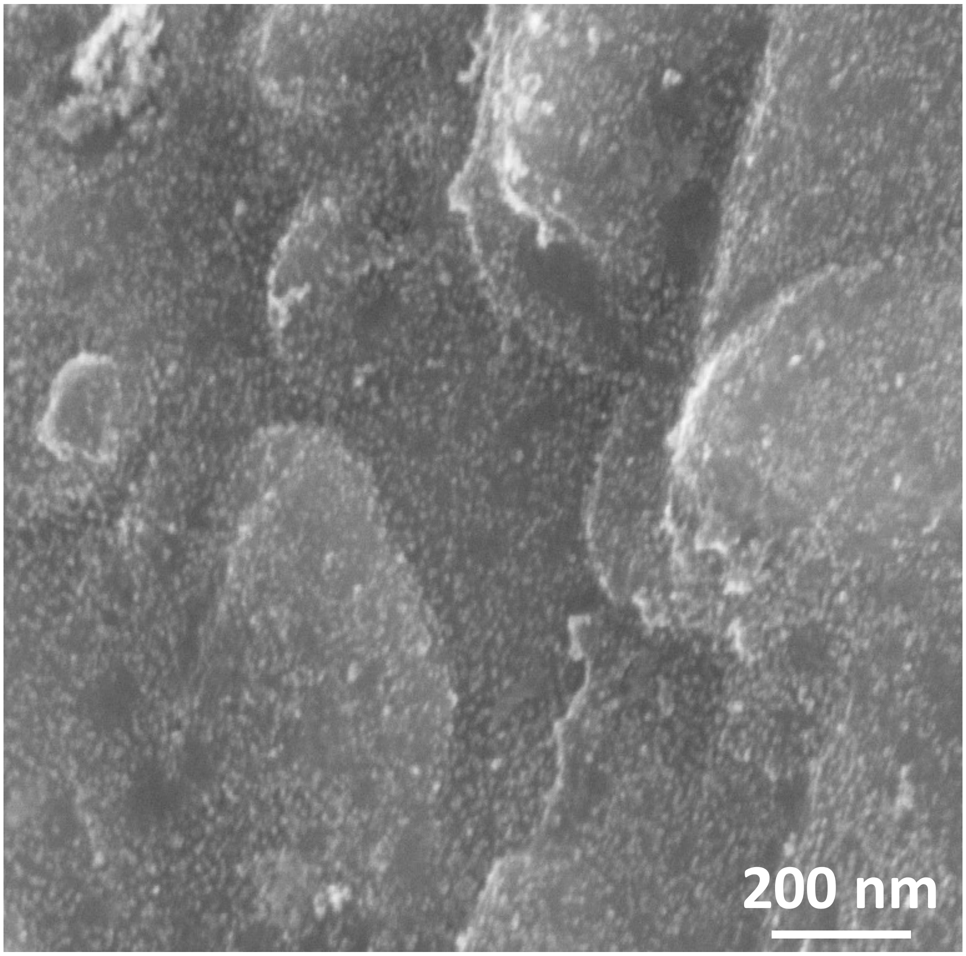

Figure 5-4. SEM micrograph of the surface of an interior Nb ligament after Pt deposition. The ligament was exposed by fracturing the Nb sample immediately prior to imaging. Finely dispersed particles were observed on the surface of the ligament.

A Pt mesh (52 mesh gauze, Sigma Aldrich) HER electrode was tested as a comparison to the NbPt sample. The surface area of a Pt mesh was measured by hydrogen UPD in 100 mM $HClO_4$. In a 6 mm geometric diameter, one mesh was found to have a surface area of 0.635 cm^2, which equated to a roughness factor of 1.75 based on the theoretical surface area of the mesh. In a 6 mm diameter channel, a stack of 6 Pt meshes therefore had 3.8 cm^2 of surface area. The porous Nb electrode with a thickness of 1.04 mm had a surface area of 14.1 cm^2, which was 3.7 times larger than the stack of Pt meshes., while the NbPt sample had a surface area of 29.5 cm^2, which was 7.7 times larger. The pore size of the Pt mesh was approximately 380 microns according to the standard weave dimensions.

Stainless steel screen (type 304, McMaster) with minimum opening of 26 microns was also tested as an HER working electrode. The stainless-steel screen was investigated as an HER catalyst as it had a relatively small opening compared to the Pt mesh with a passive oxide surface (Cr based) similar to Nb.

Results

The ability of the cell to oxidize H_2 was evaluated by performing cyclic voltammetry (CV) with electrolytes purged with both N_2 and H_2. Figure 5-5 shows these results for the cell at a flow rate of 40 mL/min. The curves clearly show the stack of Pt meshes was capable of oxidizing H_2 to protons due to the broad and substantial oxidation peak present from 0 to 1500 mV in the H_2 purged electrolyte. Subsequent data were collected at HOR currents generated within the potential region of H_2 oxidation according to the CV curves.

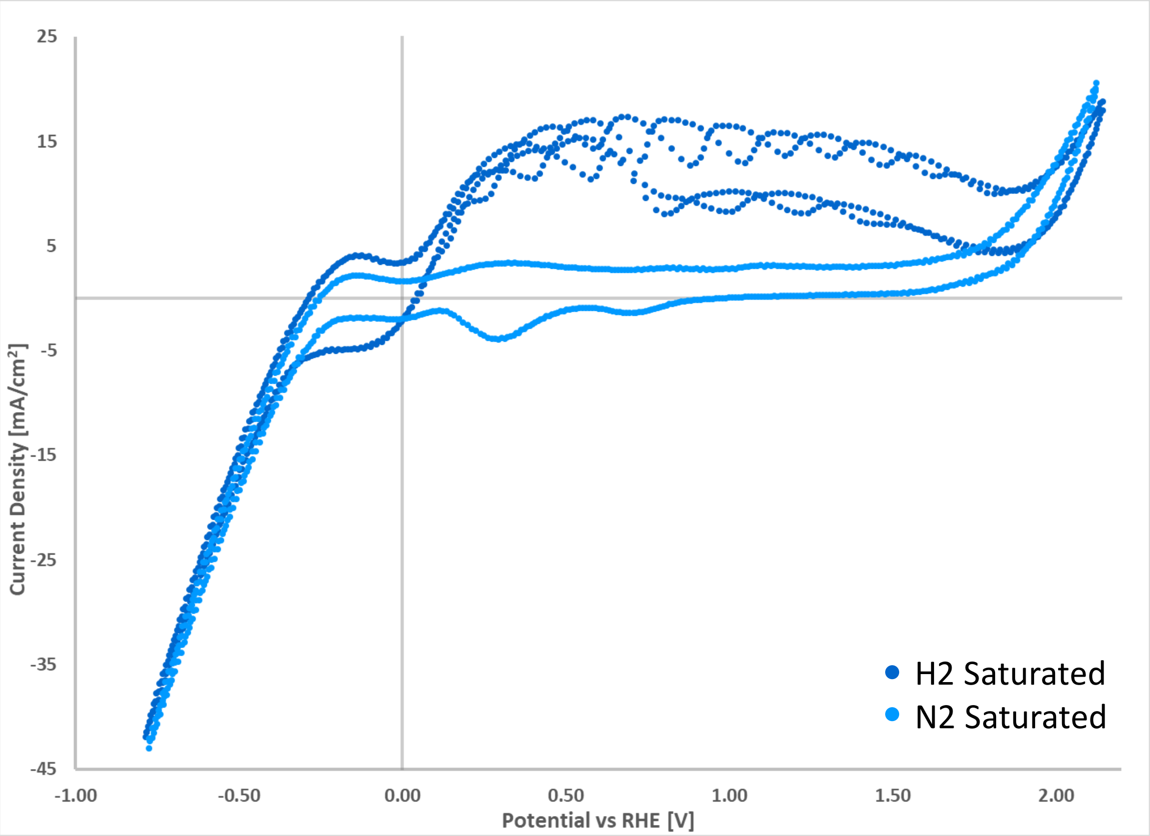

Figure 5-5. Cyclic voltammetry measurements (50 mV/s) on a stack of 4 Pt meshes in the flow cell at flow rate of 40 mL/min in electrolytes purged with H_2 and N_2 as indicated.

HER Catalyst Materials

Figure 5-6 through Figure 5-9 show CV curves obtained from porous Nb, NbPt, Pt mesh (six meshes stacked) and stainless-steel mesh HER electrodes in H_2 saturated 1M Na_2SO_4 electrolyte with various upstream HOR currents. The applied HOR current distinctly affected the HER reduction current generated from protons on the porous Nb and NbPt, while the stainless steel and Pt mesh electrodes responded negligibly in response to upstream HER current in the potential range corresponding to proton reduction. The response of the porous Nb electrodes was apparent around 0 to -500 mV

(Nb electrode) and 0 to -300 mV (NbPt electrode) on both the negative and positive going sweeps. The potential ranges of the observed HER response on the Nb and NbPt electrodes lined up well with the expected potential range for HER via proton reduction.

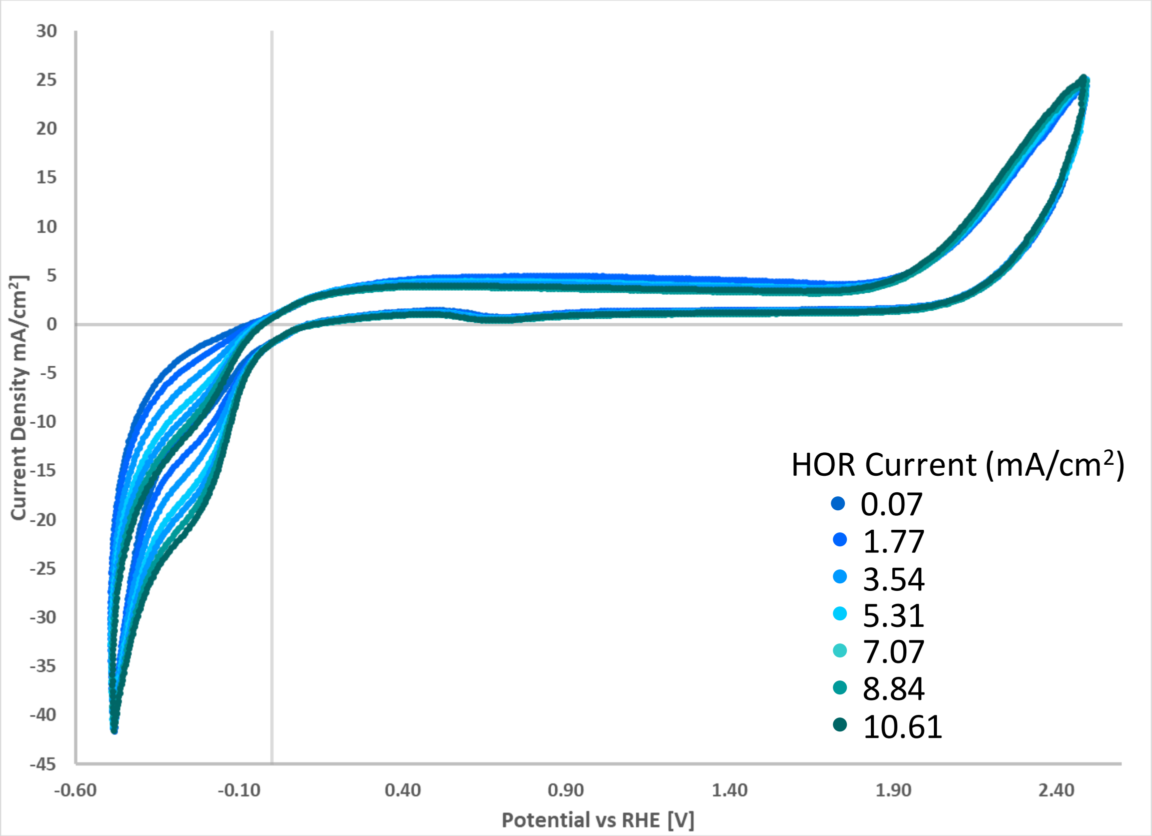

Figure 5-6. Cyclic voltammograms (50 mV/sec) of porous Nb HER working electrode in H_2 saturated 1M Na_2SO_4 with the upstream HOR working electrode operating at the noted current densities.

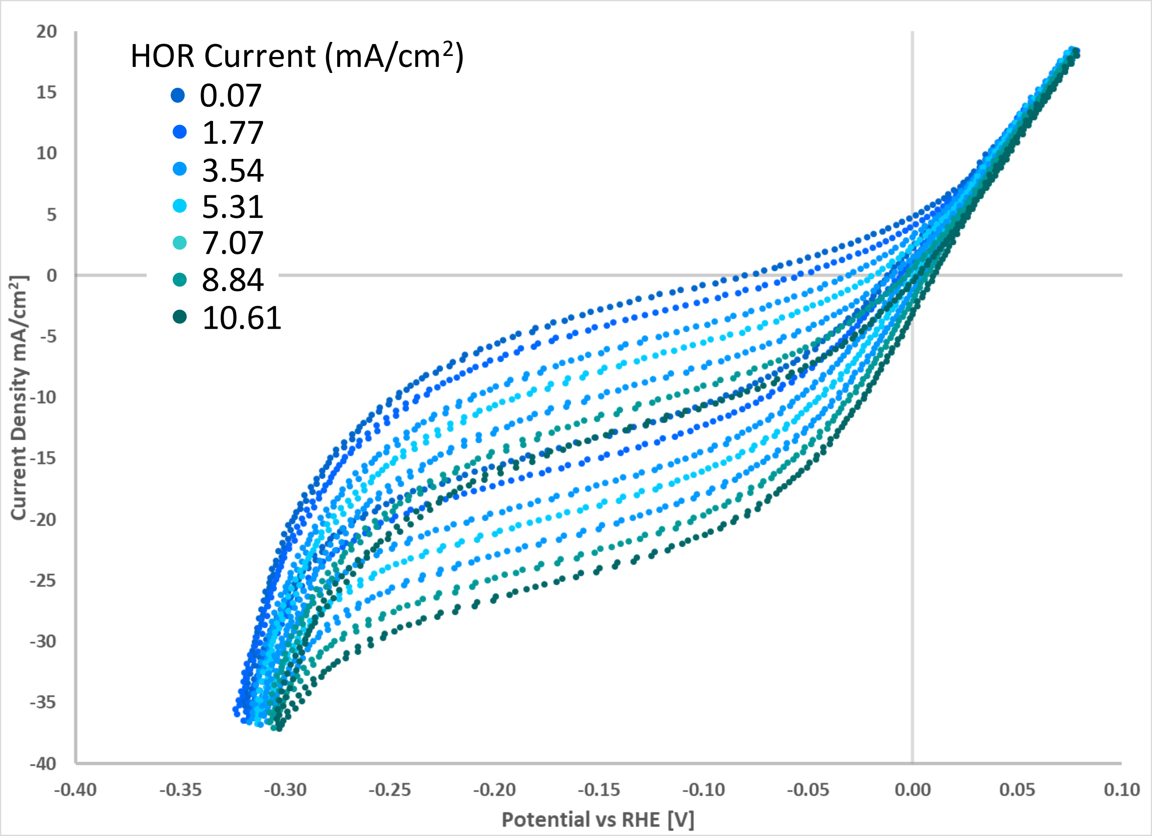

Figure 5-7. Cyclic voltammograms (50 mV/sec) of porous NbPt HER working electrode in H_2 saturated 1M Na_2SO_4 with the upstream HOR working electrode operating at the noted current densities.

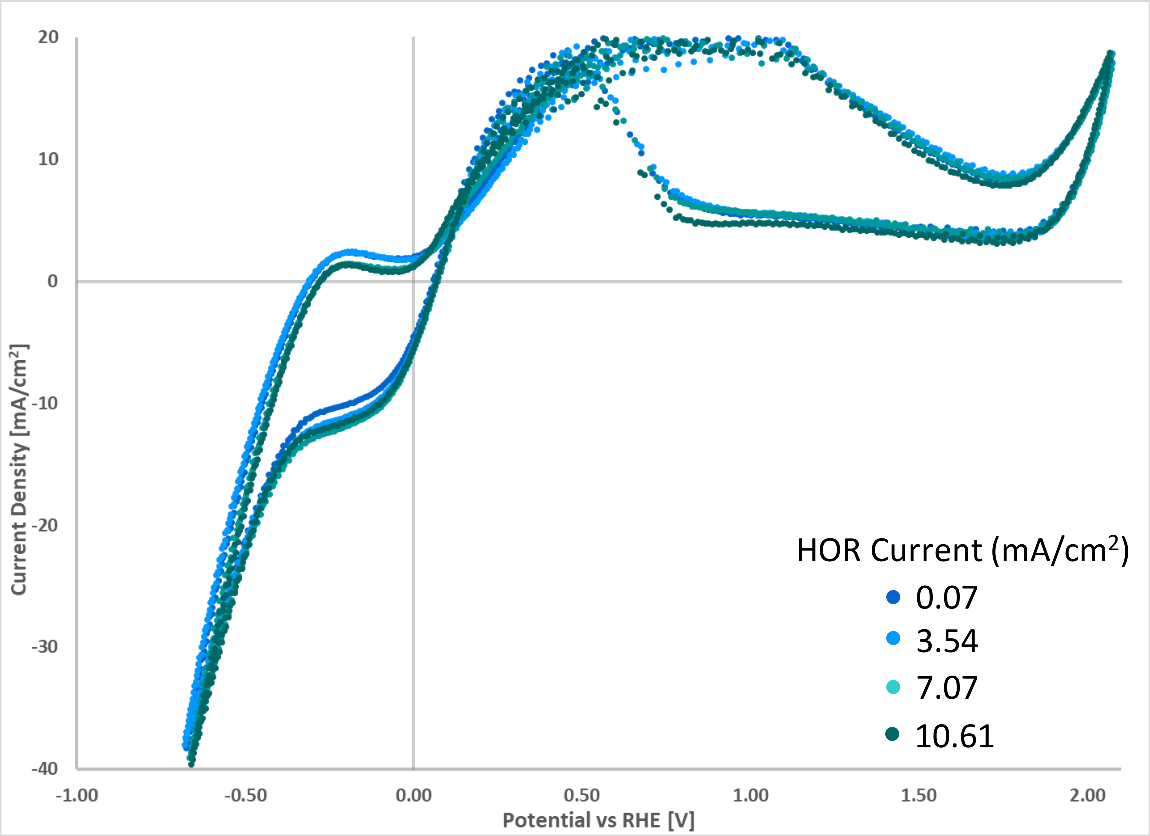

Figure 5-8. Cyclic voltammograms (50 mV/sec, average of 2 CV cycles) of stack of 6 Pt mesh HER working electrode in H_2 saturated 1M Na_2SO_4 with the upstream HOR working electrode operating at the noted current densities.

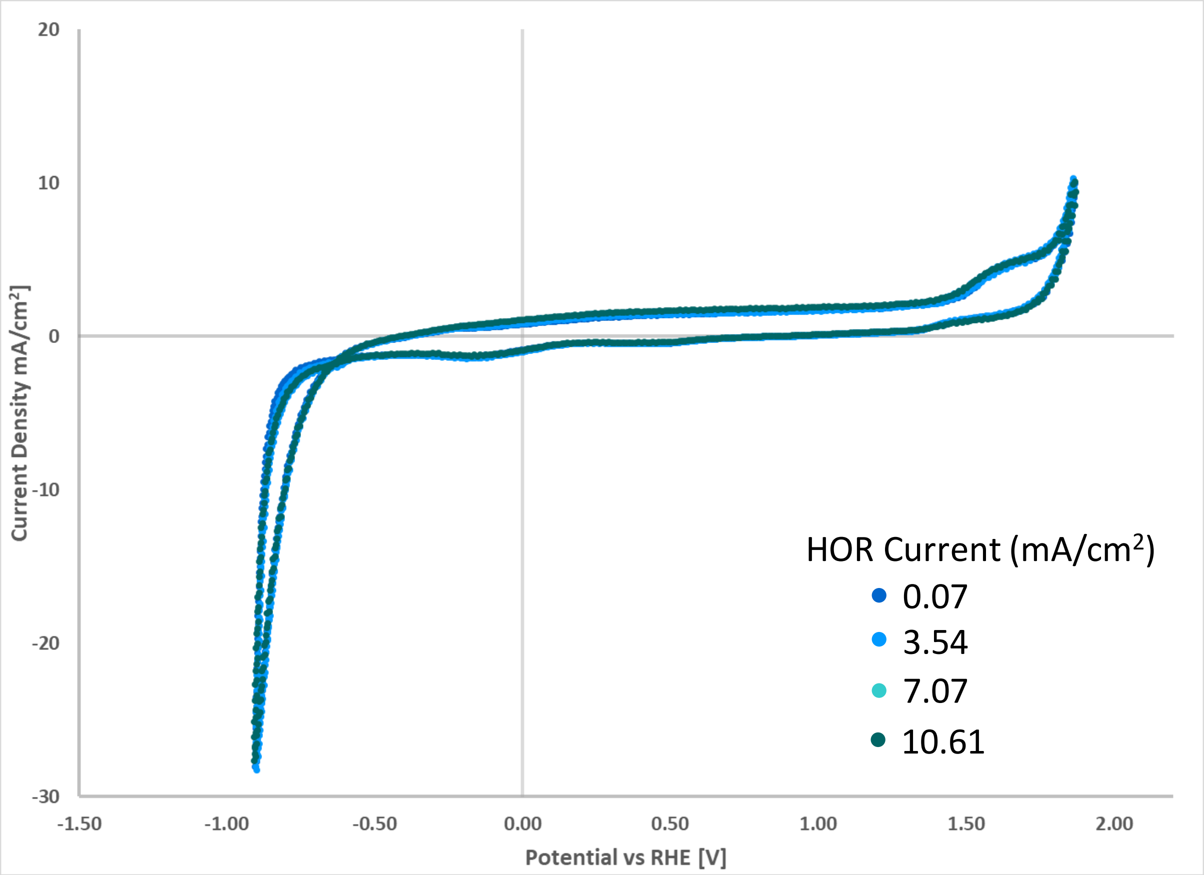

Figure 5-9. Cyclic voltammograms (50 mV/sec) of stainless-steel mesh HER working electrode in H_2 saturated 1M Na_2SO_4 with the upstream HOR working electrode operating at the noted current densities.

To more accurately detail the HOR effects on HER at each electrode, we performed CV measurements at slower scan rates of 5 mV/sec in order to minimize non-Faradaic current effects. Figure 5-10 through Figure 5-13 show the slow CV data for the HER electrodes at various HOR currents. The effects of HOR on HER at the Nb based electrodes were again evident over the entire potential range sampled while the response of the mesh Pt electrodes to upstream HOR was apparent below -400 mV with the stainless-steel electrode showing a small but nearly negligible response to upstream HOR current below -600 mV.

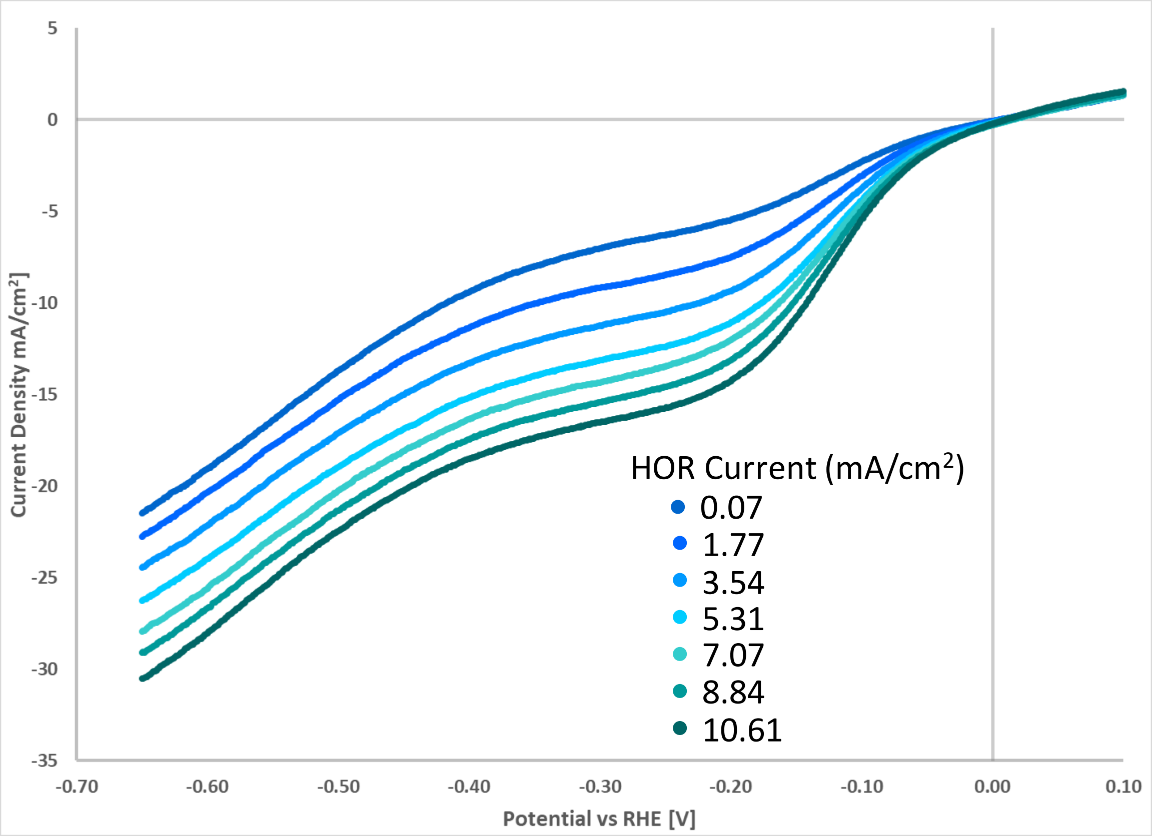

Figure 5-10. Negative going sweep from slow cyclic voltammograms (5 mV/sec) of porous Nb HER working electrode in H_2 *saturated 1M* Na_2SO_4 *with the upstream HOR working electrode operating at the noted current densities. The plotted curves are an average of 4 CV's.*

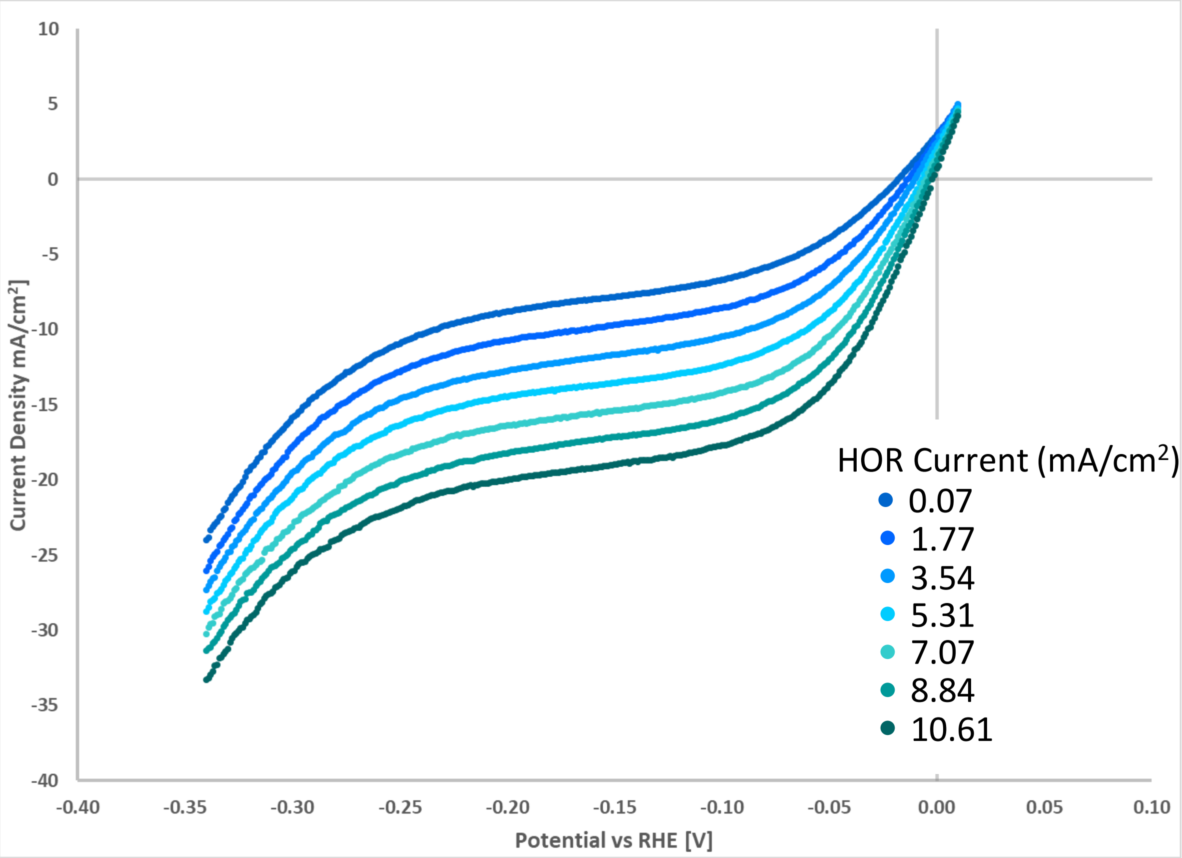

Figure 5-11. Negative going sweep from slow cyclic voltammograms (5 mV/sec) of porous NbPt HER working electrode in H_2 saturated 1M Na_2SO_4 with the upstream HOR working electrode operating at the noted current densities. The plotted curves are an average of 3 CV's.

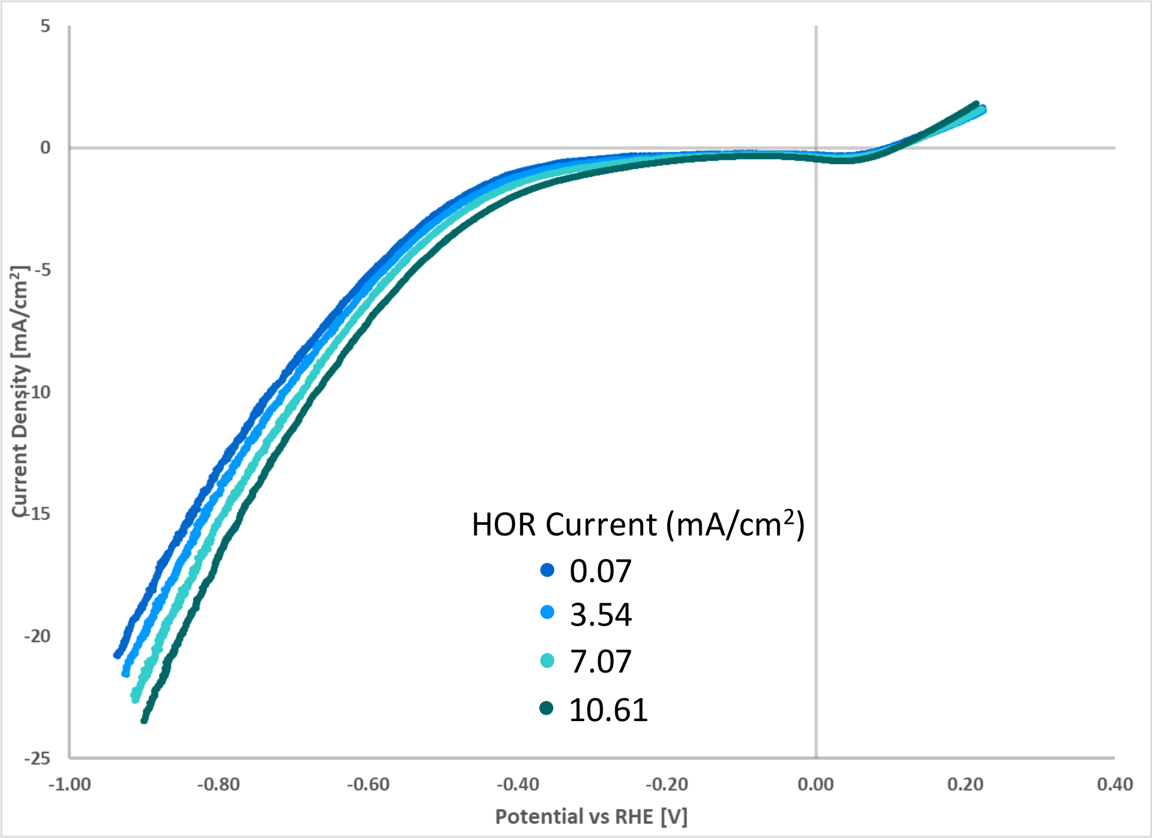

Figure 5-12. Negative going sweep from slow cyclic voltammograms (5 mV/sec) of 6 Pt mesh HER working electrode in H_2 saturated 1M Na_2SO_4 with the upstream HOR working electrode operating at the noted current densities. The plotted curves are an average of 4 CV's.

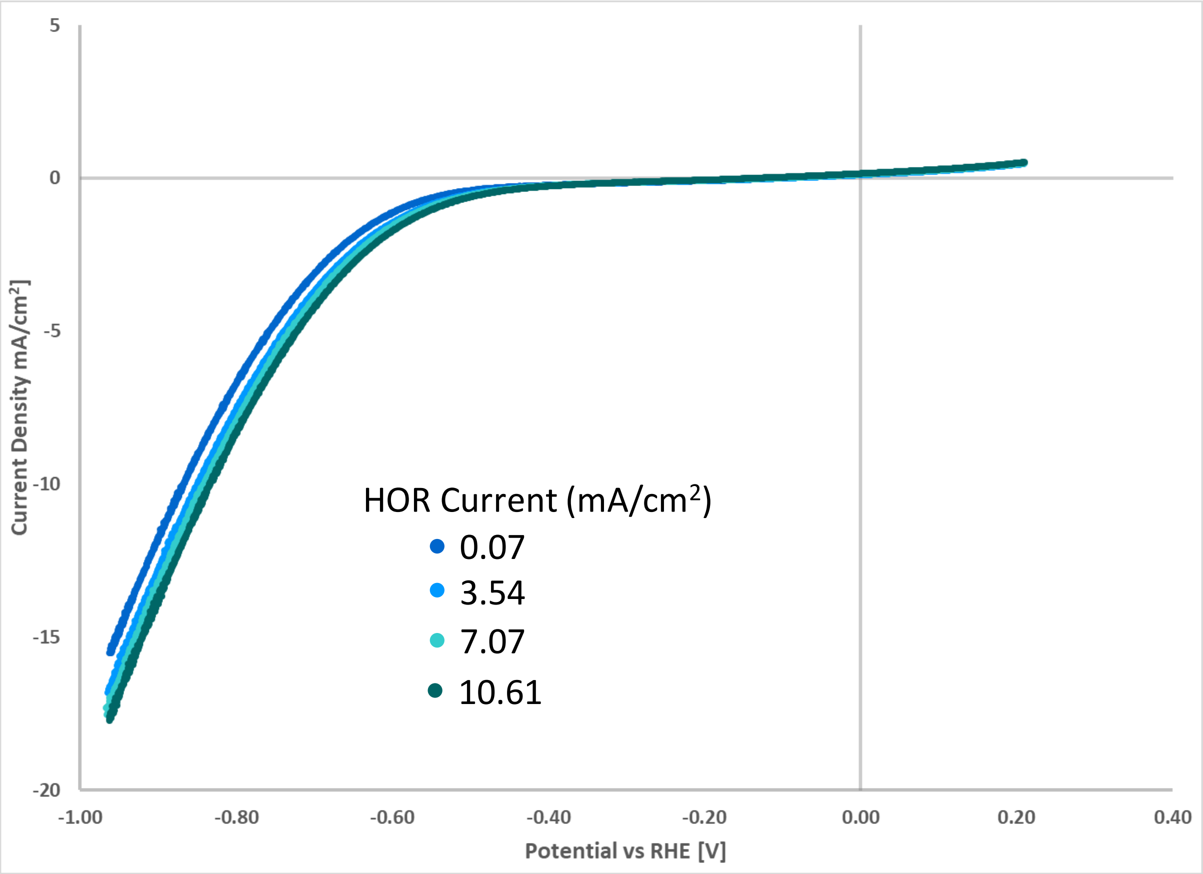

Figure 5-13. Negative going sweep from slow cyclic voltammograms (5 mV/sec) of stainless-steel mesh working electrode in H_2 saturated 1M Na_2SO_4 with the upstream HOR working electrode operating at the noted current densities. The plotted curves are an average of 4 CV's.

The negative going sweeps of the slow CV data were analyzed several methods to characterize the ability of the porous Nb based electrodes to convert the protons created directly upstream back to H_2. First, the excess reductive current was determined by subtracting the background slow CV data generated at an upstream HOR current of 20 µA from the data at the other HOR currents. Figure 5-14 and Figure 5-15 show these data, which clearly indicate that the amount of excess HER current was proportional to the upstream HOR current. The excess current in the proton reduction region was negligible on the mesh electrodes. The conversion efficiency of the Nb electrode (excess reductive current/HOR current upstream) was also calculated and is plotted in Figure 5-16 and Figure 5-17 for the Nb and NbPt electrodes. The efficiency was negligible on the mesh electrodes in comparison to the Nb based electrodes.

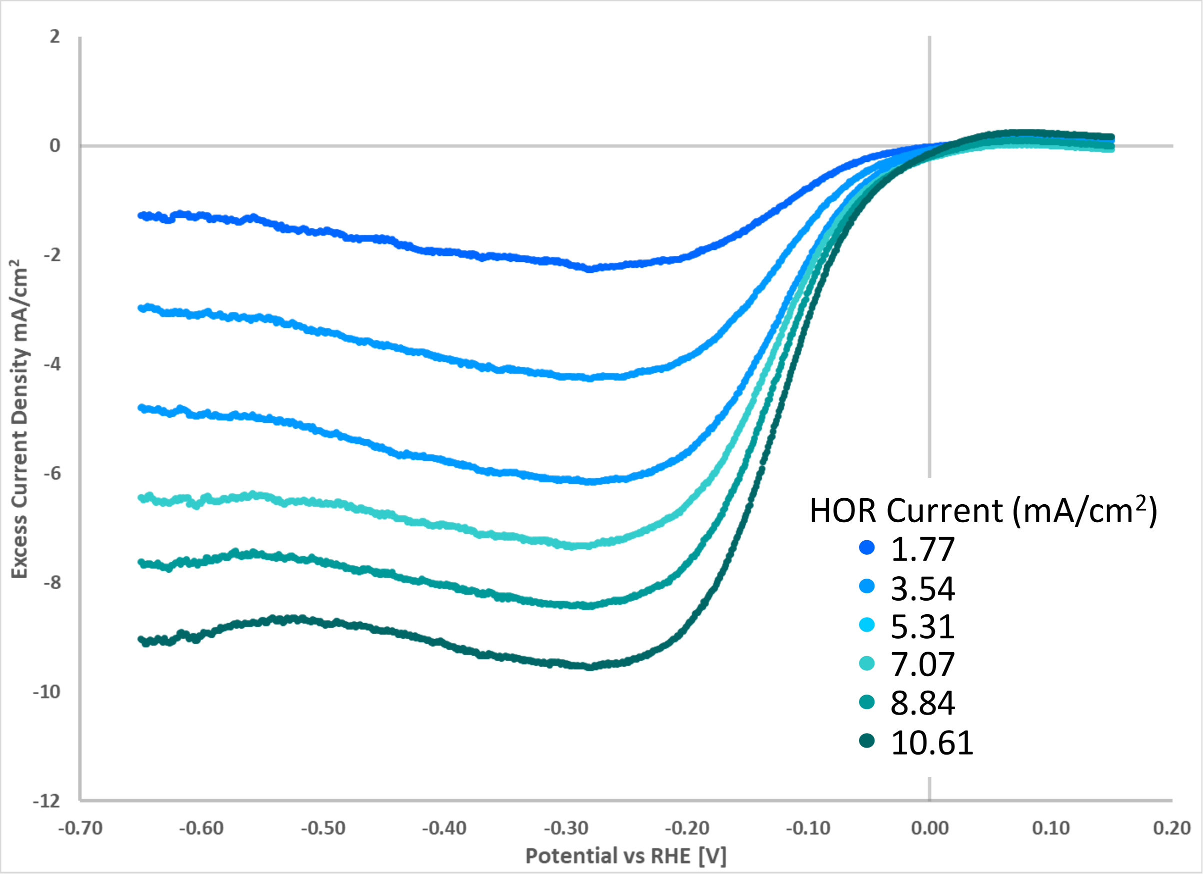

Figure 5-14. The excess HER current density (compared to the curve obtained at negligible applied HOR current density) versus applied potential using the porous Nb working electrode as a function of the noted HOR current densities. These data were calculated from the negative going sweeps of 5 mV/sec CV's in H_2 saturated 1M Na_2SO_4.

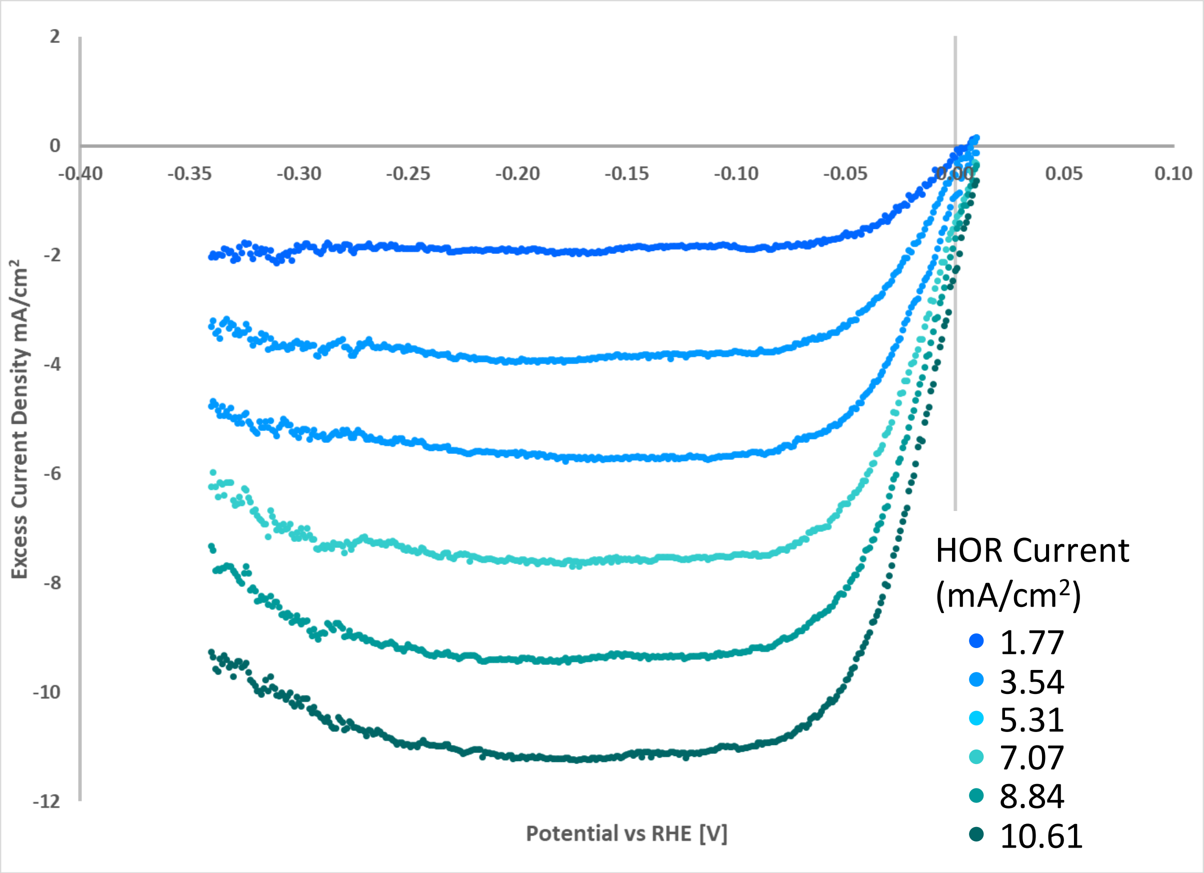

Figure 5-15. The excess HER current density (compared to the curve obtained at negligible applied HOR current density) versus applied potential using the porous NbPt working electrode as a function of the noted HOR current densities. These data were calculated from the negative going sweeps of 5 mV/sec CV's in H_2 saturated 1M Na_2SO_4.

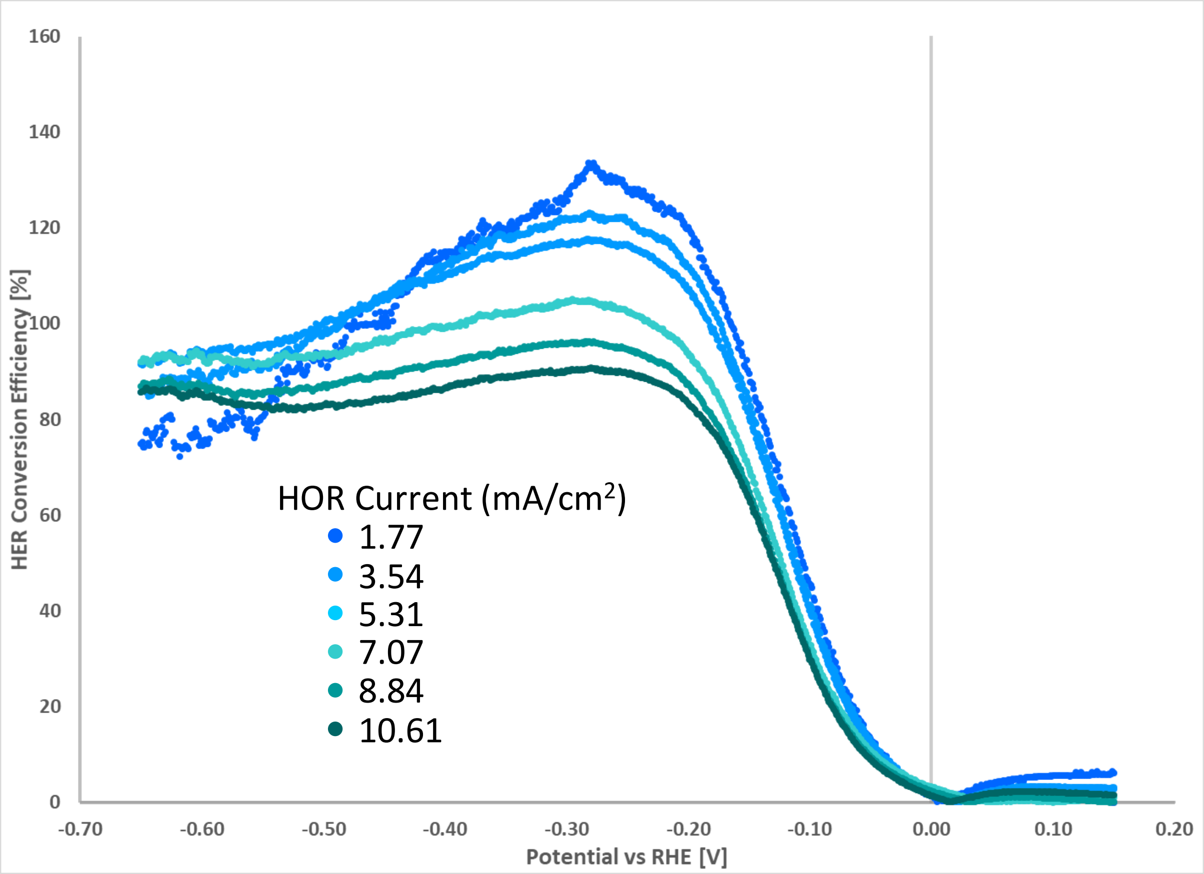

Figure 5-16. The HOR to HER conversion efficiency versus applied potential using the porous Nb working electrode as a function of the noted HOR current densities. These data were calculated from the excess current densities of 5 mV/sec CV's in H_2 saturated 1M Na_2SO_4.

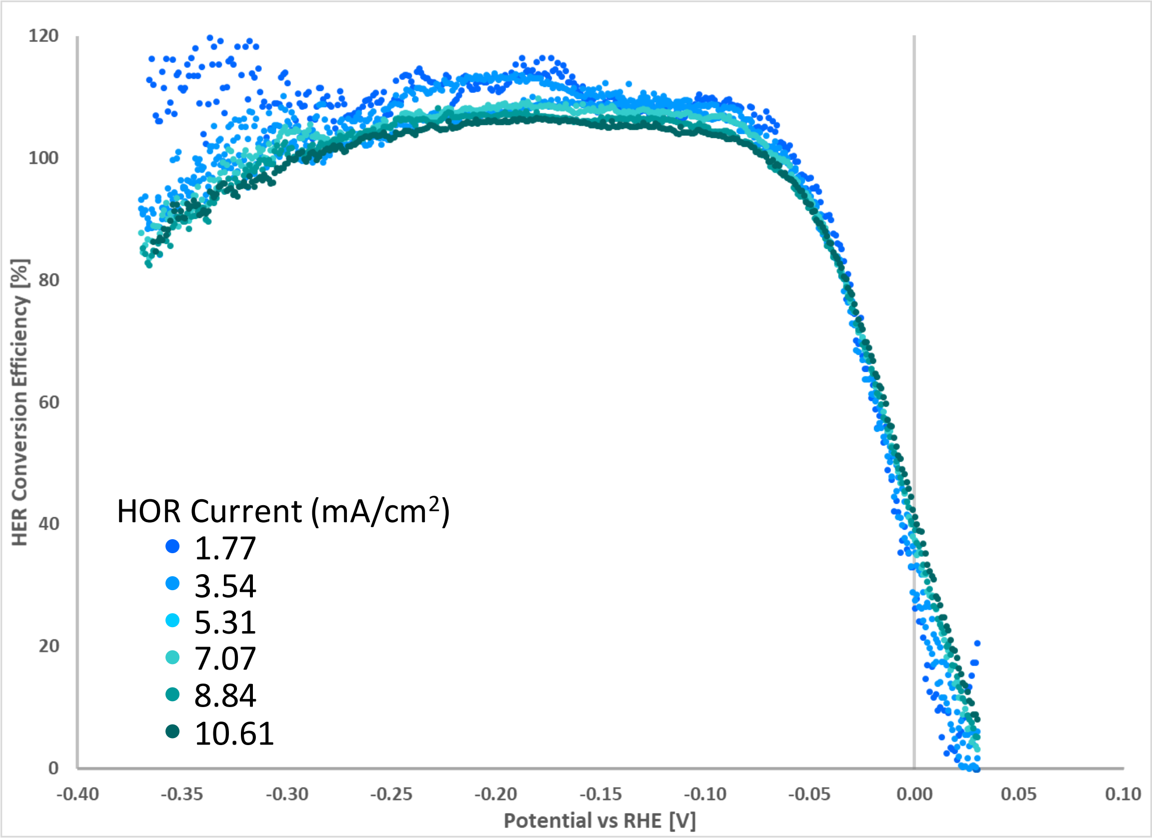

Figure 5-17. The HOR to HER conversion efficiency versus applied potential using the porous NbPt working electrode as a function of the noted HOR current densities. These data were calculated from the excess current densities of 5 mV/sec CV's in H_2 *saturated 1M* Na_2SO_4.

Figure 5-16 and Figure 5-17 show the calculated conversion efficiency of the cell peaked at approximately 80 to 130% for the Nb electrode between -100 and -400 mV (the upper conversion limit being an impossibly large value attributed to the nature of the bare Nb catalyst which we discuss below) and remained nearly constant around 100% between -50 and -300 mV for the NbPt electrode, while the Pt and stainless-steel mesh electrodes converted protons to H_2 at negligible efficiency in comparison over the same potential range. The apparent HER conversion efficiency of the Nb electrode decreased with increasing HOR current as shown in Figure 5-16.

Figure 5-18 and Figure 5-19 show Tafel plots generated from Figure 5-10 and Figure 5-11 to aid in detailed analysis of these electrode characteristics.

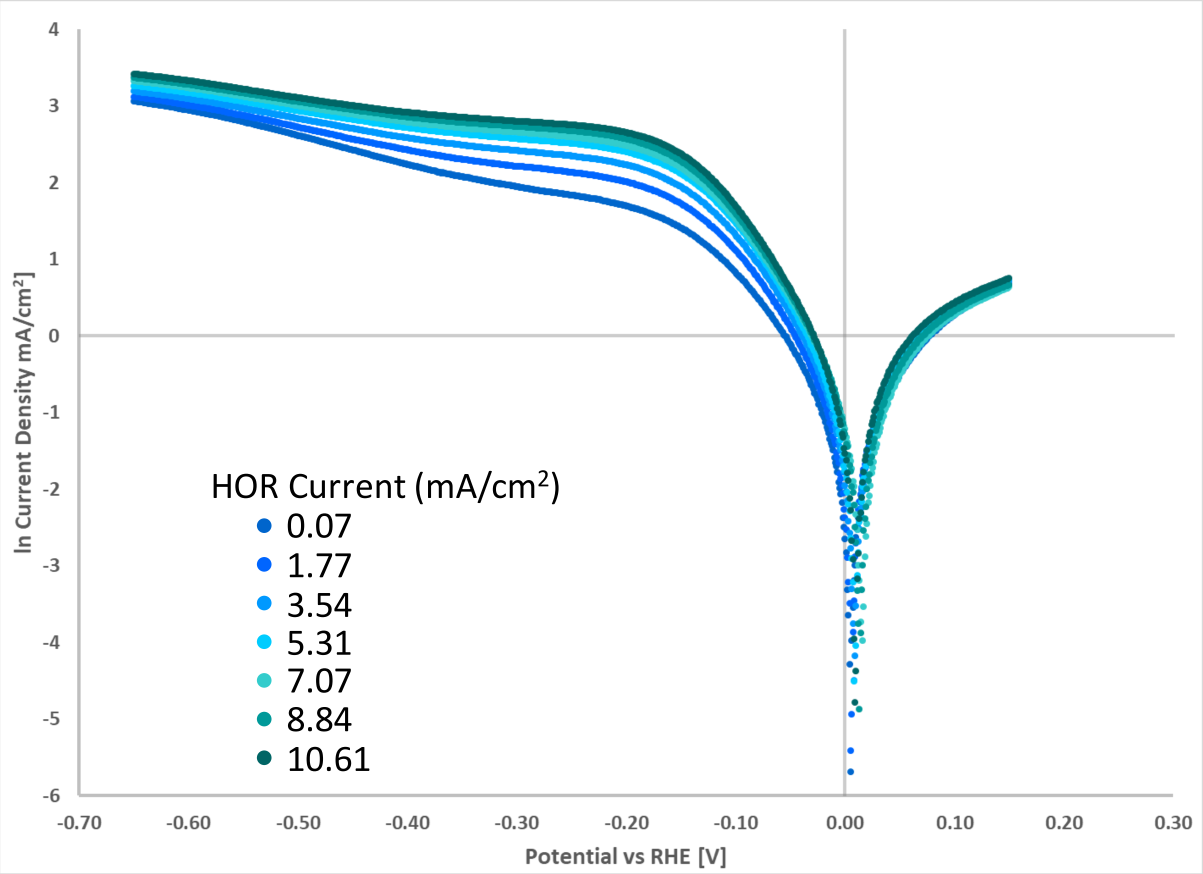

Figure 5-18. Tafel plot of negative going sweep of 5 mV/sec CV of Nb in H_2 *saturated 1M* Na_2SO_4*.*

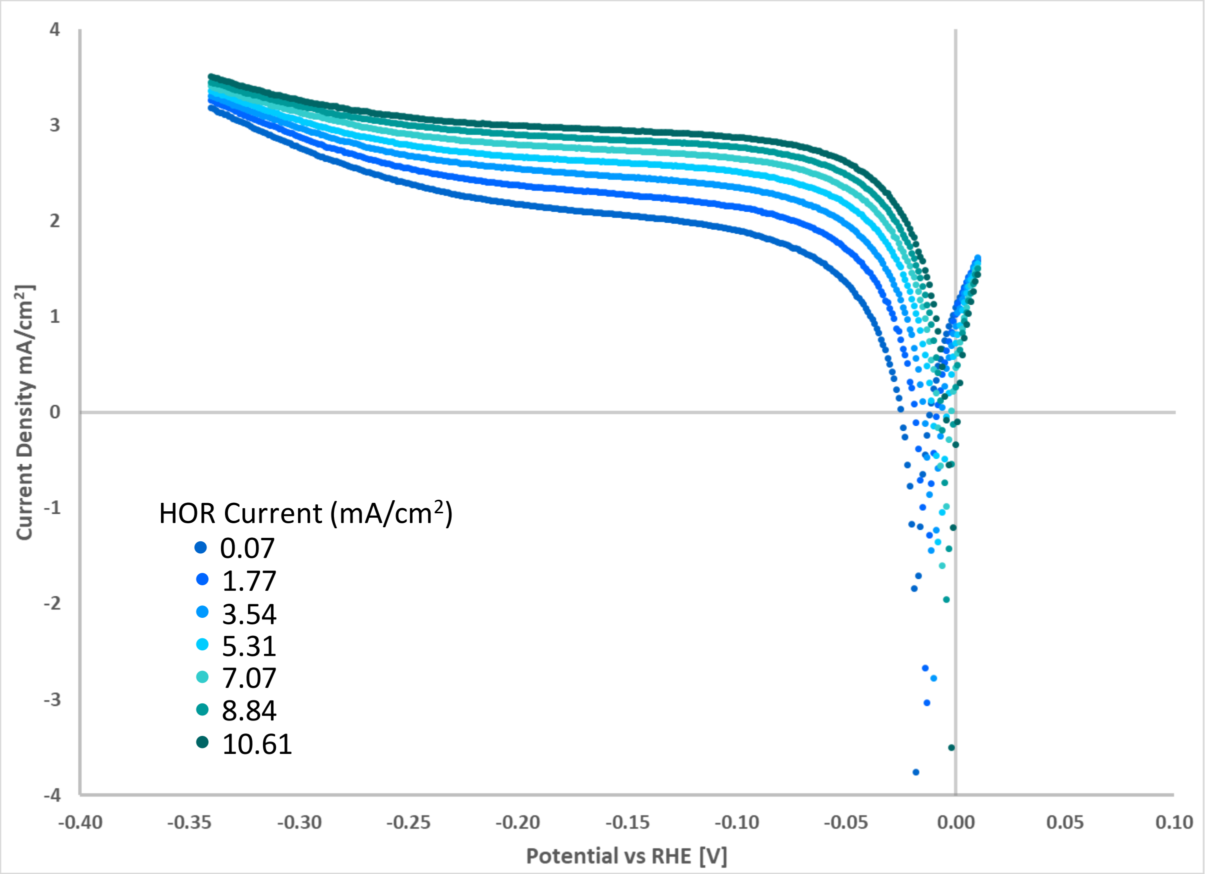

Figure 5-19. Tafel plot of negative going sweep of 5 mV/sec CV of NbPt in H_2 *saturated 1M* Na_2SO_4*.*

Surface Area Effects

We further examined the effects of active surface on the HER conversion efficiency by characterizing Pt mesh electrodes with a three Pt mesh as the active HER catalyst against those with six meshes shown in detail above. The HER conversion efficiency was minimal, but the H_2 oxidative current (in the range of 100 to 1500 mV) was approximately 10 mA/cm² on the three-mesh electrode and 15 mA/cm² on the six-mesh electrode as shown in Figure 5-20.

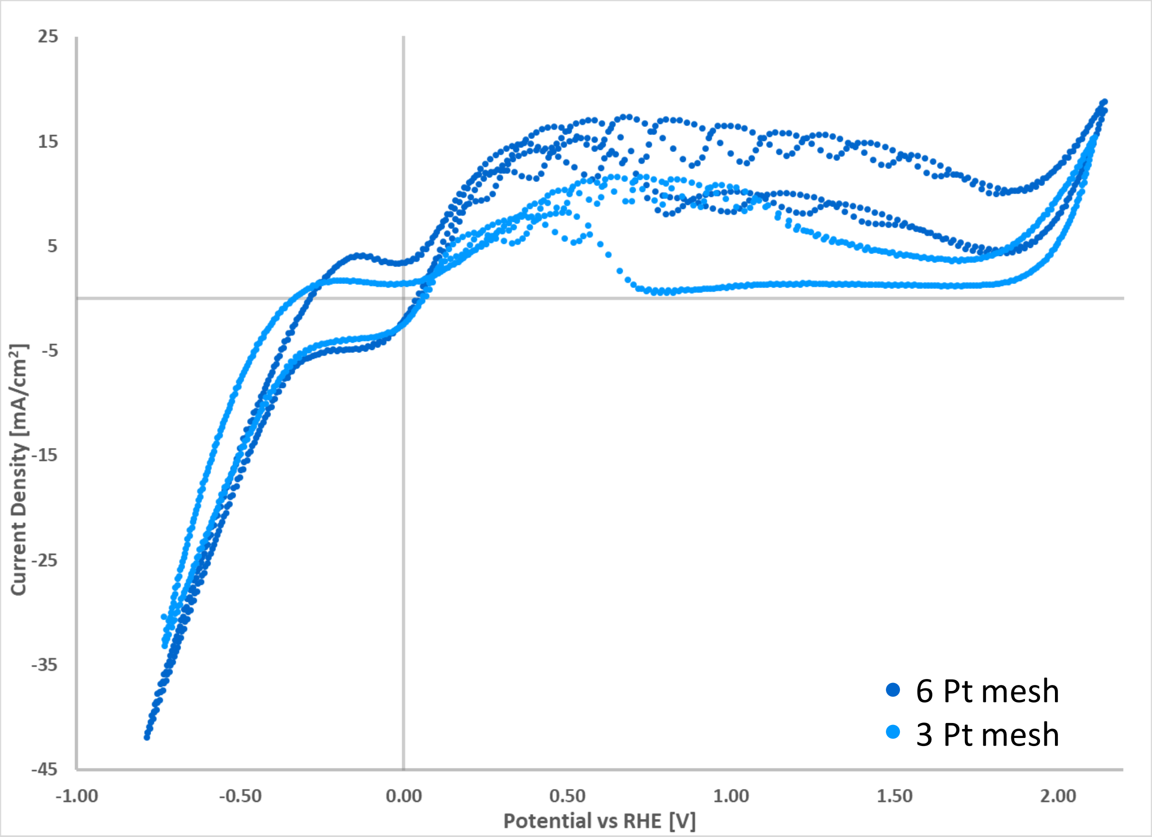

Figure 5-20. Cyclic voltammograms (scan rate of 50 mV/sec) of 3 and 6 mesh Pt electrodes in H_2 saturated 1M Na_2SO_4.

HOR on NbPt

Figure 5-21 shows CV measurements of the NbPt electrode in H_2 and N_2 saturated electrolytes which were performed to confirm the cause of the large oxidative peak positive of 0 mV vs RHE on the NbPt electrode was due to HOR. The large oxidation peak positive of 0 mV was present only under H_2 saturated conditions, proving that this peak corresponded to direct oxidation of H_2.

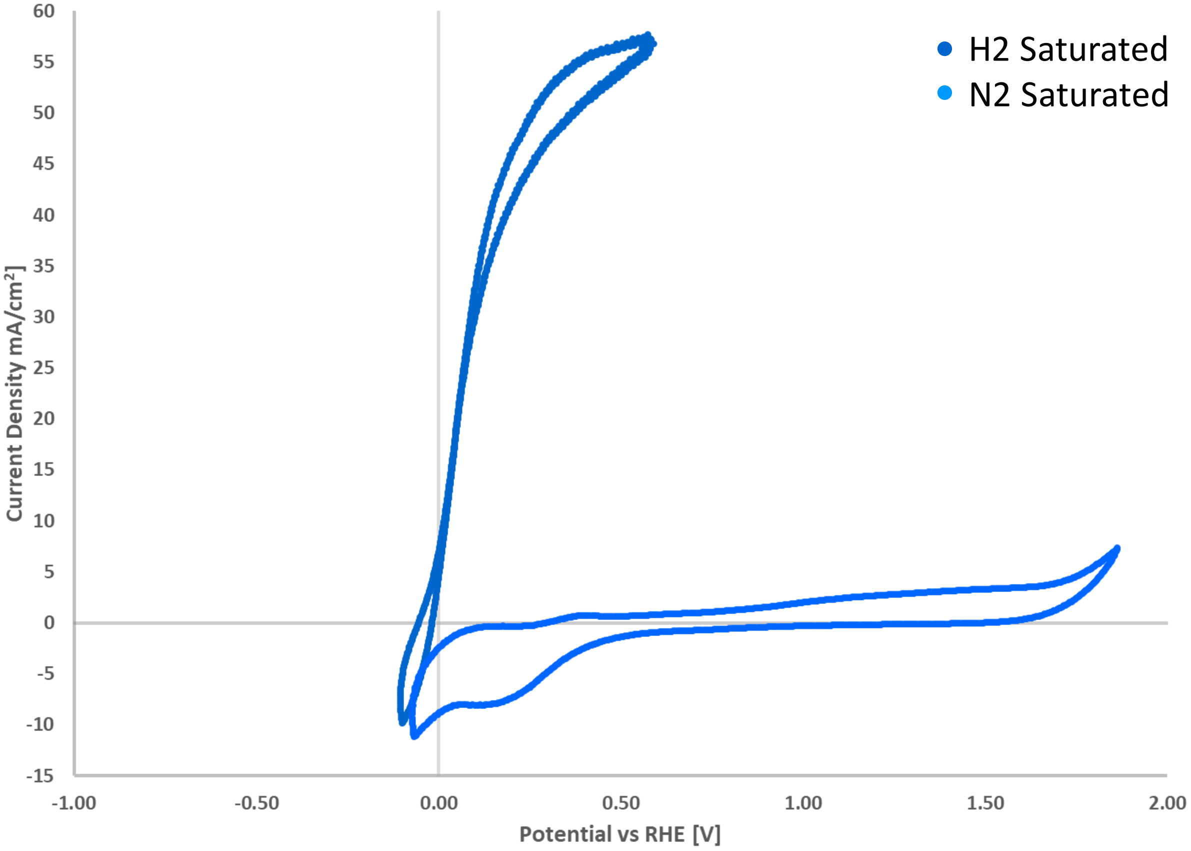

Figure 5-21. Cyclic voltammetry measurement from NbPt electrode in H_2 and N_2 saturated 1M Na_2SO_4 at 50 mV/s scan rate and 40 mL/min flow rate.

Discussion

The primary aim of performing sequential HOR/HER in the flow cells was to determine whether sequential electrolysis employing porous electrodes is a feasible approach to electrochemically binding protons derived from H_2 (or perhaps another fuel source such as simple alkanes or alcohols) to another atom such as carbon or nitrogen in an efficient and well-controlled reaction. If such a sequential approach were possible, it would provide an additional degree of control from a conventional electrochemical reaction in a single cell. The tests clearly showed it was possible to oxidize H_2 and subsequently reduce the generated protons at high efficiency with a porous electrode in a flow cell if the HER electrode met certain characteristics.

Proton Reduction

The onset of cathodic current waves near 0 mV versus RHE (the defined equilibrium potential for proton reduction) were confirmed as a proton reduction reaction based on similarities to other studies. Another study on HER/HOR in weakly acidic electrolytes on Pt electrocatalysts also predicted similar polarization curves to the slow CV data obtained here [10]. This study predicted two characteristic reduction waves corresponding to proton reduction near 0 mV vs RHE and H_2O reduction onset at approximately -400 mV vs RHE. We observed onset of proton reduction nearly at 0 mV on the NbPt samples and approximately 100 mV positive on the Pt mesh. However, it is important to note that the MSE reference was calibrated to the RHE scale in a conventional manner while the working HER electrodes were immersed in flowing electrolyte (where increased flow rate caused a positive shift in the open circuit potential of Pt mesh by ~ 60 mV as shown in the previous chapter) and without H_2 bubbling directly adjacent to the HER working electrodes as done during calibration, so positive deviations from 0 mV RHE equilibrium potential seemed reasonable for the pure Pt mesh given the operating conditions of the flow cell.

There are few previous studies of Nb as an HER catalyst in acidic electrolytes, however one detailed study of HER in 0.145 M HCl on planar Nb electrodes showed onset of proton reduction at a cathodic overpotential of approximately 80 mV, similar to the overpotential range (relative to the NbPt sample reductive wave) where we observe the onset of a reductive wave that scaled with HOR current [11].

Reduction of protons occurred over a limited potential range in the weakly acidic electrolyte until the onset of a second reductive wave, which corresponded to reduction of H_2O to H_2 and OH^-. The proton reduction range spanned approximately 0 to -250 mV vs RHE on Pt containing electrodes, 0 to -400 mV on the Nb electrode and 0 to -600 mV on the stainless-steel electrode. In further references to proton reduction below these potential ranges are implied. The voltammetry characteristics of the various porous electrodes proved that the Nb based electrodes were efficient for proton reduction from H_2 oxidized upstream.

Before discussing proton reduction in detail, it is important to note that the Pt meshes did exhibit apparent small but measurable HER conversion efficiencies at large cathodic overpotentials as shown in Figure 5-12. However, the excess HER current generated at these overpotentials was attributed to reduction of H_2O to H_2 rather than direct conversion of protons to H_2. Since Pt is among the most efficient HER catalysts for proton reduction (and is known to be more efficient than Nb) and requires minimal overpotential for HER, we expect that if the Pt meshes were efficiently converting HOR generated protons to H_2 there would have been significant excess current at small overpotentials just beyond 0 mV vs RHE as was observed on Nb based electrodes. Equation 5.2 shows the electrochemical reaction for HER via H_2O reduction. The hydroxyl concentration (and hence the pH of the electrolyte has a direct impact on equilibrium potential of the H_2O reduction reaction, and a decrease in pH would be predicted to shift the onset potential of H_2O reduction in a positive direction as we observed.

$$2H_2O + 2e^- \rightarrow H_2 + 2OH^- \qquad 5.2$$

However, the same reasoning described in the previous paragraph for water reduction could be applied to direct proton reduction on the Pt mesh, and since we didn’t observe measurable differences in proton reduction on the mesh electrodes it was likely that the choice of the offset potential of the MSE reference to the RHE scale was responsible for the apparent effect of HOR current density on H_2O reduction. The offset of the MSE reference electrode relative to the RHE was measured under standard conditions outside of the flow cell, and this offset value was used to shift all voltammetry data to the RHE potential scale independent of the applied HOR current in the operating flow cell. Any applied HOR current corresponding to oxidation of H_2 at the HOR working electrode caused a corresponding positive shift in the RHE potential at the HER reference electrode due to the corresponding decrease in the pH of the electrolyte.

Since this MSE to RHE potential shift due to upstream HOR wasn't accounted for, due to the difficulty of measuring such an effect accurately in the flow cell, there is a strong likelihood that the observed positive potential shift in the onset of H_2O reduction on the HER electrodes with increasing HOR current in the voltammetry data was an artefact of not accounting for the change in the MSE to RHE potential offset caused by the HOR current. There was theoretical shift in the MSE to RHE potential of approximately 50 mV in the positive direction between HOR current densities of 0 and 10.61 mA/cm^2. Accurately accounting for such potential shift effects in the voltammetry data may have more closely aligned the H_2O reduction waves while decreasing potential range where HER conversion efficiencies due to proton reduction were observed. In either calculation method for the RHE offset, the potential shift wasn't materially important when analyzing the Nb based electrodes as we observed large excess reductive current in the diffusion limited potential range over several hundreds of mV that could not be explained as an artefact of the MSE to RHE potential offset used.

HER Conversion Efficiency

The CV data from the various HER electrodes show clear differences in the behavior of each HER working electrode in the potential range of proton reduction to H_2. The choice of electrode materials allowed us to determine the cause of the enhanced HER conversion efficiency through direct comparison between the Nb, NbPt and Pt mesh electrodes.

The active surface area of the Nb and NbPt electrodes was ~3.5x and ~8x greater than the stack of 6 Pt mesh electrodes. Despite the marginal decrease in surface area, the diffusion limited current for in the potential range of proton reduction in the Pt mesh was significantly less (~25x) than that of the Nb based catalysts. This discrepancy in the amount of diffusion limited proton reduction current compared to the surface area differences between the Pt meshes and the Nb based samples paired with the complete lack of a response of measurable significance of the mesh electrodes in the potential range of proton reduction to upstream HOR immediately suggested that the geometry of the HER electrodes was the primary factor determining HER conversion efficiency rather than the choice of catalyst material.

If the catalyst material were the defining characteristic determining HER conversion efficiency, we would have expected to observe the measurable conversion efficiency on the Pt mesh even with the moderate differences in surface area due to the large relative HER activity on Pt compared to Nb that was well demonstrated by the differences in the Nb and NbPt electrodes.

The results present match well with previous research and theory on porous electrodes flow cell environments, much of which was initially explored and discovered in the 1970's and 80's [12]–[22]. This research showed both theoretically and experimentally that the geometric characteristics of a porous electrode in a flowing electrolyte were the primary factor determining the limiting current and conversion efficiency possible for a particular electrochemical reaction. The theoretical treatments generally assume that the delivery of reactants to the porous electrode surface are governed by diffusional mass transfer radial to the flow direction in the pore where the time, t, for a given reactant with a given diffusivity, D, to diffuse a specific length, r, is approximated by the well-known relationship shown in Equation 5.3 [12].

$$t \approx \frac{r^2}{2D} \tag{5.3}$$

The velocity of the reactant species along the flow direction, v, through the porous electrode can be calculated from the volumetric flow rate, y, and the total cross section of the porosity, a, according to Equation 5.4.

$$v = \frac{y}{a} \tag{5.4}$$

Therefore, the total time a reactant species resides in the porous electrode can determined by dividing its thickness, x, along the flow direction by the velocity of the reactant species along the flow direction. If the time to radially diffuse to the electrode surface is less than the time to pass through the electrode due to the forced flow, then it is expected that the reactant will react (given sufficient overpotential for the given electrochemical reaction). Equating 5.3 to the time to flow through the electrode yields the condition for total conversion of the reactant. The ability of a porous electrode to convert reactants to products can then be expressed as a figure of merit, α, as shown in Equation 5.5 [22].

$$\alpha = \frac{vr^2}{2Dx} \tag{5.5}$$

When α is significantly less than one, complete reaction of all reactants is expected, and for α greater than one partial reaction of the reactants is expected with greater values of α leading to decreasing conversion of the reactants. Experimental work has determined that the limit of complete conversion tends to be for a values less than approximately 0.6 for various reduction reactions [12], [22]. We calculated α for the various HER working electrodes using the radius of the pores or half the mesh opening for r, an estimated diffusivity of 10^{-5} cm^2/s, appropriate thickness from physical measurements or calculations based of wire thickness for stacked mesh, and area porosity based off measurements or theoretical mesh dimensions [23]. Table 5-1 shows the calculated α values for each electrode.

Table 5-1. Calculated characteristics of HER working electrodes.

HER Electrode	**r [cm]**	**x [cm]**	**a**	**α**
Nb, NbPt	0.0005	0.104	0.5	0.57
6 Pt Mesh	0.019	0.06	0.63	1125
St-St Mesh	0.0013	0.0045	0.6	73

The data in Table 5-1 give a clear explanation for the differences in the HER conversion efficiencies of the Nb based electrodes in comparison to the mesh electrodes. The α value of the Nb electrodes is slightly less than 0.6 which was the limit for complete conversion in previous studies as we also observed for HER efficiency. On the other hand, the mesh electrodes had α values well in excess of 1 suggesting that complete conversion was not possible (as observed), and we would have needed up to orders of magnitude more meshes stacked to achieve similar results to the Nb based samples. Further, the large magnitude of the α values for these electrodes also suggest that we should have observed negligible HER conversion efficiency as was found. This predicted minimal conversion efficiency explained why we observed negligible change in the diffusion limited HER current density on the meshes. The current we did measure in the proton reduction potential ranges was the background reductive current and the additional protons generated upstream simply were not reduced at all when passing through the meshes at the flow rate used.

The figure of merit for the Nb based electrodes also might underestimate the ability of these electrodes to convert protons to H_2. The calculation and model used assume electrolyte flow through straight pores of invariant radius, while the Nb had a highly tortuous open pore structure of varying diameter which lengthened the path through the electrode and also affected electrolyte flow characteristics. The decrease in the figure of merit by lengthening of the electrolyte path with a tortuous porous electrode has predicted in flow cell electrolysis with porous electrodes [22]. Flow of the electrolyte around a curved path of varying diameter could have induced additional convective mixing and aided diffusion in mass transport rates at the electrode surface [24]. Inducing these effects of the tortuous nature of the pores would decrease the value of the figure of merit for the Nb electrodes as calculated previously, thereby increasing its ability to reduce protons.

In contrast to HER, we did observe difference in HOR current at the Pt mesh electrodes as shown in Figure 5-20 based on electrode surface area. The 6 mesh Pt electrode oxidized more H_2 in the electrolyte than the 3 mesh Pt electrode. While the observed current density due to H_2 oxidation increased from approximately 10 mA/cm^2

to 15 mA/cm^2 rather than doubling as might be expected, the increase was greater in relative magnitude than that observed for the diffusion limited HER current density in the range of 0 to -300 mV vs RHE. These differences in HOR vs HER behavior on the Pt mesh electrodes suggested that the figure of merit for the porous electrode varied depending on the electrochemical reaction taking place. The diffusivity of protons (which is typically similar in value to gaseous H_2 in dilute solution) might have been suppressed relative to gaseous H_2 due to the polar protons forming a complex with sulfate ions in solution and hindering their diffusivity, as has been observed in previous research [25], [26]. The concentration of H_2 (~1 mM) was at minimum an order of magnitude greater than the largest proton concentration, meaning that concentration effects on the diffusivity could have also caused the differing responses of protons and H_2 to surface area. The oxidation efficiency of H_2 was still low, ~3%, on the 6 Pt mesh, again confirming that the mesh electrode was a poor form factor for porous electrodes.

Catalyst Material Considerations

The active catalyst material also had a critical role in each electrode's catalytic properties. Deposition of Pt on the porous Nb electrode significantly changed the voltammetry characteristics of the Nb electrode. Two changes in the voltammetry data demonstrated that Pt became the primary active site on the electrode surface. With deposition of Pt on the Nb, the onset potential for HER shifted in a positive direction towards 0 mV vs RHE as expected. In the fast scan CV curves (Figure 5-6 and Figure

5-7), the Nb electrode was evaluated over a wide potential range, especially in the positive potential range, whereas the NbPt electrode a significant oxidation wave started positive of 0 mV that prevented characterization over a wider positive potential range due to the uncompensated resistance inherent in the cell causing significant potential losses. Since Pt is an extremely efficient HER and HOR catalyst, these changes in the voltammetry data demonstrated that Pt became the dominant active catalyst site on the NbPt sample whereas the native Nb oxide was the active site on the unaltered porous Nb sample.

The Nb and NbPt catalysts exhibited marked differences in their conversion behavior despite both showing excellent HER conversion efficiency compared to pure Pt mesh. The Tafel data presented in Figure 5-18 and Figure 5-19 showed different trends in the equilibrium potential (where each curve shows a minimum representing the current going from a positive to a negative value) with varying HOR current. There was a clear shift in the minimum point on the curves of the composite NbPt electrodes that was not as pronounced on the pure Nb electrode. Figure 5-22 shows a plot of the potential of the minimum current density with NbPt electrodes as a function of the theoretical pH as calculated from the upstream HOR current density, and the data show evidence of characteristic Nernstian behavior where the equilibrium potential scales in a logarithmic relationship as the concentration of the oxidized species (protons) increases and the reduced species (H_2) decreases. We observed a shift of 16 mV rather than the theoretical shift of 53 mV as calculated from the Nernst equation. The 4 data points at with the lowest pH values exhibited linear behavior as a function of pH as is ideal, however the slope of these points was 24 mV, rather than the theoretical slope of 59 mV. The deviation from ideal behavior could be explained as a result of the nature of the porous electrode as the pH varied from low to higher pH through the thickness of the NbPt catalyst due to proton reduction at the leading face causing decreased proton concentration through the thickness. This effect would have led to a gradient in the Nernst potential through the thickness of the NbPt and deviation from ideal Nernst behavior. Conversely, the Nb electrodes exhibited minimal variation in equilibrium potential as a function of upstream HOR current, which as discussed later may have arisen due to the nature of the passivating Nb oxide in the potential range explored here. These differences further demonstrated that the deposited Pt on the porous Nb was the primary catalytic site for the composite electrodes and improved the activity relative to the bare Nb electrode.

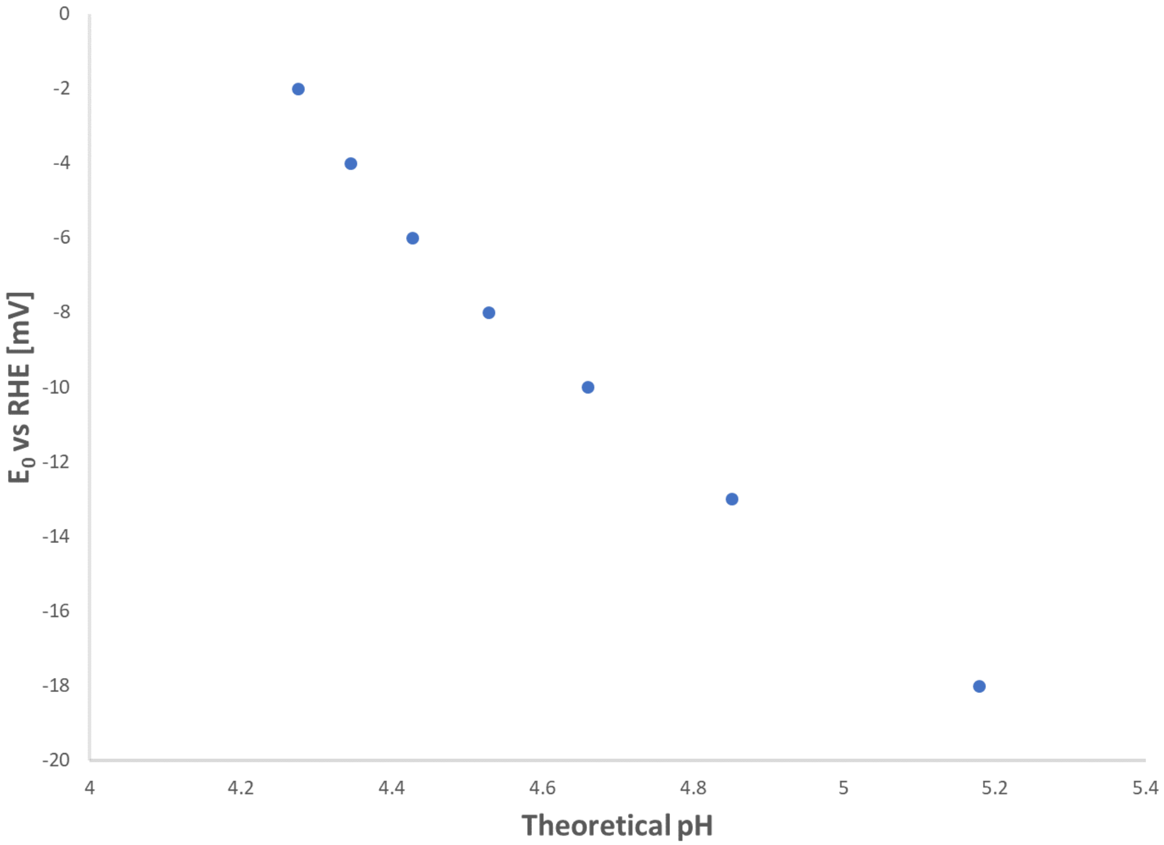

Figure 5-22. Equilibrium potential of NbPt electrode as determined from Tafel plots of slow CV data as a function of the theoretical pH of the electrode due to the upstream HOR oxidation current.

The differences in the HER conversion efficiencies of the porous Nb and NbPt catalysts were attributed to the nature of the Nb catalyst surface and its stability at the potentials probed. The bare Nb electrodes showed peak HER conversion rates well in excess of 100%, especially at the lowest HOR current densities probed, while the NbPt catalysts converted almost exactly at 100% over the range of HOR current densities. The HER conversion efficiencies on bare Nb peaked around -250 mV vs RHE before decaying at larger cathodic overpotentials, while the NbPt conversion efficiencies remained constant in the potential range of proton reduction. In these regards, the NbPt catalyst behaved in a more ideal fashion—converting all available protons to H_2 at unit efficiency over the range where H_2O reduction didn't compete. The Nb catalyst had a more complicated behavior, likely due to the nature of the Nb oxide on the surface of the catalyst. We attribute the apparent conversion in excess of 100% to the electrochemical behavior of the oxide layer and suspect the that the real conversion rate was substantial but less than 100% calculated from the raw data. The stable form of the passivating niobium oxide reduces from Nb_2O_5 to NbO_2 to NbO at -289, -655 and – 733 mV versus RHE respectively as illustrated by the Pourbaix diagram in Figure 5-23 [27], [28]. The transition from Nb_2O_5 to NbO_2 occurs by the reaction shown in Equation 5.6 [27].

$$Nb_2O_5 + 2H^+ + 2e^- \rightarrow 2NbO_2 + H_2O \qquad 5.6$$

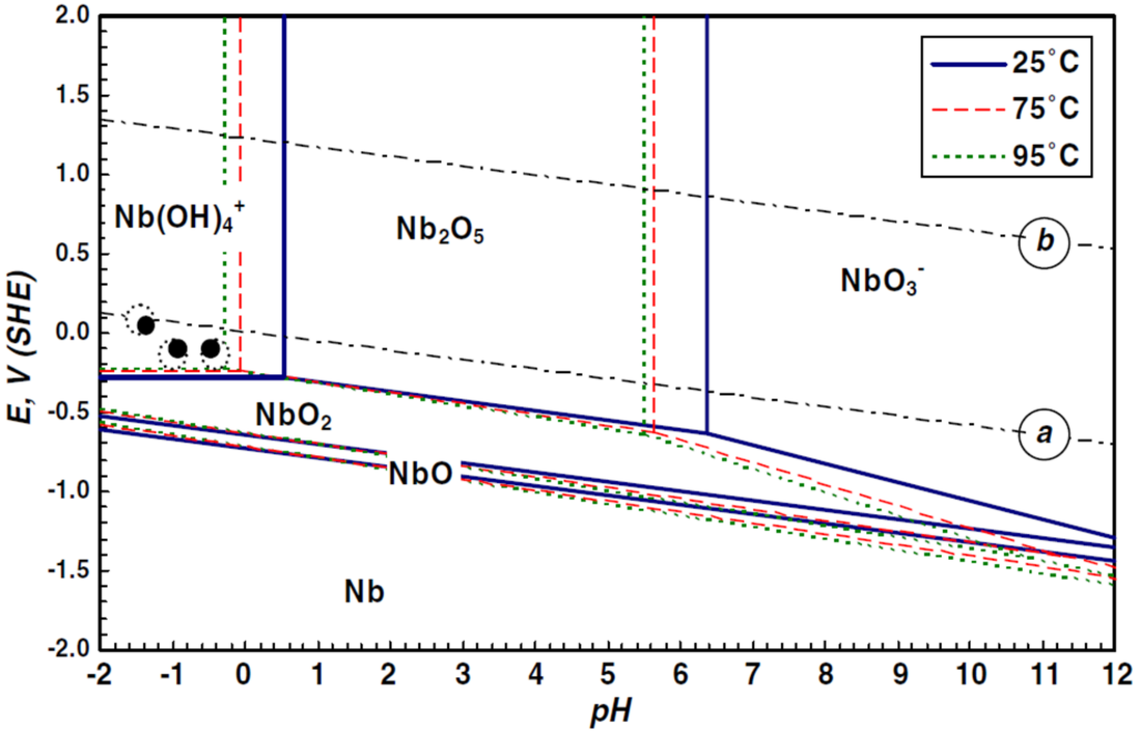

Figure 5-23. Calculated Pourbaix diagram for Niobium-H_2O system. Lines a and b show the potentials corresponding to reductive and oxidative reactions of H_2O. Figure adapted from Asselin, et. al [28].

The theoretical onset potential for electrochemical reduction of Nb_2O_5 to NbO_2 occurs very near the observed peak in HER conversion efficiency, and concurrent reduction of the Nb oxide with HER would have yielded an artefact in the slow CV data provided the oxide reduction occurred on a longer time scale than the potential sweep.

Prior research has also suggested that Nb_2O_5 can form stable hydroxides under cathodic polarization in the presence of protons leading to enhanced HER rate [27]. A change in the surface structure may have yielded local areas with greater HER activity than Nb_2O_5 as has been observed, and since these reactions require protons as a reactant, it is feasible that increasing the HOR current density yielded a greater area density of locally active surface oxides and hydroxides leading to apparent HER conversion rates in excess of 100% since the baseline HER curve would have been obtained with lower coverage of the more active surface areas for HER. The decay in the maximum HER efficiency with HOR current density also supports this hypothesis and suggests that the maximum conversion efficiency of the bare Nb was less than 100% as was achieved with Pt deposited on the Nb catalyst.

The data for bare Nb show the change in the excess HER current density with increasing HOR current density appeared to stabilize at the largest HOR current densities. At -400 mV versus RHE the excess HER current density increased in magnitude by approximately 1.1 mA/cm^2 when the HOR current density changed from 7.07 to 8.84 and 8.84 to 10.61 mA/cm^2. Assuming a similar surface structure at each of these larger HOR current densities and using the 7.07 mA/cm^2 curve as a baseline yields, the conversion efficiency measured 65%, which was still significant compared to the Pt mesh but seems more reasonable compared to the highly active NbPt catalyst. These conversion efficiencies are less than that predicted by the figure of merit calculation based on diffusional mass transport within the pores. However, the figure of merit was near the previously observed experimental limit corresponding to complete conversion, and the electrochemical reactions and electrodes used in other systems to determine this limit were operated at significantly lower flow rates and carefully chosen to avoid complexities that might arise from using a catalyst such as Nb that has a passive oxide layer and is prone to secondary, structure changing reactions in the potential range of interest.

Hydrogen intercalation also occurs in Nb, yielding another possible source of protons although the porous Nb electrode was immersed in flowing H_2 saturated solution for a minimum of 30 minutes prior to voltammetry data being gathered and the curves obtained showed repeatable trends when sampled in order of ascending HOR current densities then repeated starting at the lowest HOR density, suggesting that the intercalation wasn't an important factor in the HER characteristics and also that structural changes to the passive oxide were reversible.

HOR Characteristics

After discovering the excellent HER characteristics of the NbPt electrodes, we attempted to perform efficient HOR with the NbPt electrode. The current density achieved on the CV corresponded to a theoretical HOR efficiency of ~12% based on a theoretical H_2 solubility of approximately 1 mM in the electrolyte (also ignoring Non-Faradaic effects associated with the CV scan in the calculation). This efficiency is well below that predicted by the figure of merit calculations, however the qualitative aspect could be more promising than the initial quantitative analysis suggests. It wasn't clear that the HOR current had peaked, and the ability of the NbPt to efficiently oxidize H_2

wasn't explored in great detail since the large current densities achieved with the NbPt HOR catalyst combined with the uncompensated resistance inherent in the flow cell (~60 ohms or greater) created potential losses that were too large to reasonably accommodate with the potentiostats.

Conclusions

Sequential HOR and HER experiments in a flow cell containing two complete electrochemical cells demonstrated the feasibility of using the sequential electrolysis approach for precisely controlled protonation reactions, such as electrochemical NH_3 synthesis. The flow cell employed a unique order of electrodes to provide optimal control of the proton concentration at the downstream working electrode. The two working electrodes were upstream of the counter electrodes, providing minimal exposure of the working electrodes to the products of the anodic reactions.

The experiments were performed at large volumetric flow rates and current densities relative to those examined in previous flow cell electrolysis experiments and with H_2 source gas rather than fully ionic reactants to more closely mimic an industrial setting. The large flow rates and associated large pressures (when using an electrode with ~10 μm pores and ~1 mm thickness) were possible due to the novel porous Nb catalyst, which was reinforced with silicides to provide sufficient mechanical stability in the high-pressure environment of the flow cell.

Several working HER electrodes were evaluated. Porous Nb and porous Nb functionalized with Pt nanoparticles converted protons generated from upstream HOR back to hydrogen at 100% efficiency (for NbPt) and greater than 60% efficiency (for Nb) at all HOR current densities, while stainless steel mesh and stacks of Pt converted HOR generated protons to H_2 at negligible efficiencies despite similar surface areas to the porous Nb electrode. These results largely matched previous theoretical and experimental work on the effects of porous electrode geometry on electrochemical efficiency in a flow cell environment. The Nb electrode functionalized with Pt nanoparticles proved to be a more efficient HER catalyst than the Nb electrode alone, and this trend was attributed to the complex nature of the oxide passivated Nb and its lower inherent activity for HER compared to Pt.

The research results suggested that the sequential electrolysis method is a worthwhile candidate for further exploration for NH_3 synthesis and other relevant electrochemical reactions as it provided a viable means for direct independent control of proton concentration at the electrode of interest outside of varying electrolyte concentrations with significant conversion efficiency at the second working electrode. The flow cell design and electrodes used for HOR prevented characterization of the cell over an even larger range of current densities. As this work represented the first iteration of the flow cell and Nb catalyst, further improvements on the design of the flow cell to reduce inherent resistance and tailoring of the Nb electrode characteristics will almost certainly allow for characterization and experimentation with sequential electrolysis under a much wider range of conditions.

Future Work

Improvements to the cell design that limit resistance in the cell could greatly limit the potential losses we observed attempting to operate at larger current densities. In the system explored here, using NbPt as the HOR electrode would have been beneficial for study of the sequential reactions at larger current densities. This could be an ideal setup for other studying gas phase electrolysis systems as well where more conventional cells bubble significant excess of gas phase reactants through the electrolyte resulting in large release of the reactants to atmosphere. The porous catalysts could also be tailored to optimize their pore size and composition for efficient conversion while minimizing the pressure gradient across the porous electrodes.

Altering the cell to remove the counter electrodes from the electrolyte to prevent contamination of the electrolyte and backwards reaction of desired reduction products may also be desirable. We performed preliminary testing with the counter electrodes located in a separate electrolyte with an anion exchange membrane ported to the flow cell channel. The experiments were somewhat successful, however polarization effects due to increased cell resistance and large variations in electrolyte pH (due to unbalanced reactions in the catholyte) hindered analysis of the HOR/HER reaction so we kept both counter electrodes in the cell for these experiments. With improved cell design, these limitations could be overcome leading to more controllable electrolyte environment.

References

[1] J. Durst, A. Siebel, C. Simon, F. Hasché, J. Herranz, and H. A. Gasteiger, "New insights into the electrochemical hydrogen oxidation and evolution reaction mechanism," *Energy Environ. Sci.*, vol. 7, no. 7, pp. 2255–2260, Jun. 2014.

[2] M. Gong, D.-Y. Wang, C.-C. Chen, B.-J. Hwang, and H. Dai, "A mini review on nickel-based electrocatalysts for alkaline hydrogen evolution reaction," *Nano Res.*, vol. 9, no. 1, pp. 28–46, Jan. 2016.

[3] F. Safizadeh, E. Ghali, and G. Houlachi, "Electrocatalysis developments for hydrogen evolution reaction in alkaline solutions – A Review," *Int. J. Hydrogen Energy*, vol. 40, no. 1, pp. 256–274, Jan. 2015.

[4] W. Sheng *et al.*, "Non-precious metal electrocatalysts with high activity for hydrogen oxidation reaction in alkaline electrolytes," *Energy Environ. Sci.*, vol. 7, no. 5, pp. 1719–1724, Apr. 2014.

[5] W. Sheng, H. A. Gasteiger, and Y. Shao-Horn, "Hydrogen Oxidation and Evolution Reaction Kinetics on Platinum: Acid vs Alkaline Electrolytes," *J. Electrochem. Soc.*, vol. 157, no. 11, p. B1529, Nov. 2010.

[6] Y. Shi and B. Zhang, "Recent advances in transition metal phosphide nanomaterials: synthesis and applications in hydrogen evolution reaction," *Chem. Soc. Rev.*, vol. 45, no. 6, pp. 1529–1541, Mar. 2016.

[7] D. Strmcnik *et al.*, “Improving the hydrogen oxidation reaction rate by promotion of hydroxyl adsorption,” *Nat. Chem.*, vol. 5, no. 4, pp. 300–306, Apr. 2013.

[8] Z. Zhuang *et al.*, “Nickel supported on nitrogen-doped carbon nanotubes as hydrogen oxidation reaction catalyst in alkaline electrolyte,” *Nat. Commun.*, vol. 7, p. 10141, Jan. 2016.

[9] Z. Hou, M. Li, M. Han, J. Zeng, and S. Liao, “Aqueous phase synthesis and characterizations of Pt nanoparticles by a modified citrate reduction method assisted by inorganic salt stabilization for PEMFCs,” *Electrochim. Acta*, vol. 134, pp. 187–192, Jul. 2014.

[10] D. Strmcnik, P. P. Lopes, B. Genorio, V. R. Stamenkovic, and N. M. Markovic, “Design principles for hydrogen evolution reaction catalyst materials,” *Nano Energy*, vol. 29, pp. 29–36, Nov. 2016.

[11] M. J. Joncich, L. S. Stewart, and F. A. Posey, “Hydrogen Overvoltage on Rhenium and Niobium Electrodes,” *J. Electrochem. Soc.*, vol. 112, no. 7, p. 717, Jul. 1965.

[12] J. V. Kenkel and A. J. Bard, “A dual working electrode coulometric flow cell,” *J. Electroanal. Chem. Interfacial Electrochem.*, vol. 54, no. 1, pp. 47–54, Jul. 1974.

[13] R. E. Sioda, “Flow electrolysis on a porous electrode composed of parallel grids,” *J. Electroanal. Chem. Interfacial Electrochem.*, vol. 34, no. 2, pp. 411–418, Feb. 1972.

[14] S. Kihara, T. Yamamoto, K. Motojima, and T. Fujinaga, "Determination of plutonium by two-step flow-coulometry at the column electrode," *Talanta*, vol. 19, no. 5, pp. 657–668, May 1972.

[15] R. E. Sioda, "Distribution of potential in a porous electrode under conditions of flow electrolysis," *Electrochim. Acta*, vol. 16, no. 9, pp. 1569–1576, Sep. 1971.

[16] R. E. Sioda, "Electrolysis with flowing solution," *Electrochim. Acta*, vol. 13, no. 3, pp. 375–382, Mar. 1968.

[17] W. J. Blaedel and J. Wang, "Flow electrolysis on a reticulated vitreous carbon electrode," *Anal. Chem.*, vol. 51, no. 7, pp. 799–802, Jun. 1979.

[18] R. E. Sioda, "Flow-through electrodes composed of parallel screens," *Electrochim. Acta*, vol. 22, no. 4, pp. 439–443, Apr. 1977.

[19] B. G. Ateya, "Effects of radial diffusion on the efficiency of porous flow-through electrodes," *J. Appl. Electrochem.*, vol. 10, no. 5, pp. 627–634, Sep. 1980.

[20] C. Lamoureux, C. Moinet, and A. Tallec, "An electrolysis cell with close consecutive flow-through porous electrodes for particular organic electrosynthesis," *J. Appl. Electrochem.*, vol. 16, no. 6, pp. 819–824, Nov. 1986.

[21] E. Beinrohr, M. Nemeth, P. Tschopel, and G. Tolg, "Design and characterization of flow-through coulometric cells with porous working electrodes made of

crushed vitreous carbon," *Fresenius. J. Anal. Chem.*, vol. 343, no. 7, pp. 566–575, 1992.

[22] B. G. Ateya, E. A. S. Arafat, and S. A. Kafafi, "Hydrodynamic effects on the efficiency of porous flow-through electrodes," *J. Appl. Electrochem.*, vol. 7, no. 2, pp. 107–112, Mar. 1977.

[23] S. H. Lee and J. C. Rasaiah, "Proton transfer and the mobilities of the H^+ and OH^- ions from studies of a dissociating model for water," *J. Chem. Phys.*, vol. 135, no. 12, p. 124505, Sep. 2011.

[24] B. R. Munson, D. F. Young, and T. H. (Theodore H. Okiishi, *Fundamentals of Fluid Mechanics*. Wiley, 2002.

[25] J. V Macpherson and P. R. Unwin, "Determination of the Diffusion Coefficient of Hydrogen in Aqueous Solution Using Single and Double Potential Step Chronoamperometry at a Disk Ultramicroelectrode," 1997.

[26] M. L. Soudijn, "Proton Transport in Aqueous Ionic Solutions," 2012.

[27] H. V. K. Udupa and V. K. Venkatesan, "Encyclopedia of Electrochemistry of the Elements," in *Encyclopedia of Electrochemistry of the Elements*, A. J. Bard and J. A. A. Ketelaar, Eds. Marcel Dekker, 1974, pp. 53–117.

[28] E. Asselin, T. M. Ahmed, and A. Alfantazi, "Corrosion of niobium in sulphuric

and hydrochloric acid solutions at 75 and 95 °C," *Corros. Sci.*, vol. 49, no. 2, pp. 694–710, Feb. 2007.

Chapter 6 – Electrochemical Ammonia Synthesis

Introduction

In the previous chapter, we demonstrated that porous Nb catalysts in the flow cell efficiently employed the upstream HOR products for HER. Based on the results of the model HOR/HER reactions we try for direct electrochemical synthesis of ammonia in the flow cell from N_2 and H_2 source gases using porous Nb as the reduction catalyst, knowing that the material could proficiently use protons for electrochemical reduction reactions. Since the electrochemical NH_3 synthesis reaction is notoriously difficult and inefficient due to HER competition as described in Chapter 3, the goal of these experiments was primarily to determine if the bare Nb catalyst had any utility for NH_3 synthesis or would require functionalization to change the primary catalyst site (as demonstrated with Pt nanoparticles for HER) for future research using the beneficial features of the sequential flow cell.

Experimental

Electrochemical ammonia synthesis was attempted in the flow cell described in the previous chapters using a 0.69 mm thick piece of porous Nb as the working electrode. The volumetric flow rate was decreased to the minimum achievable with the pump of

22 mL/min. Forming gas was used to supply N_2 and H_2 with a ratio of 95:5. The pH of the 1 M Na_2SO_4 electrolyte (60 mL was used in each test) was adjusted to 7.917 with 1 M NaOH. The electrolyte container was continuously purged during the tests with the excess gas bubbled through 40 mL of 10 mM HCl in a trap in order to collect outgassed NH_3 in the acid as NH_4^+. The initial control experiments were performed without employing the upstream HOR electrode, and the NH_3 working electrode was held galvanostatically at reducing current densities of 5 and 50 mA/cm^2 for greater than 6 hours with continuous electrolyte flow. At the conclusion of these tests, the Na_2SO_4 electrolyte and the liquid from the 10 mM HCl trap were tested for ammonia/ammonium presence with a commercial kit capable of detecting ammonia in concentrations under 1 ppm.

Ammonia was not detected at either of the cathodic current densities evaluated. This result wasn't surprising considering the demonstrated activity of the bare Nb for HER. The large overpotentials required to generate NH_3 as well as the current densities evaluated here were sufficient for substantial HER at the Nb electrode. In addition, Nb has not been predicted or demonstrated as an effective NH_3 catalyst. The porous Nb remains a promising support material, but further testing with the robust porous Nb for NH_3 synthesis should focus on functionalization of the NH_3 reduction electrode with an NH_3 active catalyst while using Pt functionalized Nb as the upstream HOR catalyst for efficient oxidation of H_2 in the electrolyte.

Further next steps for NH_3 synthesis require improving cell resistance such that the sequential reactions can be performed in either a non-aqueous or mildly alkaline to alkaline, aqueous electrolyte with both N_2 and H_2 feed gases where HER through H_2O or proton reduction won’t be so favorable compared to NH_3 formation at the cathodic potentials required to form NH_3. We attempted to perform HOR/HER with methanol and DMSO based solvents with large concentrations of LiCl, however the internal cell resistance in these electrolytes yielded uncompensated resistances greater than 300 ohms which severely limited the potential range we could sample.

Chapter 7 - Novel Mediators for Copper Electrodeposition in Recessed Features

Introduction

The work presented in this chapter began under the advisement of Professor Bob Cammarata, who sadly passed away in 2016. He was a kind, humorous and gifted advisor, mentor and professor who guided this work through its early stages. While the research presented below does not directly involve porous materials, it required a great deal of electrochemical research with Cu which set the foundation for our work presented earlier on NP-Cu.

Electrodeposition of copper for integrated circuit (IC) applications has been widely researched for several decades. Research and development of the processes to produce dense, defect free Cu films within recessed features with sub-micron dimensions (such as the famous Damascene process) presented a major challenge when Cu was adapted as the material of choice metallization of IC's. Research into these processes remains active as refined techniques continue to allow electrodeposition of pristine Cu films into deep recessed geometries as the feature sizes on IC's shrink to nm dimensions [1]–[6].

The engineering challenge with depositing Cu for IC applications can be briefly summarized as follows. The operating demands on the metallized portions of the IC require the deposited Cu films to be free of major defects such as voids, seams or inclusions, while the geometries of the recessed features (particularly the depth/width ratios) that must be filled with Cu during manufacture of the IC's requires that any method used to deposit Cu must deposit at a significantly greater rate at the bottoms of the features relative to the sidewalls in order to completely fill the feature with pristine Cu films. Electrodeposition processes that yield enhance deposition rates at the bottoms of recessed features relative to the walls due to local variations in adsorbed species affecting deposition rates are commonly referred to as 'bottom-up' or 'superconformal'. Invention of deposition processes with such characteristics is challenging, but several techniques have been developed as well as models that effectively model the deposition processes [3], [7]–[11].

The earliest technique for bottom up deposition of Cu was an acidic copper sulfate electrolyte that relied on an organic leveling agent adsorbed on the surface of the growing film to produce differential local deposition rates [1]. The leveling agent suppressed the deposition rate of Cu where adsorbed and was also consumed during deposition via incorporation into the Cu film. Due to mass transport effects, leveler molecules reach and are consumed at greater rates at surfaces closer to the bulk electrolyte, while less of the rate suppressing species reaches the bottoms of recessed features. The gradient in adsorbed leveler across the profile of the recessed features that results causes Cu to deposit at greater rates at the bottoms of recessed features. The technique requires fewer additives or experimental controls to implement compared to others discussed below, however the incorporation of the inhibiting species into the growing film yields relatively large impurity concentrations in the deposited Cu film which adversely affects the film's electrical properties [12]. Modern feature sizes are also too small to effectively employ this technique.

Another widely employed and studied modern technique for bottom-up deposition relies on several additives to an acidic copper sulfate electrolyte to achieve the desired deposition characteristics [2]–[6], [10], [11]. The model that effectively describes this technique is commonly referred to as the Curvature Enhanced Accelerated Coverage (CEAC) model. The electrolyte typically contains and additive that suppresses Cu deposition rates when adsorbed on the Cu film (often a polyether) and one that increases Cu deposition rate (typically a thiol). The additives adsorb across the various areas of the profile of the Cu seed layer at nominally constant coverages across the profile prior to deposition. As deposition commences and concave surfaces grow and lose surface area (such as at the bottom of a recessed feature), the rate suppressing species is competitively displaced by the rate increasing species, while the relative coverages of the two additives remain the same at advancing flat surfaces (such as the sidewalls of recessed features). The variation in local coverages of the adsorbed species results in significant local variation of the Cu deposition rates to allow for dense filling of features on the order of tens of nanometers. The effectiveness for bottom up filling is sensitive to concentrations of the various additives, and their consumption at the growing film can limit the lifetime of the deposition bath.

More recently, another technique has been developed to yield bottom up filling of sub-micron features which uses an additive that passivates the substrate surface for Cu deposition [13]–[15]. The passivating layer blocks Cu deposition without a sufficiently large overpotential for Cu reduction. At sufficiently large overpotential, Cu deposition initiates at defects in the blocking film, providing a low resistance path for further Cu deposition once the blocking film is interrupted. On planar substrates characteristic patterns emerge where areas of Cu film growth are surrounded by areas of minimal deposition where the passivating film remained intact. The technique is referred to as negative differential resistance (NDR) owing to a characteristic shape in cyclic voltammetry curves obtained with these additives present in the electrolyte. In patterned substrates, the deposition can be controlled such that the passivating film is preferentially disrupted at the bottoms of the features. Such control is achieved by careful immersion of the substrate in the electrolyte such that the inhibiting species first reaches all surfaces except the bottoms of recessed features, and thus Cu deposition occurs only at the bottoms of recessed features while being blocked everywhere else on the substrate profile. The technique yields dramatic bottom up filling, but is sensitive to the applied deposition potential as well as careful immersion of the substrate.

In this work we explore the effects of novel mediators for electrodeposition of Cu thin films in recessed features on model IC systems. Two mediating systems were evaluated as potential additives to yield electrodeposition of dense Cu films in recessed features. We first examine the effects of organic acids on the deposited Cu films. Organic additives are an active area of research for Cu electrodeposition for printed circuit board and IC applications, and organic acids have been shown to have beneficial effects on the quality of Cu films deposited in deep recessed features and through holes for these substrates [16]–[23]. One study showed that addition of acetic acid to copper sulfate based electrolytes inhibited Cu deposition, and the authors postulated that molecular acetic acid adsorbed on the depositing Cu films forms a complex with other organic additives that thereby mediated Cu deposition and improved film quality [23]. Based on these studies, we first explored the effects of two organic acids, acetic (HOAc) and tartaric (HTar), on Cu films deposited on our model IC substrates.

Based on the findings of the Cu deposition in the presence of organic acids, we also explored electrodeposition mediated by atomic Pb underpotential deposition (UPD) of up to one monolayer of Pb on the surface of the deposition Cu film. The UPD technique, which uses up to a monolayer of an adsorbed elemental mediator at the film/electrolyte interface, has been used to electrodeposit high quality films of several metals by inducing 2D growth of the film, and we show it has dramatic effects on Cu deposition in recessed features as well [24]–[26]. A previous study examining UPD mediated deposition of Cu for interconnects showed that approximately 1 atomic percent Pb incorporated into the deposited film [27]. As described in detail below, we not only evaluate effects of UPD mediated Cu deposition, but we use the UPD technique as a contrast to mediation by the organic acids to explore effects of the underlying substrate on deposition characteristics.

Experimental

Model IC substrates were kindly provided by IBM T.J. Watson Research center. The effects of the various mediating agents on Cu deposition were evaluated through cross sectional analysis of the smallest features on the substrates, parallel trenches patterned into the dielectric on the Si wafer, measuring 360 nm deep, by 300 nm wide, with 200 nm between the trenches. The various sections of the profile will be referred to frequently throughout the chapter, and the following nomenclature is adopted. The bottom or base of the recessed trenches is referred to as 'bottom'. The neighboring perpendicular surface to the bottom which appears vertical in all images is referred to as the 'sidewall'. The flat surface between the trenches is referred to as the 'flat'. A barrier layer of TaN/Ta was sputtered on the Si to prevent Cu diffusion into the wafer. The Cu seed layer was sputtered onto the barrier, and this layer measured an average of 51 nm thick at the trench bottom, 14 nm thick at the sidewall, and 59 nm thick at the flat.

Deposition and voltammetry analysis of Cu was performed from organic acid electrolytes containing up to 0.79 M acetic acid or 0.016 M tartaric acid. Cu ions were supplied by copper sulfate for all tartaric acid containing electrolytes and by either copper sulfate or copper acetate for acetic acid containing electrolytes. To examine the effects of Pb mediation, depositions were performed from 0.15 M copper perchlorate electrolytes both with and without 0.30 M lead perchlorate. Ultrapure water (>18 MOhm) and reagent grade salts were used for all electrolytes. For all depositions, the substrate was mounted vertically in 80-90 mL of electrolyte with approximately 0.5 cm^2 of geometric area exposed (with sample edges masked with electroplaters tape). The counter electrode was a soluble Cu foil mounted parallel approximately 1 cm from the substrate. Cyclic voltammetry measurements were obtained on a round, 5 mm diameter Cu foil of predominantly (111) texture that was polished with 1200 grit abrasive prior to each scan. A saturated mercury sulfate reference electrode (MSE) was used for depositions from the organic acid electrolytes and a Cu foil pseudo reference for depositions from the perchlorate based electrolytes. All potentials are referred to the MSE reference. A Princeton Applied Research model 263A potentiostat was used for all depositions. A Mettler Toledo Seven Excellence pH meter was used to measure pH.

For sectional analysis, samples were cleaved and mounted in a two-part epoxy and cured at room temperature. The mounted sections were polished to a 1 micron finish with diamond abrasive and ion milled for the final finish. Film thicknesses were measured by cross-sectional (herein referred to as sectional) SEM micrographs.

Results

Figure 7-1 and Figure 7-2 show cyclic voltammetry results for organic acid containing and perchlorate-based electrolytes. The organic acids inhibited deposition with increased concentration of the organic acids yielding further decreased the deposition rate. These trends were consistent with those previously found for Cu deposition in the presence of acetic acid [23]. The addition of Pb to the perchloric acid-based solutions also inhibited deposition (and caused a 30 mV positive shift in the onset potential) compared to the Pb free electrolyte. The Pb UPD peak was located at –650 mV to –700 mV relative to the Cu deposition potential.

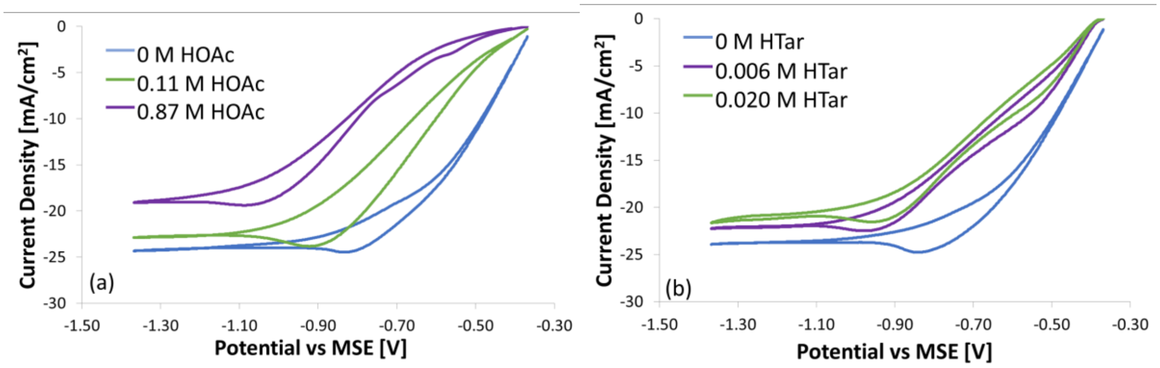

Figure 7-1 Cyclic voltammetry measurements from 0.190 M CuSO4 + 0.007 M H_2SO_4 + HOAc (a) and 0.190 M CuSO4 + 0.007 M H_2SO_4 + HTar (b) on the Cu foil electrode. All scans obtained at 10 mV/sec. Adapted from Ref. [31].

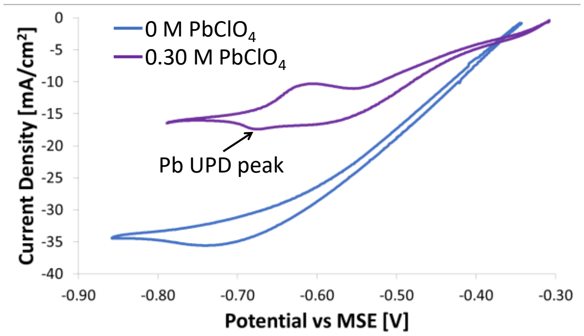

Figure 7-2. Cyclic voltammetry measurements from 0.15 M $Cu(ClO_4)_2$ with and without $PbClO_4$ on the Cu foil electrode. All scans obtained at 10 mV/sec. Adapted from Ref. [31].

Figure 7-3 through Figure 7-5 show sectional micrographs of Cu films deposited from organic acid containing electrolytes at various overpotentials. These films were deposited to partially fill the trenches and allow qualitative and quantitative evaluation of the films at various deposition conditions. Two trends were apparent in the films deposited from the organic acid containing electrolytes. The relative deposition rates at the different areas of the trench profile was dependent on the deposition overpotential.

At lower overpotentials, the deposition rate at the sidewalls was significantly suppressed relative to the bottoms and flats, while the deposition rate tended towards uniform and conformal as the overpotential was increased. The roughness of the deposited Cu films decreased as the deposition overpotential increased. We note that the presence of the organic acids at all concentrations evaluated caused a dramatic change in the quality of the film and the noted trends in the film characteristics. Cu films deposited in the absence of organic acids were of poor quality with large roughness and not suited for the possibility of dense filling of the trenches (Figure 7-5).

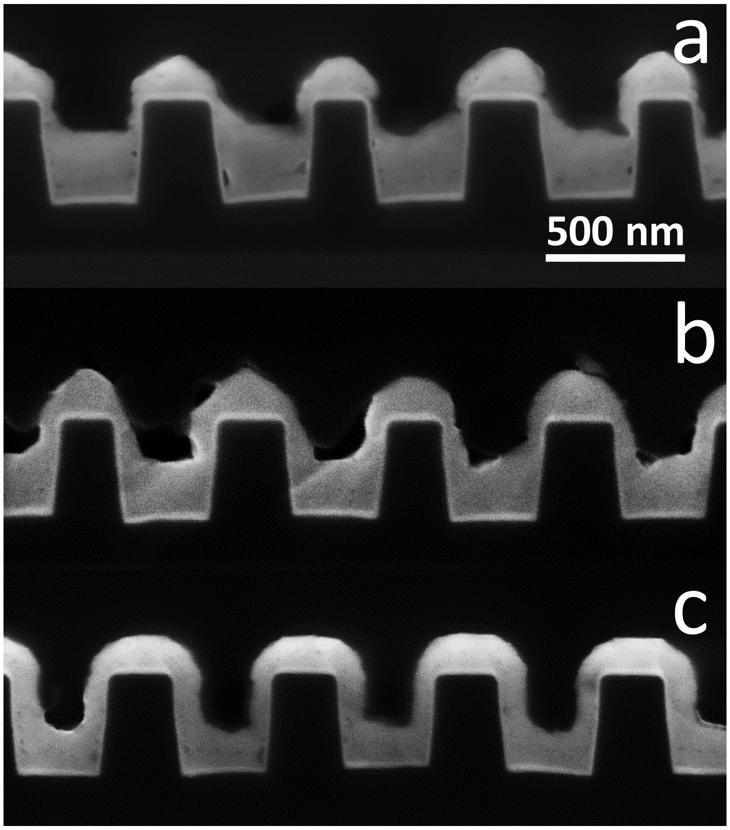

Figure 7-3. Sectional SEM micrographs of Cu films deposited from 0.30 M CuSO4 + 0.79 M HOAc [pH = 2.25] for 155 sec at 80 mV overpotential (a), 84 sec at 120 mV overpotential (b), and 54 sec at 200 mV overpotential (c). Figure from Ref. [31].

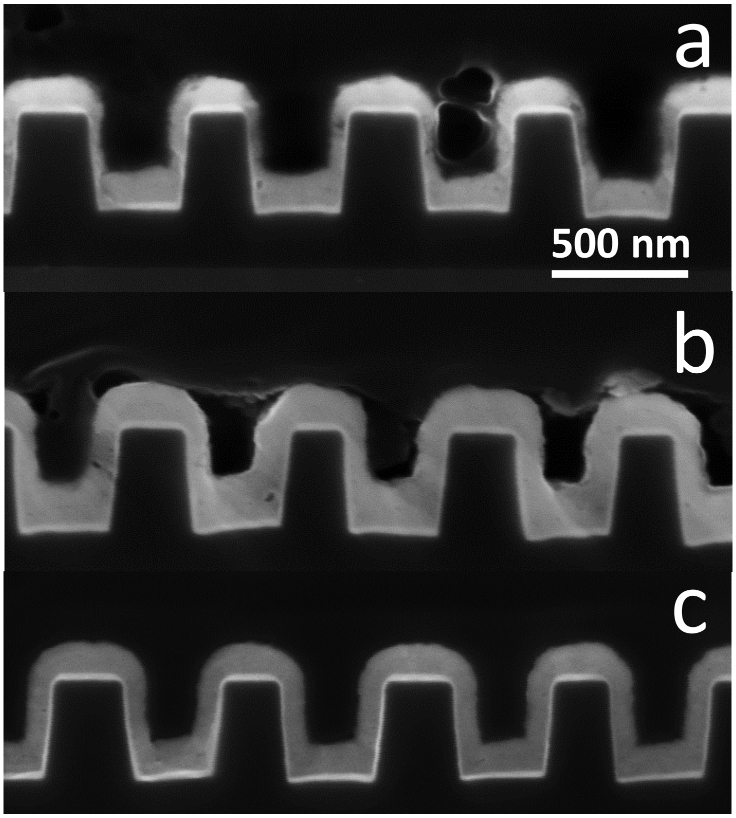

Figure 7-4. Sectional SEM micrographs of Cu films deposited from 0.19 M CuSO4 + 0.16M HTar [pH = 2.26] for 229 sec at 40 mV overpotential (a), 125 sec at 80 mV overpotential (b), and 14 sec at 500 mV overpotential (c). Figure from Ref. [31].

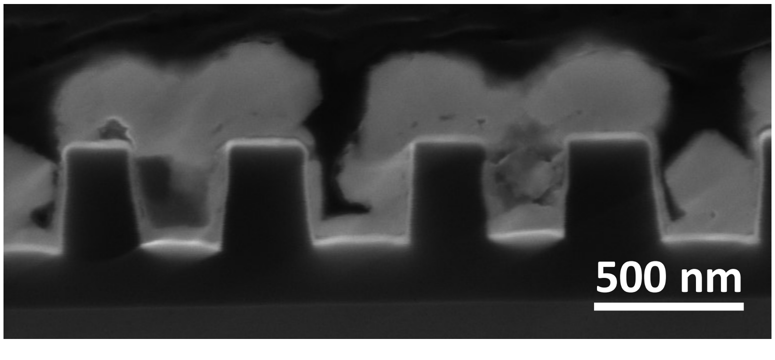

Figure 7-5. Sectional SEM micrograph of Cu film deposited from 0.19 M $CuSO_4$ *+ 0.009 M* H_2SO_4 *[pH = 2.26] for 49 sec at 160 mV overpotential. Figure from Ref.* [31].

Based on the observations of the effects of the overpotential on the film characteristics, potentiostatic Cu film depositions were performed from the organic acid containing electrolytes with the goal of entirely filling the trenches with dense Cu films. Figure 7-6 through Figure 7-8 show results of potentiostatic depositions at sufficiently low overpotentials such that the enhanced deposition rate at the trench bottoms relative to the sidewalls to allowed the film at the trench bottom to grow out of the trench prior to the opposing sidewalls converging and yielding characteristic seam defects in the center of the trenches.

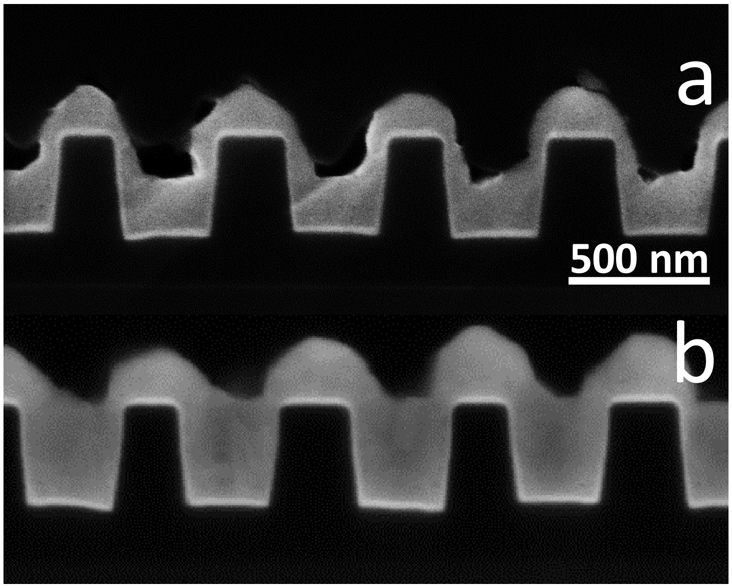

Figure 7-6. Sectional SEM micrographs of Cu films deposited from 0.30 M $CuSO_4$ + 0.79 M HOAc for 84 sec (a) and 163 sec (b) at 120 mV overpotential. Figure from Ref. [31].

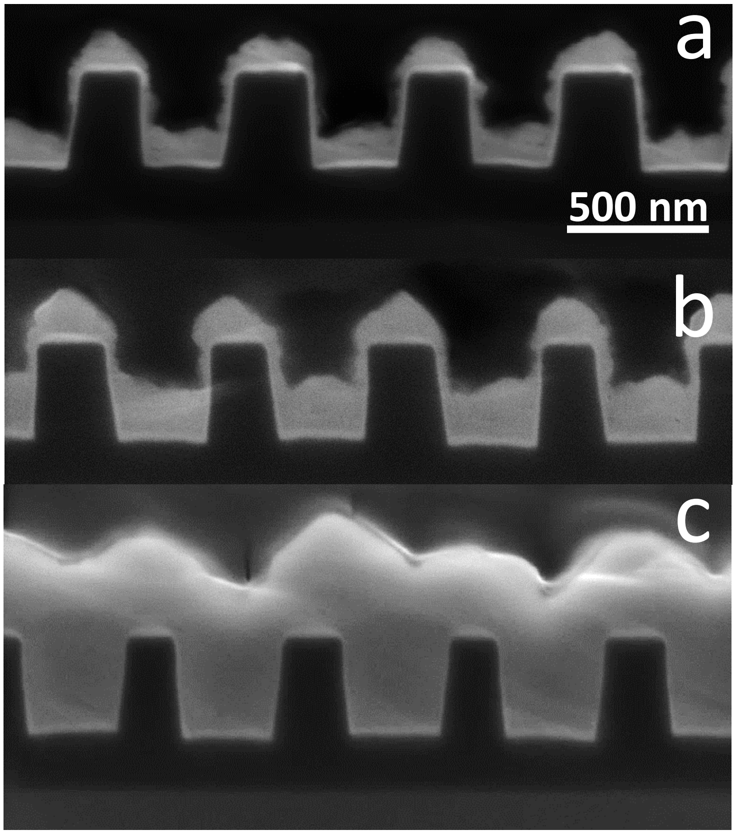

Figure 7-7. Sectional SEM micrographs of Cu films deposited from 0.19 M Cu(OAc)$_2$ + 0.12 M HOAc + 0.38 M H$_2$SO$_4$ [pH =2.12] for for 15 sec (a), 29 sec (b), and 120 sec (c) at 240 mV overpotential. Figure from Ref. [31].

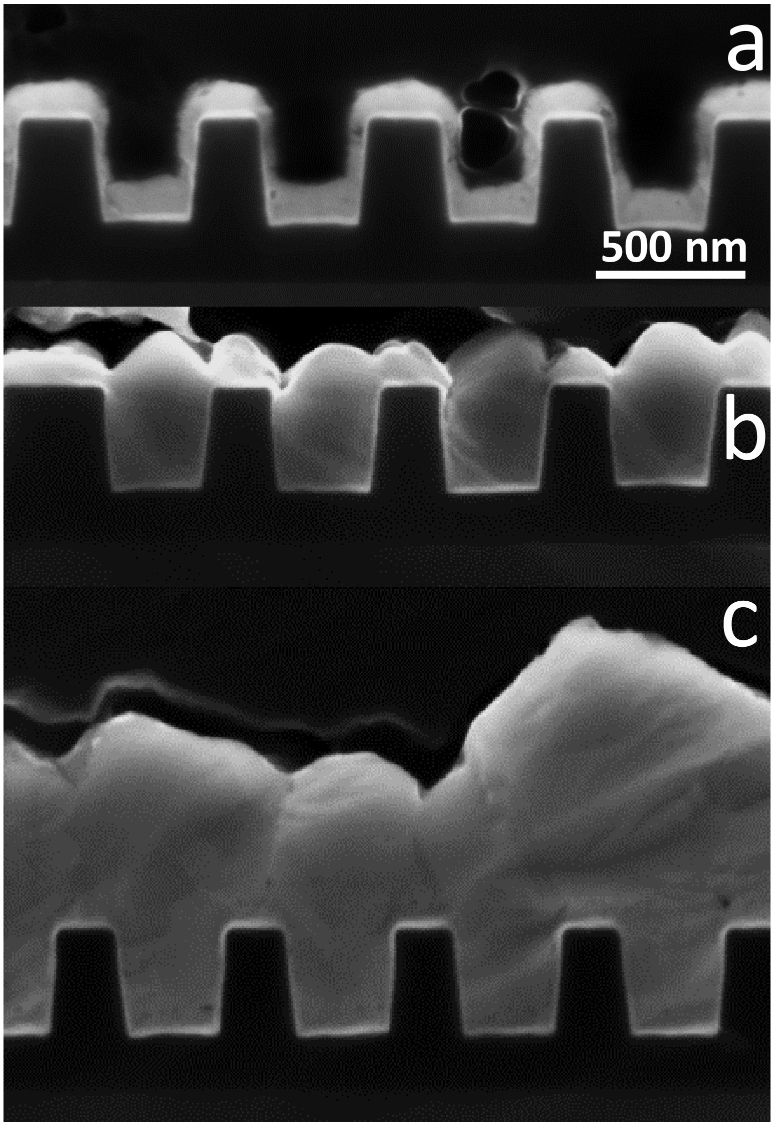

Figure 7-8. Sectional SEM micrographs of Cu films deposited from 0.30 M CuSO4 + 0.79 M HTar for 229 sec (a), 455 sec (b), and 1011 sec (c) at 40 mV overpotential. Figure from Ref. [31].

In order to further optimize the deposited Cu films, two step potentiostatic depositions were performed to take advantage of the dependence of the film conformality and roughness on the overpotential. Depositions were initiated at low overpotential to fill the trenches sufficiently from the bottom such that the film growing from the bottom would grow out of the top of the trench prior to the sidewalls converging, then finished at a large overpotential such that a smooth film would be deposited and overfill the trenches. Figure 7-9 shows an example of such a film and again demonstrates dense filling of the trenches with lower resulting roughness in the overfill area could be achieved.

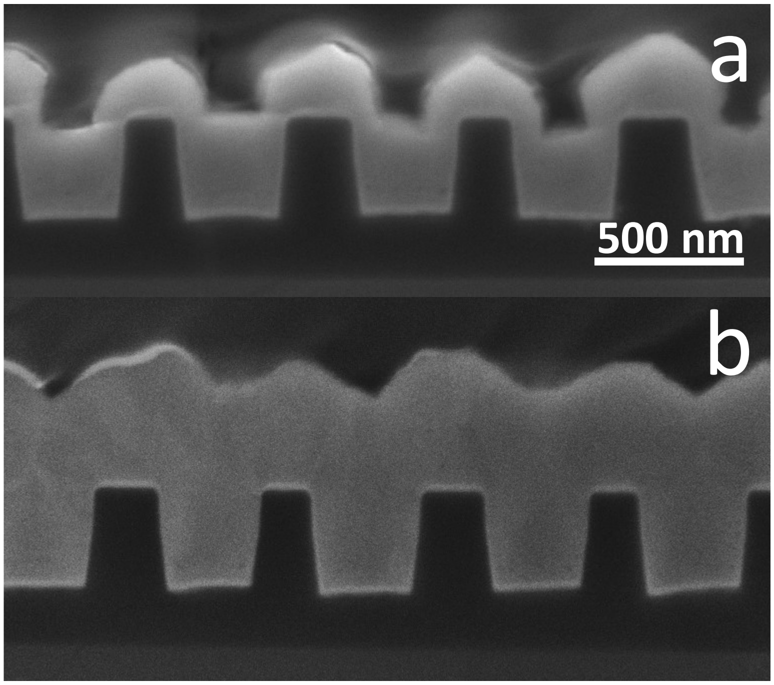

Figure 7-9. Sectional SEM micrographs of Cu films deposited from 0.19 M $Cu(OAc)_2$ *+ 0.12 M HOAc + 0.38 M* H_2SO_4 *for 60 sec at 120 mV overpotential followed by 20 sec (a) and 60 sec (b) at 600 mV overpotential. Figure from Ref.* [31].

Galvanostatic depositions were also performed from an acetic acid containing electrolyte at current densities that corresponded to the overpotentials previously sampled. Figure 7-10 and Figure 7-11 show sectional micrographs of these films, and the results align well with the potentiostatic deposition results. At sufficiently low current densities, we again observe enhanced deposition rates at the trench bottoms and flats, with conformal deposition appearing at larger current densities corresponding to larger overpotentials. In all cases, these results show that electrolytes containing organic acids were capable of producing Cu films free of major defects within the recessed features either by potentiostatic or galvanostatic depositions.

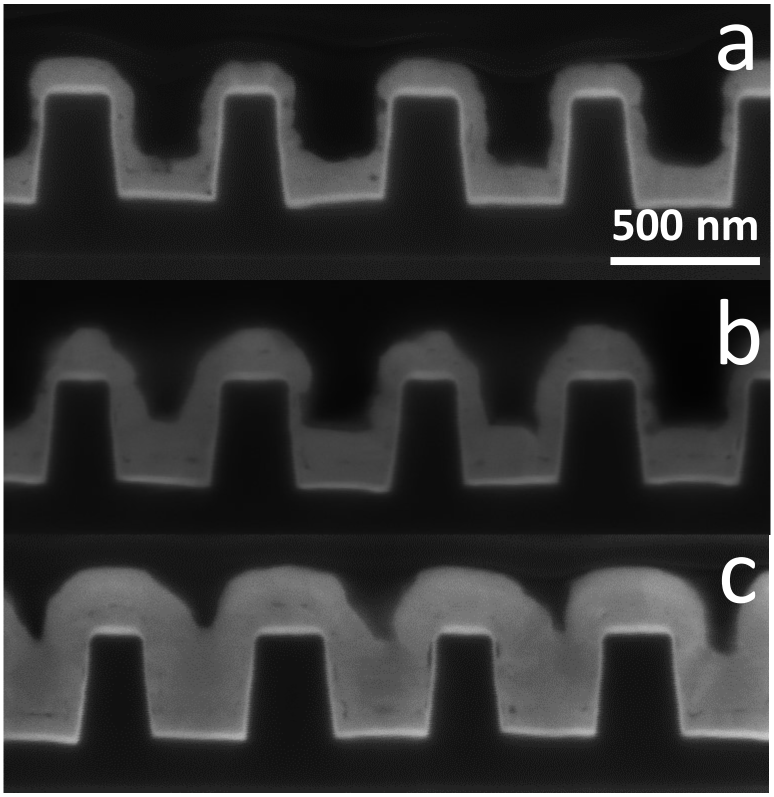

Figure 7-10. Sectional SEM micrographs of Cu films deposited galvanostatically at current density of 5 mA/cm^2 from 0.19 M Cu(OAc)$_2$ +0.12 M HOAc+0.38 M H$_2$SO$_4$ for 45 sec (a),

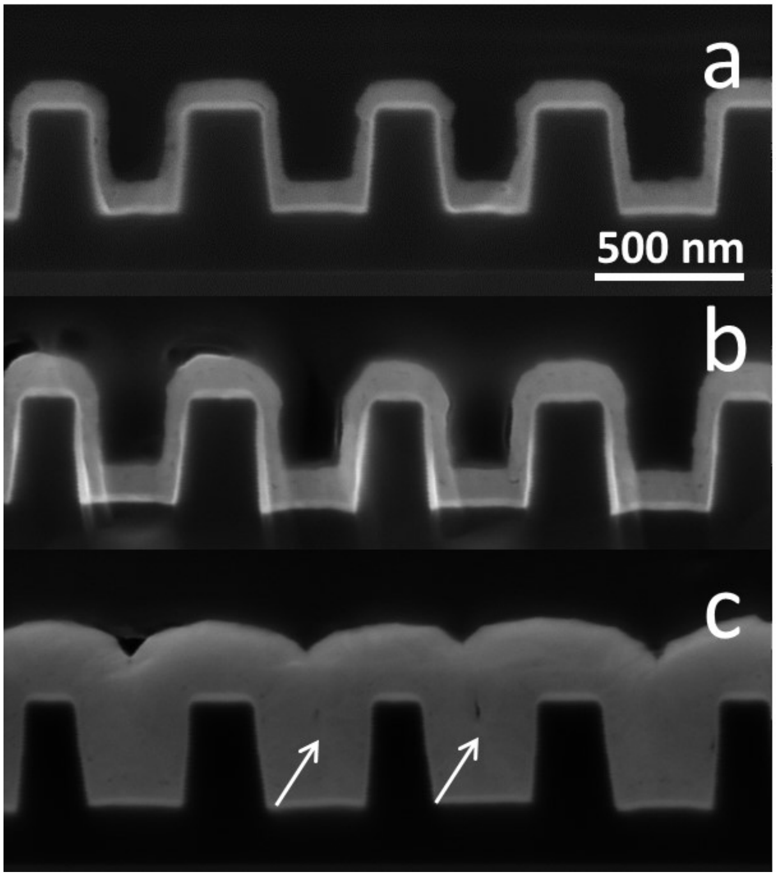

Figure 7-11. Sectional SEM micrographs of Cu films deposited galvanostatically at current density of 8 mA/cm2 from 0.19 M Cu(OAc)2 +0.12 M HOAc+0.38 M H2SO4 for 15 sec (a), 30 sec (b), and 120 sec (c). The white arrows denote center seam defects common to films with conformal deposition across the profile. Figure from Ref. [31].

Figure 7-12 shows sectional micrographs of Cu films deposited with and without Pb mediation from perchlorate-based electrolytes under otherwise identical deposition conditions. The micrographs show that Pb mediation had a profound effect on the deposited Cu film. Without Pb mediation, rough films were deposited preferentially at the sidewalls even at the large deposition overpotentials which corresponded to diffusion limited deposition. With Pb mediation, smooth and conformal films were deposited across all areas of the trench profiles. At sufficiently long deposition times, the sidewalls converged and yielded characteristic center seam defects.

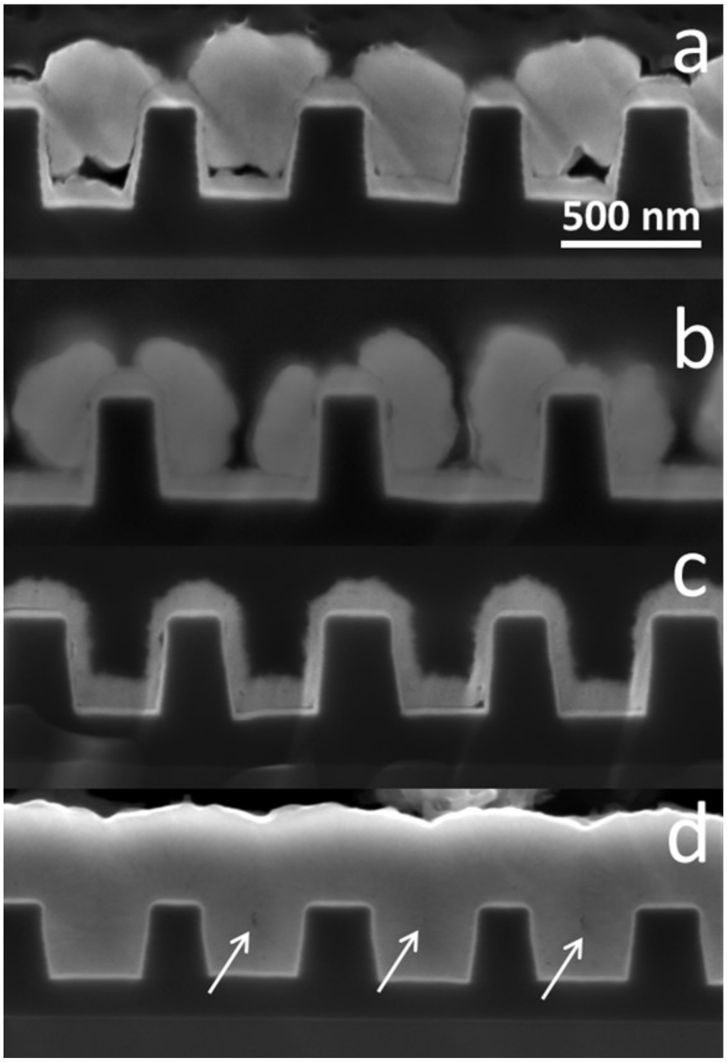

Figure 7-12 Sectional SEM micrographs of copper films deposited from 0.15 M $Cu(ClO_4)_2$ for 34 sec at trenches of varying widths (a) and (b) and 0.15 M $Cu(ClO_4)_2$ + 0.30 M $PbClO_4$ for 9.3 (c) and 54 sec (d). All depositions were potentiostatic at -690 mV vs MSE. The white arrows denote center seam defects common to films with conformal deposition across the profile. Figure from Ref. [31].

Discussion

While dense filling of the trenches, free of bulk defects, was demonstrated with Cu films deposited from organic acid containing electrolytes at low overpotentials or current densities, the mechanism that yielded suppressed deposition rates at the sidewalls only was not immediately apparent as the film characteristics did not appear to match those films deposited via other known mechanisms that allow dense filling of recessed features. The organic acids inhibited Cu deposition as required by additives that yield bottom up deposition by the leveler mechanism. However, in the films deposited with organic acid mediation, the deposition rate at the flats between the trenches was not inhibited as expected in films deposited by the leveler mechanism. The CEAC mechanism described by the associated model, requiring localized displacements of suppressing additives by rate increasing additives at the bottom of trenches, was not used in our films as only a single inhibiting additive was used without a rate increasing additive. The films also did not exhibit characteristic bump overfill above the trenches as is observed with the CEAC mechanism. The dense filling was also not a result of the NDR mechanism as the deposition was not inhibited only at the bottom of the trenches as is characteristic of the NDR mechanism.

To determine the mechanism responsible for the suppressed deposition rates at the trench sidewalls at low overpotentials we first examined the deposition kinetics at various sections of the trench profiles by calculating the effective flux at each section at several overpotentials by measuring the film thickness across the profile in a minimum of 10 trenches at each overpotential. These calculated fluxes, along with the ratios of the current densities (Figure 7-13 and Figure 7-14) were fit to the classic Butler-Volmer (BV) equation (Equation 1.10) by solving for the exchange current density (j_0) and the symmetry parameter (α). The equilibrium potential was held constant for all areas of the profile in this analysis. The analysis was performed for single step and two step reductions of Cu^{2+} ions with nearly identical results. Table 7-1 summarizes these fitting results for several organic acid containing electrolytes. The results indicated that the exchange current density was greater at the bottom and sidewalls of the trenches and the symmetry parameter was greater at the sidewall compared to the trench bottom. While the calculated constants provided good fitting of the data (as shown in Figure 7-15) and the exchange current densities at the flats and bottoms were reasonable compared to previously measured values, the calculated symmetry parameter was significantly less than typical values and thus, purely kinetic considerations as modeled by the BV analysis did not adequately explain the observed trends in the Cu films [28].

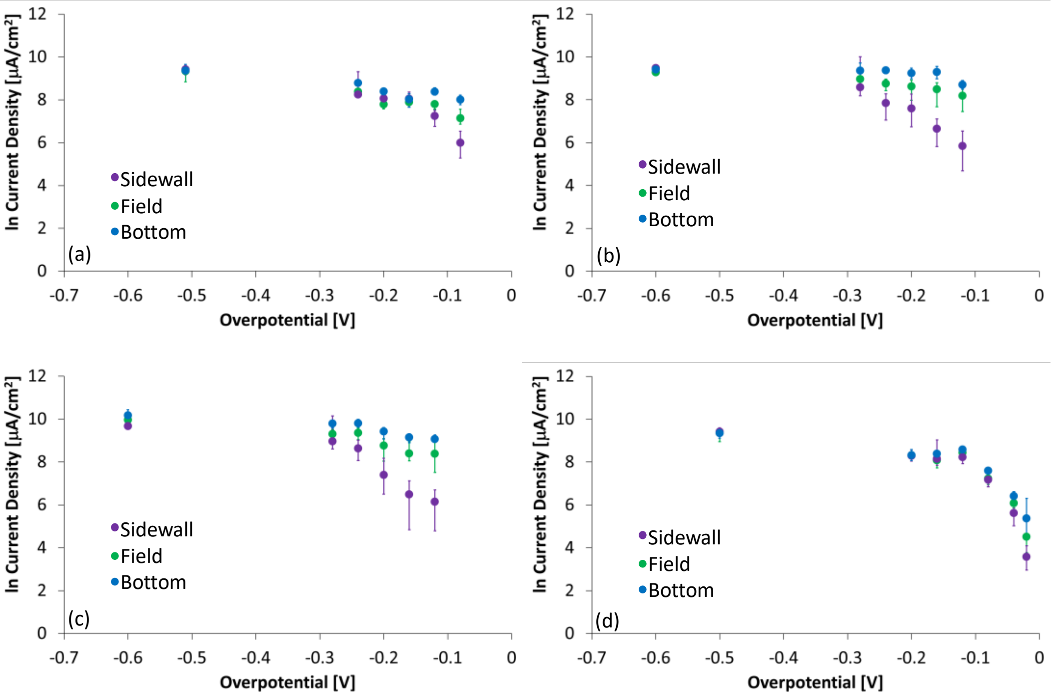

Figure 7-13. Tafel plots of Cu current density at the various sections of the trench features as calculated by thickness measurements from sectional SEM micrographs from 0.30 M $CuSO_4$ + 0.79 M HOAc, (a), 0.19 M $Cu(OAc)_2$+ 0.12 M HOAc + 0.38 M H_2SO_4 (b), 0.19 M $Cu(OAc)_2$+ 0.12 M HOAc + 0.40 M H_2SO_4 (c), and 0.19 M $CuSO_4$ + 0.016 M HTar electrolytes. Figure adapted from Ref [31].

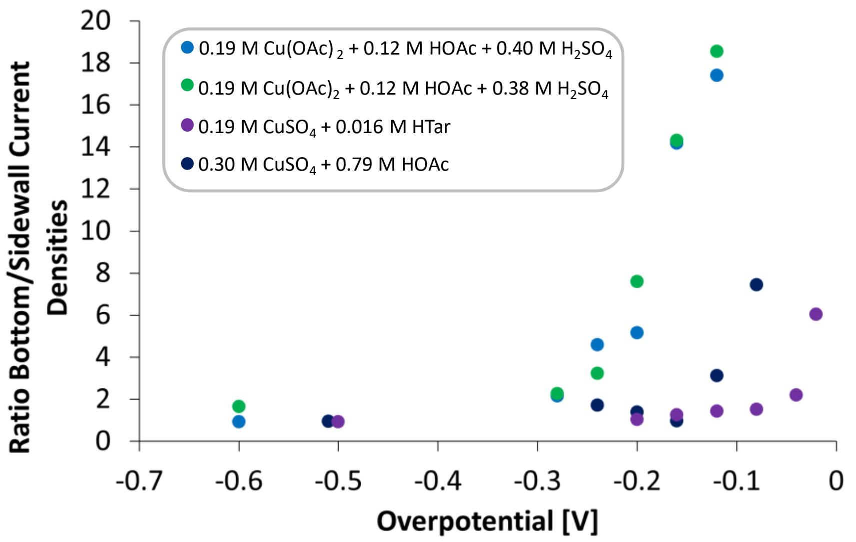

Figure 7-14. Ratios of the bottom/sidewall current densities in the patterned trenches as a function of Cu^{2+}/Cu overpotential from several organic acid containing electrolytes. Figure adapted from Ref [31].

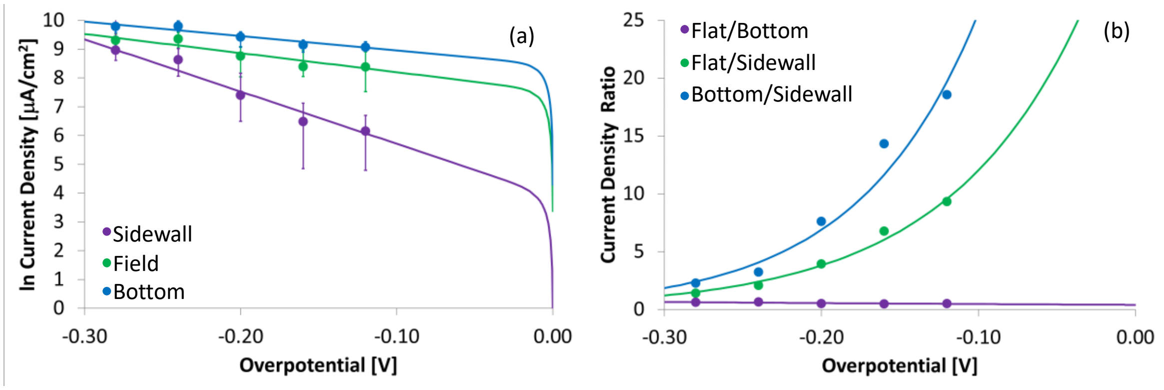

Figure 7-15. Least squares fitting result (shown by solid lines) overlaid on the Tafel data (a) current density ratios (b) as a function of overpotential for Cu2+/Cu reduction for films deposited from 0.19 M $Cu(OAc)_2$*+ 0.12 M HOAc + 0.40 M* H_2SO_4*. Adapted from Ref* [31].

Table 7-1. Exchange current densities (j_0*) and Cathodic Symmetry Coefficients (*α_C*) as calculated by least squares fitting of Tafel data and current density ratios. Adapted from Ref* [31]

Electrolyte	**j0 Flat [mA/cm²]**	**j0 Sidewall [mA/cm²]**	**j0 Bottom [mA/cm²]**	**α_C Field**	**α_C Sidewall**	**α_C Bottom**
0.19 M $CuSO_4$ + 0.79 M HOac	0.93	0.18	2.40	0.08	0.17	0.05
0.19 M CuOAc + 0.12 M HOac + 0.38 M H_2SO_4	2.48	0.06	5.66	0.05	0.20	0.04
0.19 M CuOAc + 0.12 M HOac + 0.40 M H_2SO_4	1.88	0.05	4.70	0.09	0.23	0.06
0.19 M $CuSO_4$ + 0.016 M HTar	0.82	0.34	1.63	0.11	0.17	0.07

With the limitations of the BV analysis and the inconsistencies in the film characteristics with those deposited with known methods for dense Cu filling of recessed features in mind, we suspected that the character of the Cu seed layer in conjunction with the mediating effects of the organic acid species might be responsible for the suppressed sidewall deposition rates at low overpotentials. Some recent research has shown that the texture of PVD deposited Cu seed layers in sub-micron trenches can have varying texture along the trench profile, with equiaxed Cu grains at the flats and bottoms of recessed features and larger Cu grains distributed in a nano-crystalline Cu matrix at the sidewalls [29]. We considered that if such variation in the texture of the seed layer was present it could influence the interaction with the organic acid species. Since the organic acid species inhibited Cu deposition, such variation in the coverage might lead to the variation in Cu deposition rates as we observed at low overpotentials. At large overpotentials with large driving force for reduction of Cu, the organic acid species might have been consumed or incorporated into the growing film at equal rates across the profile, yielding equal deposition rates across the profile and the observed conformal Cu films.

For films deposited galvanostatically, the film characteristics matched those expected from trends observed during potentiostatic depositions. At a lower current density of 5 mA/cm^2, corresponding to maximum deposition overpotential of approximately 150 mV, the films showed suppressed deposition rates at the sidewalls allowing for dense filling of the trenches. At a current density of 8 mA/cm^2, corresponding to a maximum deposition overpotential of 250 mV, the film deposited in a conformal manner with less roughness than the films deposited at 5 mA/cm^2.

To further test effects of the suspected variation in Cu seed layer structure across the trench profile, Pb mediated UPD of Cu was performed. We expected this technique relying on atomic mediators to provide more ‘isotropic’ mediation relative to the bulkier organic acid species and remove any substrate effects from influencing the local deposition rate. As intended and expected, the Pb mediation did yield uniform 2D film growth across the trench profile at all coverages sampled, while the film porosity uniformly improved with increasing Pb coverage. With sufficient Pb coverage, we observed similarly smooth and conformal Cu films to those deposited from organic acid electrolytes at large overpotentials, further confirming our belief that the dense filling from the organic acid electrolytes was possible through the combination of Cu seed layer structure and mediating effects of the organic acid species. In addition, deposition from the perchlorate-based electrolytes provided additional evidence that the Cu seed layer was not uniformly textured along the trench profile. Depositions from electrolytes free of Pb were very rough and exhibited preferential deposition at the sidewalls with suppressed deposition rates at the bottoms and flats, which was opposite the organic acid containing electrolytes. This contrasting deposition pattern again further suggested that the texture and/or structure of the seed layer varied along the profile and its local interactions with the available species in the electrolyte could strongly affect local deposition rates.

The Pb mediated UPD results also demonstrated that this technique could have beneficial effects on conformality and roughness for an electrodeposited Cu film. While the use of Pb raises environmental concerns, friendlier alternatives, such as Zn, have been demonstrated to have similar effects on deposited Zn films and might be suited for deposition in IC applications [30].

Conclusion

The effects of organic acid mediation and Pb mediated UPD on Cu electrodeposition in sub-micron trenches on model IC substrates were investigated. The deposition rates at the sidewalls of the trenches could be sufficiently suppressed at low overpotentials in electrolytes containing acetic or tartaric acid to allow for dense filling of the recessed features. The effect was also possible with galvanostatic deposition. Films deposited by Pb mediated UPD were conformal and smooth across the trench profiles. The films deposited from the organic acid containing electrolytes that densely filled the trenches did not share common features with films deposited from electrolytes with well-known mechanisms for allowing bottom up deposition. Based on the observed trends from organic acid mediated and Pb mediated depositions, the variations in local deposition rates were attributed to variations in the texture/structure of the Cu seed layer across the trench profiles which affected interaction with the mediators in the electrolyte.

References

[1] P. C. Andricacos, C. Uzoh, J. O. Dukovic, J. Horkans, and H. Deligianni, "Damascene copper electroplating for chip interconnections," *IBM J. Res. Dev.*, vol. 42, no. 5, pp. 567–574, Sep. 1998.

[2] T. P. Moffat *et al.*, "Superconformal Electrodeposition of Copper in 500–90 nm Features," *J. Electrochem. Soc.*, vol. 147, no. 12, p. 4524, Dec. 2000.

[3] D. Josell, D. Wheeler, W. H. Huber, and T. P. Moffat, "Superconformal Electrodeposition in Submicron Features," *Phys. Rev. Lett.*, vol. 87, no. 1, p. 016102, Jun. 2001.

[4] S.-K. Kim, D. Josell, and T. P. Moffat, "Electrodeposition of Cu in the PEI-PEG-Cl-SPS Additive System," *J. Electrochem. Soc.*, vol. 153, no. 9, p. C616, Sep. 2006.

[5] J. W. Gallaway, M. J. Willey, and A. C. West, "Acceleration Kinetics of PEG, PPG, and a Triblock Copolymer by SPS during Copper Electroplating," *J. Electrochem. Soc.*, vol. 156, no. 4, p. D146, Apr. 2009.

[6] R. Liske *et al.*, "The Influence of Adsorption Kinetics on Copper Superfilling for Dual Damascene," *J. Electrochem. Soc.*, vol. 163, no. 6, pp. D213–D220, Feb. 2016.

[7] P. M. Vereecken, R. A. Binstead, H. Deligianni, and P. C. Andricacos, "The chemistry of additives in damascene copper plating," *IBM J. Res. Dev.*, vol. 49, no. 1, pp. 3–18, Jan. 2005.

[8] K. Kondo, T. Matsumoto, and K. Watanabe, “Role of Additives for Copper Damascene Electrodeposition,” *J. Electrochem. Soc.*, vol. 151, no. 4, p. C250, Apr. 2004.

[9] T. M. T. Huynh *et al.*, “On the role of halides and thiols in additive-assisted copper electroplating,” *Electrochim. Acta*, vol. 89, pp. 537–548, Feb. 2013.

[10] D. Wheeler, D. Josell, and T. P. Moffat, “Modeling Superconformal Electrodeposition Using The Level Set Method,” *J. Electrochem. Soc.*, vol. 150, no. 5, p. C302, May 2003.

[11] T. P. Moffat, D. Wheeler, S.-K. Kim, and D. Josell, “Curvature enhanced adsorbate coverage mechanism for bottom-up superfilling and bump control in damascene processing,” *Electrochim. Acta*, vol. 53, no. 1, pp. 145–154, Nov. 2007.

[12] K.-C. Lin, J.-M. Shieh, S.-C. Chang, B.-T. Dai, C.-F. Chen, and M.-S. Feng, “Electroplating copper in sub-100 nm gaps by additives with low consumption and diffusion ability,” *J. Vac. Sci. Technol. B Microelectron. Nanom. Struct.*, vol. 20, no. 3, p. 940, Jun. 2002.

[13] T. P. Moffat and D. Josell, “Extreme Bottom-Up Superfilling of Through-Silicon-Vias by Damascene Processing: Suppressor Disruption, Positive Feedback and Turing Patterns,” *J. Electrochem. Soc.*, vol. 159, no. 4, pp. D208–D216, Jan. 2012.

[14] D. Josell and T. P. Moffat, “Superconformal Copper Electrodeposition in

Complexed Alkaline Electrolyte," *J. Electrochem. Soc.*, vol. 161, no. 5, pp. D287–D292, Apr. 2014.

[15] D. Josell and T. P. Moffat, "Bottom-Up Electrodeposition of Zinc in Through Silicon Vias," *J. Electrochem. Soc.*, vol. 162, no. 3, pp. D129–D135, Jan. 2015.

[16] W.-P. Dow, D.-H. Liu, C.-W. Lu, C.-H. Chen, J.-J. Yan, and S.-M. Huang, "Through-Hole Filling by Copper Electroplating Using a Single Organic Additive," *Electrochem. Solid-State Lett.*, vol. 14, no. 1, p. D13, Jan. 2011.

[17] M. Takeuchi, K. Kondo, H. Kuri, M. Bunya, N. Okamoto, and T. Saito, "Single Diallylamine-Type Copolymer Additive Which Perfectly Bottom-Up Fills Cu Electrodeposition," *J. Electrochem. Soc.*, vol. 159, no. 4, pp. D230–D234, Jan. 2012.

[18] G.-Y. Lin, J.-J. Yan, M.-Y. Yen, W.-P. Dow, and S.-M. Huang, "Characterization of Through-Hole Filling by Copper Electroplating Using a Tetrazolium Salt Inhibitor," *J. Electrochem. Soc.*, vol. 160, no. 12, pp. D3028–D3034, May 2013.

[19] H. C. Kim *et al.*, "Bottom-up Filling of through Silicon Vias Using Galvanostatic Cu Electrodeposition with the Modified Organic Additives," *J. Electrochem. Soc.*, vol. 162, no. 3, pp. D109–D114, Jan. 2015.

[20] J. Tang, Q. S. Zhu, Y. Zhang, X. Zhang, J. D. Guo, and J. K. Shang, "Copper Bottom-up Filling for Through Silicon Via (TSV) Using Single JGB Additive," *ECS Electrochem. Lett.*, vol. 4, no. 9, pp. D28–D30, Jul. 2015.

[21] M. J. Kim, S. Choe, H. C. Kim, S. K. Cho, S.-K. Kim, and J. J. Kim, "Electrochemical Behavior of Citric Acid and Its Influence on Cu Electrodeposition for Damascene Metallization," *J. Electrochem. Soc.*, vol. 162, no. 8, pp. D354–D359, Jan. 2015.

[22] Y.-T. Lin, M.-L. Wang, C.-F. Hsu, W.-P. Dow, S.-M. Lin, and J.-J. Yang, "Through-Hole Filling in a Cu Plating Bath with Functional Insoluble Anodes and Acetic Acid as a Supporting Electrolyte," *J. Electrochem. Soc.*, vol. 160, no. 12, pp. D3149–D3153, Sep. 2013.

[23] J.-J. Yan, L.-C. Chang, C.-W. Lu, and W.-P. Dow, "Effects of organic acids on through-hole filling by copper electroplating," *Electrochim. Acta*, vol. 109, pp. 1–12, Oct. 2013.

[24] K. Sieradzki, S. Brankovic, Dimitrov, and N. Dimitrov, "Electrochemical defect-mediated thin-film growth," *Science*, vol. 284, no. 5411, pp. 138–41, Apr. 1999.

[25] S. R. Brankovic, N. Dimitrov, and K. Sieradzki, "Surfactant Mediated Electrochemical Deposition of Ag on Au(111)," *Electrochem. Solid-State Lett.*, vol. 2, no. 9, p. 443, Sep. 1999.

[26] Seongpil Hwang, and Ilwhan Oh, and J. Kwak*, "Electrodeposition of Epitaxial Cu(111) Thin Films on Au(111) Using Defect-Mediated Growth," 2001.

[27] J. Horkans, I. H. Chang, P. C. Andricacos, and H. Deligianni, "Alloying of a Less Noble Metal in Electrodeposited Cu Through Underpotential Deposition," *J.*

Electrochem. Soc., vol. 142, no. 7, p. 2244, Jul. 1995.

[28] E. Mattsson and J. O. Bockris, “Galvanostatic studies of the kinetics of deposition and dissolution in the copper + copper sulphate system,” *Trans. Faraday Soc.*, vol. 55, no. 0, p. 1586, Jan. 1959.

[29] B. B. O’Brien, E. Lifshin, and K. A. Dunn, “Sidewall Texture and Microstructure of iPVD Copper Seed in Narrow Damascene Trenches,” *J. Electrochem. Soc.*, vol. 160, no. 12, pp. D3139–D3144, Sep. 2013.

[30] K. Venkatraman, R. Gusley, L. Yu, Y. Dordi, and R. Akolkar, “Electrochemical Atomic Layer Deposition of Copper: A Lead-Free Process Mediated by Surface-Limited Redox Replacement of Underpotentially Deposited Zinc,” *J. Electrochem. Soc.*, vol. 163, no. 12, pp. D3008–D3013, May 2016.

[31] T. Pounds, K. Sieradzki, J. Erlebacher, and R. C. Cammarata, “Effects of Acetic Acid, Tartaric Acid and Pb UPD on Cu Electrodeposition in Sub-Micron Trenches,” *J. Electrochem. Soc.*, vol. 164, no. 6, pp. D307–D314, 2017.

Chapter 8 - Summary

The research presented in this work focused on design of nanoporous materials for electrocatalytic applications and use of a novel electrochemical flow cell to employ these materials as flow through electrodes in a precisely controlled electrolyte environment.

We first synthesized NP-Cu thin films supported on bulk Cu foils or meshes using an inexpensive and rapid process. The synthesis procedure relied on diffusion bonding of Al or Zn foils to the Cu substrates followed by dealloying in a range of electrolytes. This method allowed for formation of stably dealloyed NP-Cu films several microns in thickness within several hours. The use of mesh substrates demonstrated that hierarchal porosity could be formed directly from this method, and while the NP-Cu didn't form within the pores of the mesh as hoped, slight alterations to the diffusion bonding fixture may allow for optimal formation of uniform NP-Cu on a mesh structure. We showed that the morphology of the nanoporous Cu was strongly dependent on dealloying medium. Electrochemical CO_2 reduction was performed on NP-Cu derived from Cu-Al parent phases, and the results demonstrated that catalyst selectivity was strongly dependent on the structure of the NP-Cu which was controlled by the dealloying medium. The results demonstrated that the NP-Cu was primarily selective for H_2 evolution, and this effect was attributed to the small amount of residual Al that remained in the NP-Cu due to galvanic protection afforded by the layered intermetallic substrates. The NP-Cu films were also impregnated with hydrophobic ionic liquids, which were capable of drastically affecting the selectivity and efficiency of the catalysts, particularly towards formation of formate during electrochemical CO_2 reduction.

We next developed a flow cell and procedure for sequential electrolysis using flow-through porous electrodes in well controlled electrolyte environments. The cell was created with the goal of developing a system optimized for dividing complex, multistep reactions or those susceptible to low selectivity due to detrimental competing reactions such as ammonia synthesis when performed on conventional electrodes into simplified steps to be performed sequentially at separate electrodes. The flow cell employed two complete electrochemical cells, with one cell located entirely within the other and the working electrodes located sequentially at the inlet side of the cell. Such an electrode orientation allowed for delivery of precise amounts of reactants from the first working electrode to the second, but this orientation also prevented the inner electrochemical cell from operating independently of the outer cell. We showed a new method to account for effects of the independent electrochemical cell on the non-independent cell such that both working electrodes could be accurately controlled.

The electrochemical cell was next employed for sequential hydrogen oxidation (HOR) and hydrogen evolution (HER) with a focus on using silicide stabilized NP-Nb both bare and functionalized with Pt nanoparticles as the HER working electrode. The results of the study demonstrate that the Nb based catalysts were capable of efficiently reducing protons created directly upstream at the HOR electrode at large efficiencies when operating at current densities relevant to industrial rates for some applications (>10 mA/cm^2). The bare NP-Nb electrode converted protons at greater than 60% efficiency under these conditions, and the Pt functionalized NP-Nb converted at approximately 100% efficiency due to the activity of the Pt nanoparticles.

In the final project, we report results of an electrodeposition project that initiated our interest in electrochemical synthesis of NP-Cu as reported earlier. We explored the use of novel mediating agents during electrodeposition of Cu in recessed features on model integrated circuit substrates and demonstrated that mediation through the use of organic acids provided a means for depositing pristine films in the recessed features due variation in the deposition rates along the profile of the recessed features at sufficiently low overpotentials. We also demonstrated that UPD mediated electrodeposition of Cu using Pb as the mediating agent yielded uniform deposition across the feature profiles. The mediating effects on the film morphologies were attributed to variation in the structure of the underlying seed layer on the substrate which resulted in variation in the coverage of adsorbed, deposition rate affecting molecules in the case of organic acids but uniform coverage in the case of the atomic Pb mediators.

Curriculum Vitae

Tyler Pounds

typounds@gmail.com | (612) 310-5413

EDUCATION

Johns Hopkins University, Baltimore, MD Dec. 2018

PhD, Materials Science and Engineering

Washington State University, Pullman, WA 2007

MS, Materials Science and Engineering

University of Minnesota-Twin Cities, Minneapolis, MN 2004

BS, Materials Science and Engineering

RESEARCH EXPERIENCE

Research Assistant, Johns Hopkins University, Baltimore, MD January 2014-Present

- Developed novel electrochemical technique for sequential electrochemical reactions and validated utility of technique.
- Created new composite porous catalysts and demonstrated the material's ideal efficiency as a flow through electrochemical catalyst for Hydrogen formation at large reaction rates.
- Conceived new process for inexpensive and rapid production of nanoporous copper films as electrochemical CO_2 reduction catalysts; resulted in presentation at national conference.
- Developed electrochemical deposition process utilizing novel mechanism for synthesis of pristine copper films for integrated circuit applications. Research published in Journal of Electrochemical Society.

Research Assistant, Washington State University, Pullman, WA August 2005-June 2007

- Lead author on review chapter for applications of nanomaterials
- Characterized various materials by electron microscopy for peer reviewed publications
- Synthesized and characterized composites of metal nanoparticles on nanowires

SELECT PUBLICATIONS

T. Pounds, K. Sieradzki, J. Erlebacher, RC Cammarata, *Effects of Acetic Acid, Tartaric Acid and Pb UPD on Cu Electrodeposition in Sub-Micron Trenches*, Journal of the Electrochemical Society, 164, D307, 2017.

T. Pounds, M. G. Norton and D. N. McIlroy, O*ne Dimensional Nanostructures for Sensors and Catalysts*, Handbook of Nanoceramics and Their Based Devices, American Scientific Publishers: 2007.

A. Biswas, I. S. Bayer, B. Marken, T. Pounds and M. G. Norton, Nanotechnology, 18, 305602 (2007).

H. Eilers, A. Biswas, T. Pounds, M. G. Norton and M. Elbahri, J. Mater. Res., 21, 2168 (2006).

SELECT PRESENTATIONS

T. Pounds, E. Benn, C. Wang, J. Erlebacher, *Nanoporous Cu Thin Films for Electrochemical* CO_2 *Reduction*, 232nd meeting of the Electrochemical Society, 2017.

T. Pounds, K. Sieradzki, J. Erlebacher, *The Effects of Organic Acids on Electrodeposited Cu Films in Sub-Micron Trenches*, 2017 Spring meeting of the Materials Research Society.

T. Pounds, S. Farias, K. Sieradzki, RC Cammarata, *In-Situ Stress Characterization of Electrodeposited Silver Films*, 2015 Fall meeting of the Materials Research Society.

T. Pounds, S. Farias, K. Sieradzki, RC Cammarata, Mediated Electrochemical Deposition of Copper and Silver Thin Films for Improved Resistivity, Grain Size and Intrinsic Stress, 228th meeting of the Electrochemical Society, 2015.

T. DeHennis, D. Weires and T. Pounds, *Integral Preoxidation of Aerospace Gear Steels*. Proceedings of the 26th Annual ASM Heat Treating Society Conference, 108, 2011.

APPLIED EXPERIENCE

Materials Engineer, Woodward, Rockford, IL	2012 - 2014
Metallurgist, Northstar Aerospace, Bedford Park, IL	2010 - 2012
Applications Engineer, Hexagon Metrology, Elgin, IL	2008 - 2010

HONORS/AWARDS

Johns Hopkins University

Donald S. Rodbell Award

Whiting School of Engineering Fellowship

Washington State University

Thomas S. Foley Public Service -Alice O. Rice Fellowship

RV Subramanian Graduate Fellowship

University of Minnesota

National and Gopher State Scholarships

Biographical

Born in Ames, IA in 1981.